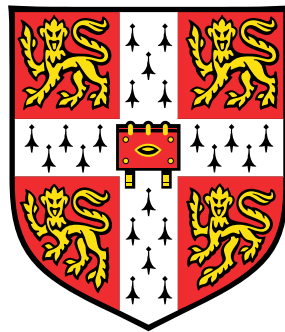


Hydrodynamic interactions in narrow channels



Karolis Misiunas

Department of Physics
University of Cambridge

This dissertation is submitted for the degree of
Doctor of Philosophy

Churchill's College

September 2016

To my loving family

Acknowledgements

I wish to express my heartfelt gratitude to those who have contributed to this thesis and supported me during this marvellous journey. I could not have done this without you.

First and foremost I wish to thank my supervisor, Dr Ulrich F. Keyser. You have been a tremendous mentor for me. I would like to thank you for encouraging my research and for allowing me to grow as a scientist.

I would like to thank the brilliant people that I had pleasure working with. Thank you: Stefano Pagliara for introducing me to microfluidics and giving me an extensive mentorship; Sandip Ghosal for teaching me how to study physical phenomena; Eric Lauga for giving insights into mathematical models; Silvia Hernandez-Ainsa for answering my silly chemistry questions. My first project was in collaboration with Nadanai Laohakunakorn, who also indulged us with music. Thereafter, I had the pleasure of working with Simon Dettmer, Yizhou Tan, and Soichiro Tottori on microfluidics. I have learned a lot from you. I must also thank my two students, Jerome Burelbach and Antony Scott, for their work. I am grateful to have shared offices with Kerstin Göpfrich and Michael Walker – you are awesome! And I must acknowledge my endearing friend Vahe Tshitoyan, who lent me his expertise in e-beam lithography.

Sometimes my research had hiccups, but the rich social dynamics of our lab kept me going forward. From the first moments, I was welcomed by the veterans: Oliver, Catalin and Oli. Big thanks to Alex and Madhavi for organising the unforgettable journey to Scotland. I will always remember the 500 mile trip to Lake district with Thomas, Elisa, and Jinglin. And the cardboard boat that we built with Vivek, Kerstin, Nadanai, and Sowmya. Let's not forget all the foosball games, where we never quite managed to beat the Invincibles: Jehangir and Nick! We had so much fun in Churchill guest nights, where Lisa had the most memorable costume. Thanks to Maria for introducing me to bouldering. It was pleasant to see the cheerful attitude brought by Michael Schaich and Kareem. Thanks to Theresa and Kaikai, who would keep me company during the late night experiments. It is great to see our group rejuvenating with Jannes, Jinbo, Clare, and Alice, who have brought new ideas. You are all great and I am glad to have shared this experience with you. Thank you, friends!

Lastly, a number of people deserve to be acknowledged for keeping my mind straight outside the lab. Dear Ben, Hannah, Andrius, Joakim, Judith, Matthew, Giorgio, Matic, Philip, Flaviu, Vivak, Janusz, Themis, Aurimas, Siri, Juliet, Ani, Floris, Michael, Igor, Mika, Hannah, Paul, Kotryna, and Aurimas; you have enriched my life in Cambridge. I would also like to thank my mom, dad and brother for their continued support and love.

Table of contents

1	Introduction	1
2	Theory	7
2.1	Brownian motion	8
2.1.1	Smoluchowski equation	9
2.2	Hydrodynamics	10
2.2.1	Hydrodynamic interactions	12
2.3	Driven transport	13
2.3.1	Pressure and Poiseuille flow	13
2.3.2	Gravity	13
2.3.3	Double layer	13
2.3.4	Electroosmosis	16
2.3.5	Electrophoresis	17
2.4	Relevance of our model system	18
3	Brownian Motion in Channels	21
3.1	Method for microfluidics experiments	21
3.1.1	Fabrication	22
3.1.2	Particle tracking	26
3.2	Brownian motion experiments	33
3.2.1	Spacially resolved diffusion coefficients	35
3.2.2	Channel dimensions	35
3.3	Method for hydrodynamic simulations	38
3.3.1	Diffusion coefficients in infinite channels	39
3.4	Simulation of spacially varying D_x	41
3.4.1	Complex cross-section shapes	42
3.4.2	Approximations in all simulations	46
3.5	Increased diffusivity in finite channels	47

3.5.1	Access resistance	49
3.5.2	Comparison with experimental data	51
3.6	Conclusion and impact	51
4	Hydrodynamic Particle Interactions	53
4.1	Method for placing particles in channels	53
4.2	Nondecaying interactions	55
4.2.1	Hydrodynamic interaction model	57
4.2.2	Analytical model	58
4.3	Many particle interactions	61
4.3.1	Generalised interaction model	62
4.4	Discussion and special cases	66
4.4.1	Pressure exchange mechanism	66
4.4.2	Relation between correlation and $\zeta_{i,j}$	67
4.4.3	Varying particle size	68
4.4.4	Interaction at the entrances	68
4.4.5	No external oscillations	70
4.5	Conclusion and impact	70
5	Driven Transport	73
5.1	Methods for driving particles	74
5.1.1	Pressure	74
5.1.2	Electric fields	76
5.1.3	Electrophoresis of isolated particles	80
5.1.4	Electrophoretic velocity versus c_0 and pH	81
5.1.5	Charge polarisation with Ag/AgCl electrodes	83
5.1.6	Gravity as driving force	84
5.2	Driven particle interactions	87
5.2.1	Electrophoresis: enhancement coef. versus c_0 and pH	89
5.3	Model for driven particle interactions	91
5.3.1	No interactions under pressure	91
5.3.2	Hydrodynamic interactions under gravity fall	92
5.3.3	Electrophoresis: competition between piston and backflow	94
5.4	Conclusion and impact	99
5.4.1	Electrophoresis vs pressure	100
	Summary and Outlook	103

Appendix A	Entrance jamming in electric field	105
Appendix B	More on experimental methods	109
B.1	E-beam lithography and Si etching protocol	109
B.2	PDMS/glass bonding quality	110
B.3	Measuring D_x for migrating particles	111
B.3.1	Comparison to DNA polymer transport	112
B.4	Velocity auto-correlation function and motion blur	114
B.4.1	VACF for moving particles	115
Appendix C	Full analytical model for particle interaction	117
	List of publications	123
	List of figures	125
	List of tables	129
	List of revisions	131
	References	133

Chapter 1

Introduction

In 1959, Richard Feynman gave a lecture entitled ‘There’s plenty of room at the bottom’ to promote nanotechnology. He imagined a future where a patient would ingest a pill filled with tiny machines, which would fix the body from within. Such unparalleled control is approaching, but before we can build such tiny machines, we must understand the science at these length-scales; one small step at a time.

Our goal here is to understand small channels filled with liquid, that are found in our bodies and across the physical world. In nature, such channels come in many shapes and sizes. For example, Figure 1.1a shows a porous rock, where the interlinked cavities form a network of channels. Similarly, biological organisms use a network of channels to transport biomolecules around the body. Our cardiovascular system has channels with diameters ranging from 10 mm for arteries, down to 5 μm for the smallest capillaries that are shown in Figure 1.1b. Zooming in even closer, into the cells themselves, we discover perhaps the smallest channels found in nature - the protein pores. Figure 1.1c shows a Maltoporin pore that facilitates the transport of sugars into Gram-negative bacteria. The typical inner diameters of protein pores range from 50 nm down to only 0.5 nm [1].

In technology, channels are found in porous materials, like the novel electrodes shown in Figure 1.1d. These pores dramatically increase the surface area, thus allowing the rapid charging of batteries [4]. Another example is gel electrophoresis, where charged particles migrate through a porous gel. Biochemists use this method to separate molecules on the basis of their size and charge. Meanwhile, industrial particle separation uses filtration membranes. Figure 1.1e shows a membrane composed of tiny channels that remove dust and bacterial contaminants from water [6]. Individual channels may also be used as biosensors, capable of identifying the bases of a DNA molecule. Figure 1.1f shows an illustration of the DNA sequencing mechanism found in an Oxford Nanopore Technologies Ltd, MinION sequencer.

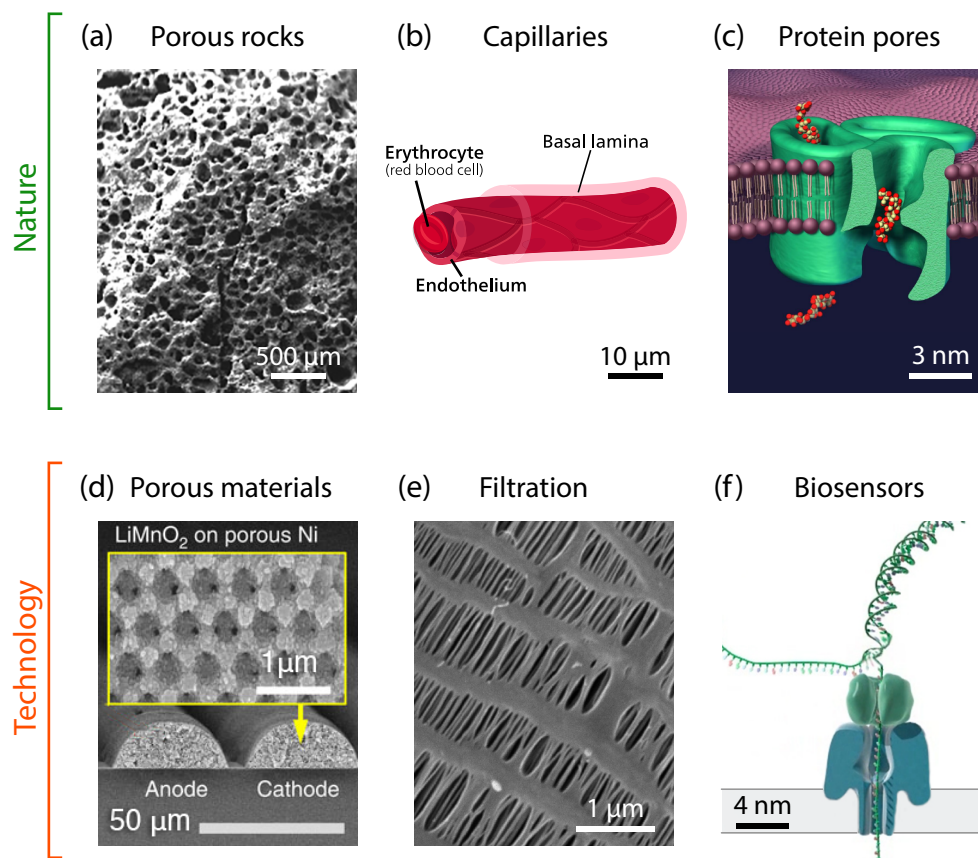
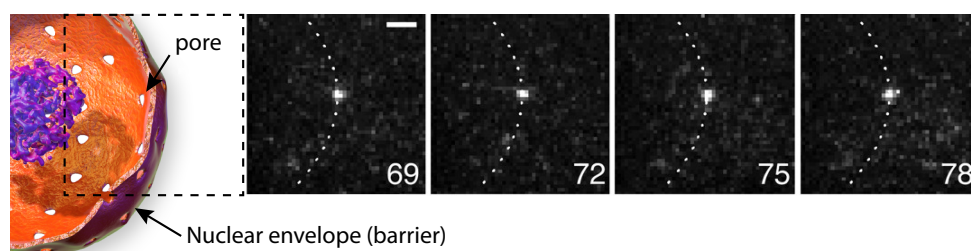


Figure 1.1: Examples of channels found in nature and technology. (a) SEM micrograph of a highly porous magnesiumian limestone, where the holes form a network of channels. (b) The mammalian circulatory system transports blood in channels called vessels. The smallest of them are called capillaries. (c) Protein pores transport ions and molecules through cell membranes. The illustration shows a Malto porin pore, which can transport maltodextrins into *Escherichia coli* bacteria. (d) Porous electrodes increase the surface area for chemical reactions, thus enabling quickly chargeable batteries. (e) SEM image of a porous membrane made out of fibril fibres. It is used as a filtration membrane, where the channel-like structures stop unwanted particles. (f) Biosensors aim to identify biomolecules for medical diagnostics. Here, a DNA molecule is threaded through an alpha-hemolysin protein channel. The DNA sequence is determined by measuring an electric current flowing through the pore. Figure adapted from [2–6].

(a) Diffusive transport through a nuclear pore



(b) Electrophoretic transport of DNA through a nano-capillary

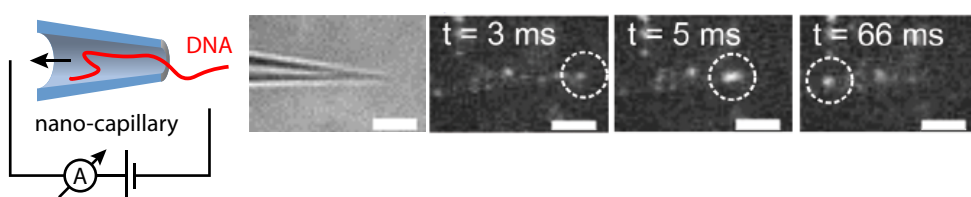


Figure 1.2: Measurements of particle transport through nano-channels. (a) Single molecule translocation through a nuclear pore complex. Imaged using single molecule fluorescence (SMF) microscopy [7]. The fluorescently tagged molecule moves passively from the cytoplasm to the nucleus. The technique had spatial resolution of 30 nm and temporal resolution of 3 ms. The scale bar indicates $2\ \mu\text{m}$ and the numbers indicate time in milliseconds. (b) DNA translocation through a nano-capillary, which was also imaged using SMF [8]. An external electric field drives the DNA through the capillary. Capillary tip radius was about 50 nm. The scale bars indicate $5\ \mu\text{m}$. In both cases, only a few frames are captured with the molecules inside the channels, thus limiting the amount of information that can be inferred about the behaviour inside the channels. Figure adapted from [7–10].

In all these examples, channels facilitate the transport of particles whether they are ions, molecules, or larger assemblies. Biological channels are made for a sole purpose of moving particles around. For example, consider the functions of protein channels. At the small end of the size spectrum, we find voltage-gated ion channels that are normally closed, but an increase of membrane potential can open them, thereby allowing ions to pass. This transistor-like behaviour is vital for neurons because it propagates signals along the axons [1]. Aquaporin channels specialise in the transport of water across membranes. Their shape allows high permeability, while maintaining a very high selectivity for water [11]. The nuclear pore complex also has a high selectivity due to a polymer brush inside the channel, which permits the passage of specialised transporters [12]. These facilitate the transport of signalling molecules into the nucleus and then bring RNA molecules back to the cytoplasm, thus acting as a gateway for accessing the genetic material. These three examples demonstrate the diversity of transport modes that are all vital for life. Disorders of ion channels are associated with a large number of diseases, such as epilepsy or osteopetrosis [13]. Consequently, understanding the particle behaviour inside such channels is of critical importance. For example, Figure 1.2a shows an experimental observation of a single molecule moving across a nuclear pore, where its trajectory reveals that passive diffusion drives this transport [7, 12]. However, two constraints limit our understanding of this process. First, the microscope resolution is insufficient to determine the exact dynamics within the channel. The nuclear pore is the biggest protein pore, but the experiment that is shown in Figure 1.2a only obtained a few position points per molecule [7]. The same problem occurs in synthetic nano-channels, where, for example, Figure 1.2b shows a voltage-driven translocation of a DNA molecule through a nano-capillary. Note that the DNA passed through the capillary tip in just half a millisecond, thereby leaving us unable to determine the velocity in the tip. The second major obstacle is complexity: biological channels have irregular shapes and can change their conformation or sometimes have molecular binding sites inside. Such complexity obscures the contributions from different phenomena. These two reasons make it difficult to understand the physics involved in particle transport.

Our goal is to understand the fundamental principles of particle behaviour in channels, and therefore, we must address both limitations discussed above. Therefore, we study particle motion in highly controlled microfluidic channels that serve as a model system, as shown in Figure 1.3. The characteristic sizes of our channels and particles are approximately $1\ \mu\text{m}$ across, which is small enough to have significant Brownian motion, but still large enough to resolve using a bright-field microscope. This dimensional scale-up increases our spacial and temporal resolution, thereby solving the first problem. To solve the second problem of complexity, we simplify the geometry: particles are modelled by spherical colloids, while our channels are fabricated straight and uniform, enabling a direct comparison with theory.

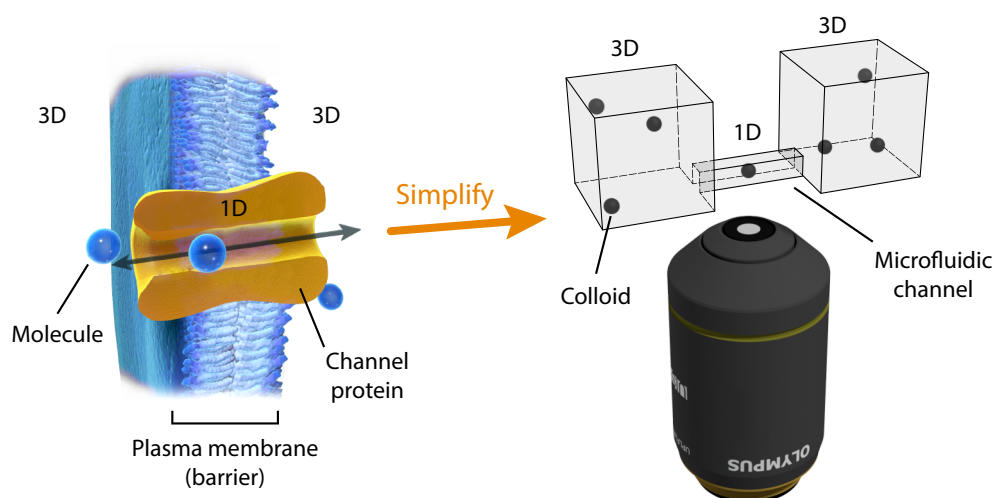


Figure 1.3: Biological channels have complex shapes and features that make it difficult to understand particle transport through them. In contrast, microfluidic channels have a well defined shape. The molecules are approximated as spherical colloidal particles. The characteristic diameter of our synthetic channels is about $1\ \mu\text{m}$, allowing us to image them using bright-field microscopy. Figure adapted from [9].

Similar systems have been applied previously to study electrostatic interactions [14–16], steric interactions [17–19], and hydrodynamic interactions [20–25]. In this thesis, we focus on the hydrodynamic interactions between particles, the particles and the channel walls, and the role in driven transport.

The work is organised as follows. In the second chapter of this thesis, we will introduce the relevant theory for Brownian motion, hydrodynamics, and electrokinetics. Chapter 3 will present our experimental methods and also the measurement of diffusion coefficients, which are related to the hydrodynamic friction experienced by a moving particle. We will demonstrate that theory underestimates the diffusion coefficients, which leads us to suggest a new method for modelling hydrodynamics inside finite channels. Chapter 4 focuses on particle-particle interactions between particles undergoing Brownian motion. Here, we will show that hydrodynamics in channels produces a unique mode of interaction that is distance-independent. Chapter 5 will demonstrate that these hydrodynamic interactions persist for electrophoretically driven particles as well. All these phenomena share a fundamental principle: channels of finite length have a flow across the inlets, which can be modelled with periodic boundary conditions.

These discoveries present a valuable contribution towards understanding the physics inside channels. We expect that this knowledge will help estimate the permeability of porous materials [26, 27] and drug diffusion through protein channels [28]. Perhaps most importantly, we predict a new type of particle-particle interaction that was previously unknown.

Chapter 2

Theory

This chapter introduces theoretical concepts necessary for understating particle behaviour in channels. Specifically, we will introduce Brownian motion that acts on all small particles. When these particle move, they experience hydrodynamic drag that couples them to the surrounding liquid. Therefore, we will introduce hydrodynamics and how it depends on the confinement. Finally, we will also study different methods for actively driving particle through channels, for which we must explain electrokinetic effects.

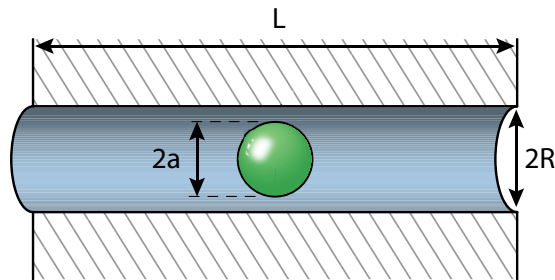


Figure 2.1: Our model problem: two reservoirs are connected by a liquid filled channel of length L and diameter $2R$. The spherical particle inside the channel has diameter of $2a$.

We start by introducing our model system for understanding particle behaviour and interactions inside channels. Figure 2.1 shows a simple geometry, where the particles are spherical with diameter $2a$, and the channel has a uniform cross-section with diameter $2R$. The channel has a finite length, L , which connects two reservoirs. The entire system is filled with liquid. Using this model system, we aim to understand particle motion in channels and the corresponding transport properties.

2.1 Brownian motion

In water, a particle is surrounded by solvent molecules that are constantly moving due to thermal energy. Collisions between them can transfer some momentum to the particle, thus resulting in its motion. This motion is damped by the surrounding liquid that quickly stops the particle. The direction and magnitude of such ‘step’ is random. The particle constantly performs these random steps, essentially performing a random walk throughout the environment, which is called Brownian motion. This process can be described with the Langevin equation [29, p. 62]:

$$m \frac{d^2x}{dt^2} = -\zeta \frac{dx}{dt} + \vartheta(t) + F_{\text{ext}}, \quad (2.1)$$

where m is the mass of our particle, x is its position, ϑ is the random force caused by the thermal collisions, F_{ext} is an external force acting on the particle, and ζ is the hydrodynamic friction coefficient for a moving particle in a liquid. The random force is typically approximated by white noise, which has a Gaussian distribution with zero mean and correlation function:

$$\langle \vartheta(t_1) \vartheta(t_2) \rangle = 2\zeta k_B T \delta(t_1 - t_2). \quad (2.2)$$

The resulting motion has two characteristic time-scales [30, 31]. Initially, inertia dominates the particle motion with characteristic time-scale of $\tau_p = m/\zeta \sim 0.1 \mu\text{s}$. Here, the particle receives a thermal impulse and moves in a straight line at velocity v . The surrounding liquid resists this motion by exerting a drag force, $F_d = \zeta v$. This process is called ballistic Brownian motion and its duration can be measured using the velocity auto-correlation function (VACF):

$$\text{VACF}(\tau) \equiv \langle v(t) v(t + \tau) \rangle. \quad (2.3)$$

From Equation (2.1) it can be shown that the velocity auto-correlation function decays exponentially with time, $\text{VACF} \sim e^{-t/\tau_p}$. However, this is an oversimplification since the moving liquid carries additional momentum. As a result the velocity auto-correlation function decays slower than expected by Langevin equation, at a rate $\text{VACF} \sim t^{-3/2}$. This effect is called hydrodynamic memory [30, 32]. The characteristic time for this process is $\tau_f = a^2 \rho_f / \eta \sim 10 \mu\text{s}$. In channels, theory predicts a much smaller hydrodynamic memory effect that leads back to the exponential decay of the velocity auto-correlation [33]. However, particles also have a secondary coupling carried by sound, which decays as $\text{VACF} \sim -t^{-3/2}$ [34]. This effect has

negative magnitude and is much weaker than conventional decay due to the hydrodynamic friction.

In our experiments, we measure particle motion at much longer time-scales, where $VACF = 0$. The resulting particle motion is known as Brownian motion and it was first theoretically described by Sutherland [35], Einstein [36] and Smoluchowski [37] around 1905. Here, the particle performs a random walk with no net progress, $\langle \Delta x(t) \rangle = 0$. It does, however, explore a growing region in time that is described by the mean squared displacement (MSD), $\langle (\Delta x(t))^2 \rangle = 2D_x t$, where D_x is the diffusion coefficient along one coordinate. This coefficient depends on the temperature of the system and the hydrodynamic friction coefficient via the Einstein-Smoluchowski relation

$$D_x = k_B T \zeta^{-1}. \quad (2.4)$$

2.1.1 Smoluchowski equation

The long time-scale evolution of particles can be described by the Smoluchowski equation¹ [29, p. 100]

$$\frac{\partial n}{\partial t} = D \frac{\partial^2 n}{\partial x^2} - \frac{1}{\zeta} \frac{\partial (n F_{\text{ext}})}{\partial x}, \quad (2.5)$$

where n is the probability density for finding the particle in a given position in 1D. For multiple interacting particles, it reads [29, p. 226]

$$\frac{\partial f_N}{\partial t} = \sum_{i,j=1}^N \frac{\partial}{\partial x_i} D_{i,j} \left(\frac{\partial}{\partial x_j} - \frac{F_{j,\text{ext}}}{k_B T} \right) f_N, \quad (2.6)$$

where f_N is an equivalent distribution function in a configuration space. In this notation, the electrostatic interactions are introduced through the external force term $F_{j,\text{ext}}$. Meanwhile, the hydrodynamic interactions are embedded in the diffusion coefficient matrix $\mathbf{D} = [D_{i,j}]$, that is inversely proportional to the hydrodynamic friction coefficient matrix via Einstein-Smoluchowski relation, $\mathbf{D} = k_B T \mathbf{Z}^{-1}$. The friction matrix is symmetric, $\zeta_{i,j} = \zeta_{j,i}$, and has the following structure [29, p. 226]

¹A general version of this equation is called Fokker-Planck equation.

$$\mathbf{Z} = \begin{bmatrix} \zeta_{1,1} & \cdots & \zeta_{1,N} \\ \cdots & \ddots & \cdots \\ \zeta_{N,1} & \cdots & \zeta_{N,N} \end{bmatrix}, \quad (2.7)$$

where the diagonal terms, $\zeta_{i,i}$, describe the hydrodynamic friction with the surrounding environment for particle i . The off-diagonal terms, $\zeta_{i,j}$, describe the hydrodynamic interaction between particles i and j . We will use this notation extensively throughout the thesis.

2.2 Hydrodynamics

Liquids are incompressible due to strong intermolecular interactions that produce a large inwards pressure [38]. The Navier-Stokes equation for incompressible liquids reads

$$\frac{\partial \mathbf{u}}{\partial t} + (\mathbf{u} \cdot \nabla) \mathbf{u} - \frac{\eta}{\rho_f} \nabla^2 \mathbf{u} = -\frac{1}{\rho_f} \nabla p + \mathbf{f}, \quad (2.8)$$

where \mathbf{u} is the flow velocity, η is the dynamic viscosity, p is the pressure, ρ_f is the density, and \mathbf{f} is an external force distribution. In a typical nano- or microfluidic system, the viscous forces dominate over the inertial forces, leading to low Reynolds number flows with the definition

$$Re = \frac{\text{inertial forces}}{\text{viscous forces}} = \frac{\rho_f 2Ru}{\eta} \sim 10^{-3}, \quad (2.9)$$

where $2R$ is the characteristic width of the channel and u is the typical flow velocity. This value suggests that the viscous forces dominate the flow. Therefore, the Navier-Stokes equation can be simplified by discarding the inertial terms, leading to the Stokes' equation for laminar flows

$$\eta \nabla^2 \mathbf{u} = \nabla p - \mathbf{f} \quad (2.10)$$

$$\nabla \cdot \mathbf{u} = 0. \quad (2.11)$$

It is a linear equation, allowing us to superimpose independent solutions for different boundary problems. Stokes' equation also has no time component, implying that information propagates instantaneously, which is an approximation, because in real water, information propagates at the speed of sound, $c \approx 1482 \text{m/s}$. This approximation is accurate for our system, because information propagates over the length-scale of our system. For example, in 10 ns

a change in pressure travels $15\ \mu\text{m}$, while in $1\ \mu\text{s}$ it travels $1.5\ \text{mm}$. For comparison, our experimental particles are about $500\ \text{nm}$ wide and channels are about $1\ \mu\text{m}$ wide and $10\ \mu\text{m}$ long.

Coming back to the isolated spherical particle, we are interested in a drag force due to its motion through the liquid. In bulk, this drag is given by the Stokes' law

$$F_d = -6\pi\eta a v, \quad (2.12)$$

where v is particle's velocity. This equation can be related to the hydrodynamic friction coefficient that was used in the description of Brownian motion

$$\zeta_0 = -\frac{F_d}{v} = 6\pi\eta a. \quad (2.13)$$

Here, 0 indicates that the coefficient is for bulk. The value has to be adjusted in confinement, because surfaces alter the flow fields by imposing no-flux and no-slip boundary conditions. Confinement effects on spherical particle motion can be quantified using Faxen's laws, but its solutions are scarcely available. One useful solution gives the force on a particle moving parallel to an infinite plane [39, p. 327]:

$$F_d = -\frac{\zeta_0 v}{1 - (9/16)(a/r)} + O\left((a/r)^2\right), \quad (2.14)$$

where r is the distance from the sphere to the plane. This equation highlights an important trend: the drag on the particle increases when it gets closer to a wall.

In channels, the walls also restrict flows, leading to an increased drag force. For very long channels ($L \rightarrow \infty$), analytical solutions exist [39, p. 320] and have been studied extensively [40]. These solutions are based on expansions and therefore are complex. However, the trend holds: the friction coefficient increases with the confinement, where the confinement is quantified with a ratio between the diameters of the particle and the channel, a/R . We will use the confinement ratio to classify our experiments. When $a/R \gtrsim 0.3$, the particles are tightly confined by the channel and we say that the channel is narrow. For smaller a/R values, the channel becomes increasingly like bulk and the friction coefficient approaches Equation (2.13).

When discussing the hydrodynamics equations we assume no-slip boundary conditions on all surfaces, $u = 0$. This standard boundary condition works well for micrometer sized

systems [39, p. 51], and we will continue using the no-slip boundary condition unless stated otherwise.

2.2.1 Hydrodynamic interactions

A moving particle induces a flow field that extends far into the liquid. Other particles in this flow field react to and interact with it, thus resulting in a hydrodynamic particle-particle interaction. The force on the second particle depends on the position and also on the velocity of the first particle. This is fundamentally different from electrostatics, where the position is sufficient to determine the force vector. The magnitude of the hydrodynamic force is linearly proportional to the speed of the first particle, thereby we can quantify the interaction using the hydrodynamic friction matrix or the diffusivity matrix, as it was discussed in Section 2.1.1.

In 3D, or for two particles in bulk, the interactions are well understood theoretically [39, p. 235], with an approximate solution given by [29, 41, p. 226]

$$\mathbf{D}_{1,1} = \mathbf{D}_{2,2} = \frac{k_B T}{\zeta_0} \mathbf{1}; \quad \mathbf{D}_{1,2} = \mathbf{D}_{2,1} = k_B T \mathbf{T}, \quad (2.15)$$

where $\mathbf{1}$ is an identity matrix, and \mathbf{T} is the Oseen tensor [39, p. 320]:

$$\mathbf{T} = \frac{1}{8\pi\eta} \left(\frac{\mathbf{1}}{|\mathbf{r}|} + \frac{\mathbf{r}\mathbf{r}}{|\mathbf{r}|^3} \right). \quad (2.16)$$

This equation suggests that the interaction strength decays with distance as $1/r$, where r is the distance between two spherical particles. The literature often refers to this as a long-range interaction, because it extends much further than electrostatic interactions between particles. This result has been confirmed experimentally [42].

In 2D, or for particles tightly confined between two infinite planes, the strength of hydrodynamic interactions decays faster, as $1/r^2$. Here, the confinement changes the flow field, thus modifying the decay function. This was also confirmed experimentally [24, 41, 43].

In 1D, or for particles inside narrow channels, the hydrodynamic interactions are predicted to decay exponentially, as $\sim \exp(-r/2R)$ [22, 44]. Some experiments have attempted to confirm this relation [22, 24, 25], but we will argue in Chapter 4 that these experiments did not capture 1D hydrodynamics, because the liquid could escape the channel through open sides. Thus leaving open questions about the hydrodynamic particle-particle interactions in 1D.

2.3 Driven transport

Our particles are not only subject to Brownian motion but can also be actively transported by applying external forces. We consider three driving sources for actively driving particles through channels: pressure induced flow, gravity fall, and electrostatic pull. We start by describing the former two forces. However, the main topic of this section is the electrostatic pull, which in liquids is called electrophoresis. To explain how it works we will first consider two other electrokinetic phenomena: the double layer that forms at the interface between a liquid and a solid, and electroosmosis that propels a liquid in an external electric field.

2.3.1 Pressure and Poiseuille flow

A pressure difference across a cylindrical channel induces a Poiseuille flow. It has a characteristic parabolic profile given by: $u(r) = \Delta p (R^2 - r^2) / 4\eta L$, where r is a radial coordinate and Δp is the pressure difference [38]. The flow rate is described by the Hagen-Poiseuille equation

$$\frac{dV}{dt} = \langle u \rangle \pi R^2 = -\frac{\pi R^4}{8\eta} \frac{\Delta p}{L}, \quad (2.17)$$

where V is the volume of the liquid transferred. This flow can transport particles across channels, since particles simply follow the resulting flow field.

2.3.2 Gravity

Gravity acts directly on a particle, where the force is a combination of gravitational pull and buoyancy. Using the Archimedes' principle the force reads

$$F_g = 3/4 \pi a^3 (\rho_p - \rho_f) g, \quad (2.18)$$

where ρ_p is the density of the particle, ρ_f is the density of the fluid, and g is gravitational acceleration. Note that gravity is not affected by confinement and particles in channels fall slower due to the increased hydrodynamic friction.

2.3.3 Double layer

Hydrophilic particles often carry (negative) surface charges and thus can be manipulated by electric fields. In order to understand the forces we need to briefly consider the solid/liquid interface. Water is capable of dissociating bonds of exposed groups on many surfaces. For

example, a glass surface undergoes oxide dissociation process ($-\text{OH} \longrightarrow -\text{O}^- + \text{H}^+$) leaving it with a negative surface charge. Such surface charges create an electric field that attracts counter-ions. Taken together, the charged surface and the counter-ions are known as the double layer.

Gouy and Chapman formulated the first model of the double layer using empirical observations [45]. Their description includes a diffuse layer in which counter-ions are free to move around. Later, Stern reviewed their results and formulated a better picture called Gouy-Chapman-Stern model [46]. It includes a Stern layer of immobilised ions at the surface. Despite its simplifications, the model captures two important phenomena: the freely diffusing ion cloud and immobilised ions on the surface.

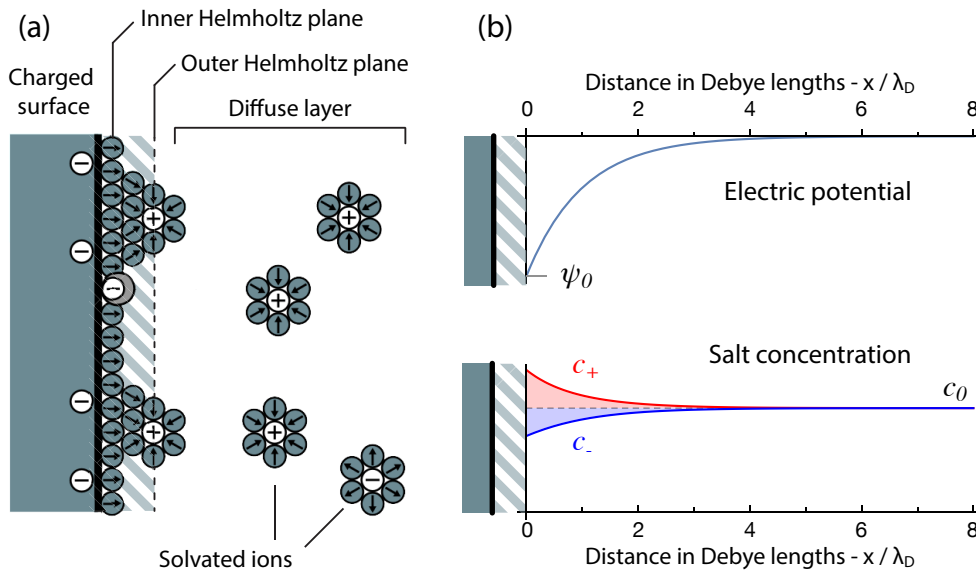


Figure 2.2: (a) Illustration of the double layer for low surface charges: the charged surface attracts counter-ions, some of which get immobilised on the surface, while others remain free in the diffuse layer. The boundary between fixed and mobilised ions is called outer Helmholtz plane (or Stern layer). (b) In the diffuse layer, the charged surface creates an electric potential that attracts counter-ions and pushes away anions. This uneven ion concentration results in a net charge in the diffuse layer, screening the negatively charged surface. Figure adapted from [47].

Figure 2.2a shows a schematic illustration of the double layer. The Stern layer has two parts: The inner Helmholtz layer consists of immobilised ions that are absorbed at the surface. The outer Helmholtz layer represents immobilised counter-ions that are temporarily stuck to the surface. Ions beyond this point are in the diffuse layer where they move around freely. Figure 2.2a also shows solvent molecules, whose dipoles are indicated by an arrow. They form hydration shells around free ions which increase their effective diameters. Note that, polar

solvent molecules also have a preferred direction near the surface [45]. This restricts the motion of water molecules and thus reduces the dielectric constant to about $\epsilon_r \approx 4$ at the surface [48].

In the following, we consider the diffuse layer, in which ions are mobile and arrange themselves in such a way that they minimise the free energy. The local electric field drives counter-ions closer and co-ions further away from the charged surface. The resulting electric potential, ψ , is described by Poisson's equation,

$$\epsilon \nabla^2 \psi = -\rho_C = -e(c_+ - c_-), \quad (2.19)$$

where ρ_C is charge density and c_{\mp} are the concentrations of ions and counter-ions. Ions are subject to Brownian motion adding thermodynamic character to the system. At equilibrium their distribution in the electric potential, $e\psi$, is given by the Boltzmann distribution [45]:

$$c_{\pm} = c_0 \exp\left[\mp \frac{e\psi}{k_B T}\right], \quad (2.20)$$

where c_0 is ion concentration in the bulk. The combination of the two equations is known as the Poisson-Boltzmann equation [45, 49]:

$$\nabla^2 \psi = \frac{2ec_0}{\epsilon} \sinh\left(\frac{e\psi}{k_B T}\right). \quad (2.21)$$

It describes the electric potential in a salt solution with charged surfaces. If the surface potentials are small it can be simplified using $\sinh(x) \approx x$. This approximation is known as the Debye-Huckel equation [45]:

$$\nabla^2 \psi \approx \frac{\psi}{\lambda_D^2}; \quad \lambda_D \equiv \sqrt{\frac{\epsilon k_B T}{2e^2 c_0}}, \quad (2.22)$$

where λ_D is the Debye screening length. It is the characteristic length-scale over which the free ions screen the electric potential created by a charged surface. For example, a 5 mM KCl salt solution has a screening length of $\lambda_D \approx 4.3$ nm.

Figure 2.2b shows a solution of Equation (2.22) next to an infinite plane. The electric potential decays exponentially within a few Debye lengths. This rapid screening of surface potential is caused by an increased concentration of counter-ions and a depletion of co-ions. The concentrations were obtained using Equation (2.20) and are shown in the lower panel

of Figure 2.2b. This screening reduces the electrostatic particle-particle interactions down to ~ 10 nm.

The boundary conditions for solving the Poisson-Boltzmann equation can be determined using Gauss' law. For a surface with a charge density σ_q and a normal vector \vec{n} it is $\vec{n} \cdot \nabla \psi = -\sigma_q/\epsilon$. However, this approach often overestimates the surface potential [50] because it fails to account for the ions immobilised in the Stern layer. For this reason, it is practical to introduce an effective potential at the outer Helmholtz layer that we call the surface potential², ψ_0 . It is used as an effective parameter to absorb all the complexities at the surface. For nearly flat surfaces with low charge density, Grahame's equation is an accurate approximation for the surface potential [45]:

$$\psi_0 \approx \sigma_q \lambda_D / \epsilon. \quad (2.23)$$

2.3.4 Electroosmosis

The immobilised charges on the surface lead to an charge imbalance next to the wall. If an external electric field is applied along the surface, it causes ion migration that exerts a force on the liquid. In the diffuse layer there is an unbalanced number of ions and counter-ions, as shown in Figure 2.2b, that exerts a net force on the liquid $f = -\rho_C E$. Therefore, the liquid is propelled in the diffuse layer [51].

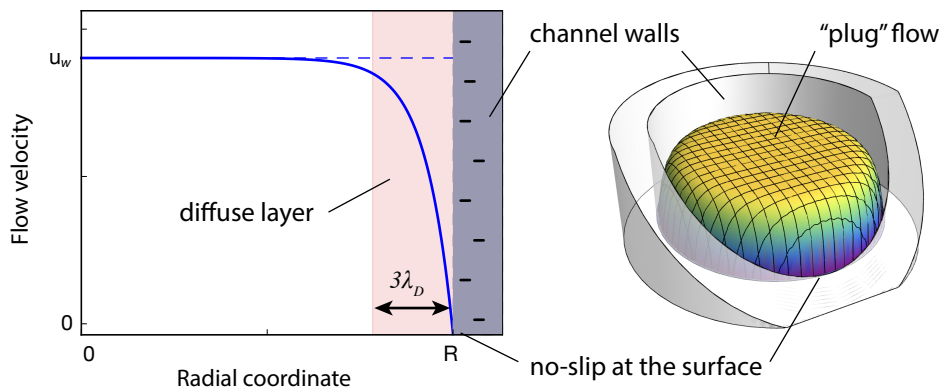


Figure 2.3: Illustration of electroosmotic plug flow inside a narrow channel. The propulsion of the liquid develops in the diffuse layer close to the charged surface of the channel. There are no forces acting on a liquid in the center of the channel, resulting in a flat flow profile.

²In literature, surface potential is called zeta potential, but we do not use this convention since the zeta symbol (ζ) is used for the hydrodynamic friction coefficients.

For an example solution, consider a cylindrical channel with charged walls. An external electric potential, U , is applied at the inlets that creates an electric field inside the channel, $E = U/L$. Figure 2.3a shows the solution to Equations (2.22) and (2.10) in the limit of thin diffuse layer, i.e. $\lambda_D \ll R$. The liquid speeds-up within three Debye lengths from the surface and then stays constant throughout the channel. This results in a flat flow profile that is called plug flow. Figure 2.3b shows an illustration of the plug flow.

This phenomenon can be simplified by approximating the diffuse layer with a sliding wall boundary condition, which has a saturated electroosmotic velocity given by the Helmholtz-Smoluchowski slip velocity [52]:

$$u_w = -\varepsilon \psi_w E / \eta, \quad (2.24)$$

where ψ_w is the surface potential on channel walls, E is the external electric potential, and η is the dynamic viscosity.

2.3.5 Electrophoresis

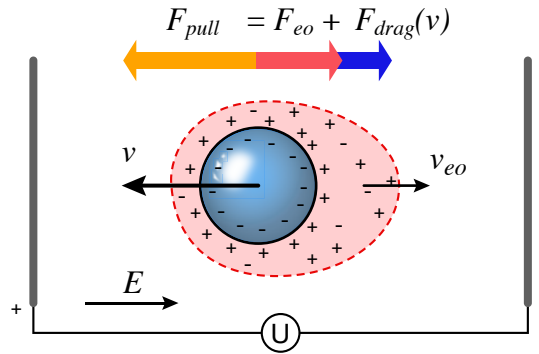


Figure 2.4: Illustration of electrophoresis: a charged particle moves in an external electric field, E . Charges on the surface of the particle exert an electrostatic force, F_{pull} . The same charges attract a cloud of counter-ions in the diffuse layer. This layer has opposite charges that migrate towards the opposite electrode. This migration induces a flow v_{eo} that exerts a viscous drag on the particle, F_{eo} . The force difference moves the particle to the left and force balance is achieved by viscous drag, $F_{drag} = \zeta v$.

Electrophoretic migration of charged particles comprises of electrostatic force and electroosmotic drag as illustrated in Figure 2.4 [51]. The electrostatic force drives the particle towards the electrode on the left with a force $F_{pull} = qE$. The same charge induces a double layer around the particle, shown in red. The charges in the double layer are positive, and thus, they migrate towards the right electrode. As a result, there is an electroosmotic flow on the particle surface

that exerts a viscous drag on the particle, F_{eo} . To distinguish between this electroosmotic flow and the flow on the channel walls, we call the former electrophoretic backflow. The difference between the two forces drives the particle to the left at a terminal velocity $v_{ep} = (F_{\text{pull}} - F_{eo})/\zeta$. The exact expression for this velocity depends on the flow profiles. For large particles in the bulk ($\lambda_D \ll a$), it is $v_{ep} = \varepsilon \psi_p E / \eta$, where ψ_p is the surface potential on the particle [51].

When considering electrophoresis inside channels, one must also take into account the electroosmotic plug flow, because the electric field induces both phenomena. In experiments, the particle and the channel have a charge of the same sign to prevent sticking. In such cases, the two effects act in opposite directions, with a net velocity given by

$$v_{net} = v_{ep} + v_{eo} \approx \frac{\varepsilon E}{\eta} (\psi_p - \psi_w) \approx \sqrt{\frac{\varepsilon k_B T}{2e^2 c_0}} \frac{E}{\eta} (\sigma_p - \sigma_w) \propto \frac{E}{\sqrt{c_0}} (\sigma_p - \sigma_w), \quad (2.25)$$

where σ_p and σ_w are surface charge densities on the particle and the channel, respectively. The second equality is only approximate since the confinements introduces a correction pre-factor that was calculated by Keh and Anderson [53, p. 437]. In the third equality we used Equation (2.23) and (2.22). The final expression suggests that electrophoretic velocity in channels is proportional to the electric field strength and the surface charge difference. It also suggests that velocity decreases with salt concentration.

2.4 Relevance of our model system

Throughout this thesis, we study the idealised model system that has characteristic dimension of $\sim 1 \mu\text{m}$. However, channels and particles found in nature have a wide range of sizes and shapes, as it was shown in Figure 1.1. Therefore, we discuss how shape impacts particle behaviour, and how the relevant physics changes at different length-scales.

Particle shape does not fundamentally change the hydrodynamics, because the flow pattern in far field is almost the same as for spherical particles [39, p. 141]. In bulk, the modified Stokes' law is $F_d = -6\pi\eta aKv$, where K is the correction constant that depends on the exact geometry of the particle. For example, an oblate ellipsoid with a minor/major principal axes ratio of 0.5 has $K(a/c = 0.5) = 0.9$, while a prolate ellipsoid has $K(a/c = 2) = 1.2$ [39, p. 149]. This illustrates that the deviations away from the spherical solution are small, thereby justifying the usage of spherical particles as model systems. For flexible particles, like DNA polymer, physics becomes more involved since the flow can deform them and they also have internal degrees of freedom, resulting in entropic effects. Nevertheless these differences, the same formalism is often applied to get an idea for polymer behaviour in channels [40].

Now consider scaling laws [54]. First, Brownian motion does not scale with the particle size, i.e. it is much more significant for small particles. Formally, the diffusion coefficient scales as $D \propto 1/a$, while Brownian trajectory scales as $\text{MSD} = \langle \Delta x^2 \rangle \propto t$.

For electrostatics, the velocities scale linearly with the applied electric field and are independent of the dimensions. These results are valid in the limit $\lambda_D \ll a$. For smaller systems, corrections must be introduced to account for significant geometric curvature. Furthermore, overlapping diffuse layers might introduce new effects that we are not probing with our analysis.

Hydrodynamics is scale invariant at low Reynolds numbers [39], meaning that results can be scaled up or down without changing the underlying physics. However, in biological protein pores, the diameters are sometimes below 1 nm, while water molecules are around 0.3 nm, raising questions about the continuum approach to hydrodynamics. This problem has been studied by comparing the continuum solutions with molecular dynamics simulations [55]. Both models show similar trends and good quantitative agreement for smooth liquid-solid interfaces. Meanwhile, for rough interfaces the solutions deviate, but they still share qualitative features [56, p. 186]. Further support comes from studying biological nano-channels called aquaporins, where the continuum equations successfully predict the permeability of the channels [11]. Such agreements are somewhat expected since the Navier-Stokes equation is built on conservation laws, which must be satisfied even at the molecular level [57]. All this suggests that the continuum equations can describe systems down to a few nanometers. Therefore, our model system probes physics relevant even for nano-channels.

Chapter 3

Brownian Motion in Channels

This chapter introduces our experimental method for studying the hydrodynamic interactions inside channels, and then present a simple experimental investigation of Brownian motion of isolated particles in these microfluidic channels. Specifically, diffusion coefficients are determined from experimental trajectories of colloidal particles. To understand these measurements, we introduce a numerical method for calculating diffusion coefficients. Finally, we show that finite channels have a higher diffusivity than previously thought by comparing our experimental results with the simulations.

3.1 Method for microfluidics experiments

Our model system is implemented experimentally using microfluidic lab-on-a-chip devices that have two reservoirs connected by narrow channels. These chips are filled with a dilute solution of spherical polystyrene colloidal particles (details to follow). Figure 3.1 shows a schematic illustration of such a chip and a microscope used to record the particle motion.

The chip is mounted on a custom built, inverted bright-field microscope with 100 \times , NA 1.4 objective (UPLSAPO, Olympus). The position of the sample can be adjusted using micrometers drive or a piezo nano-positioning stage (model PI P-561.3CD). Particle motion in the microfluidic chip is recorded using either a CCD Mikrotron MC1362 camera or CMOS Imaging Source DMK-31BF03 camera. We switched to the Mikrotron camera in later experiments since it can record at high frame rates, which is necessary for driven transport experiments. Finally, particle positions are extracted using a semi-automatic image analysis method. In the rest of this section, we will describe a fabrication process for the microfluidic chips and also the image analysis.

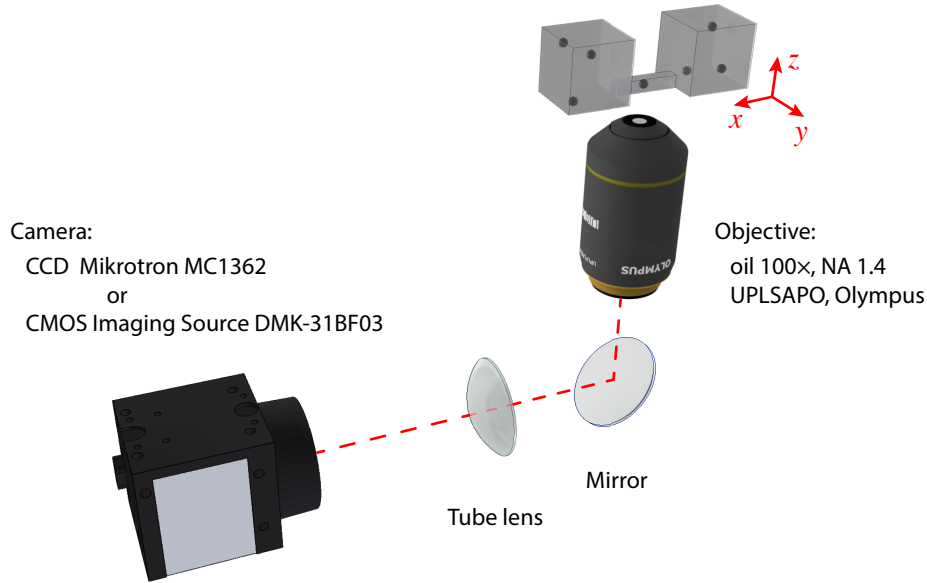


Figure 3.1: Setup diagram: the microfluidic chip is mounted on a custom built inverted bright-field microscope. The sample can be moved along the three axes via nano-positioning stage.

3.1.1 Fabrication

The microfluidic chips are produced using a PDMS replica moulding technique [58]. First, we create an impression of channels on a silicon substrate, as shown in Figure 3.2a. This is achieved via focused ion beam (FIB) deposition of platinum [58] or via e-beam lithography followed by a reactive ion etching¹. FIB based deposition typically produces channels with a semi-elliptical cross-sections, as revealed by SEM image in Figure 3.3d. Meanwhile, the e-beam lithography method produces rectangular channels of arbitrary length, see Figures 3.3a-c. In early experiments, we used FIB method, but later we switched to e-beam lithography method. Table 3.1 lists the dimensions of channels alongside their unique identification name.

In the second step, we deposit a pattern of the reservoirs and access connections, as shown in Figure 3.2b. This is achieved using conventional photolithography on a 10 μm thick layer of AZ 9260 polymer, which was spun coated directly onto the substrate [58]. Then a pattern is exposed through a Cr/quartz mask (Photodata Ltd, Hitchin, UK) and developed². Figure 3.4 shows three different pattern designs. In all of them, the channels are aligned across the barrier that separates the two reservoirs, where the width of the barrier determines the length of the channels. The reservoirs are connected to two inlets each: one inlet is used for injecting

¹The FIB method was developed and performed by Stefano Pagliara, while the e-beam method was developed and performed by Vahe Tshitoyan. Details are provided in Appendix B.1.

²The photolithographic layer was deposited in a clean room by Stefano Pagliara.

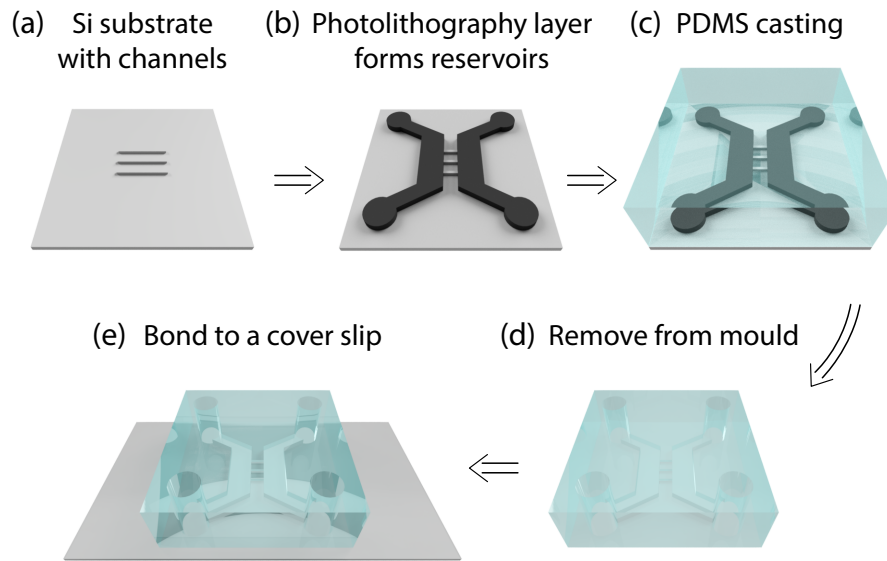


Figure 3.2: Preparing lab-on-a-chip devices using PDMS replica moulding technique. (a) Narrow channels are fabricated on a silicon substrate via FIB or e-beam lithography [58]. (b) Reservoirs and large access channels are deposited using photolithography patterning of an AZ 9260 polymer. (c) The finished master mould is replica moulded by PDMS casting. (d) After curing, the PDMS chip is separated from the mould and the inlet holes are punched. (e) Finally, the PDMS chip is bonded to a glass cover slip by activating the surface with a plasma oven.

the solution, while the air escapes through the other one. In the designs (a) and (b), we place additional connections between the reservoirs that facilitate pressure equilibration. The complete two-layer structure forms a master mould, containing a negative impression of our experimental structure.

The third step is PDMS casting, as shown in Figure 3.2c. Polymer polydimethylsiloxane (PDMS) is mixed with a curing agent in a ratio 9:1, and degassed in a vacuum desiccator for around 20 minutes. Then the mould is placed facing upwards in a container and covered with the PDMS mixture. Curing is accelerated by baking it at 70 °C for 60 minutes.

In the fourth step, we carefully remove the cured PDMS from the mould. Empirically, we noticed that leaving the PDMS replicas in air improves the reproducibility of our experimental results. Therefore, the PDMS is left in air for at least two days before proceeding. Afterwards, we punch inlet holes using biopsy punch tool (1.5 mm, BPP-15F by Kai medical).

Finally, the PDMS is plasma bonded to a glass coverslip, as shown in Figure 3.2e. The glass coverslip (thickness 0.13 mm-0.16 mm, Glaswarenfabrik Karl Hecht GmbH & Co) is cleaned by sonicating for 20 minutes in Hellmanex 3 soap solution, then flushing it five times with deionised water, and sonicating it again for 20 minutes in isopropanol. The PDMS chip is cleaned by blowing with a compressed nitrogen and then carefully sticking and removing a

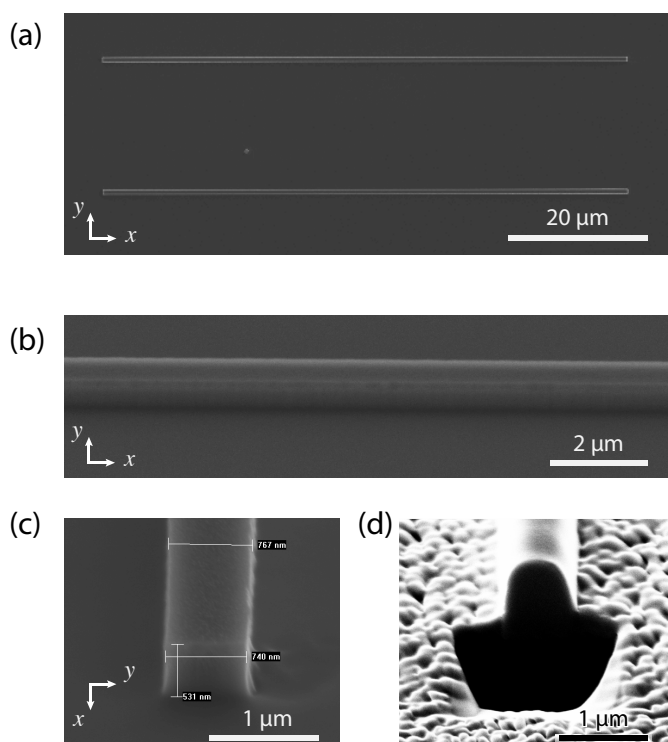


Figure 3.3: Scanning electron microscope (SEM) images of channels on a substrate. (a), (b) and (c) show channels etched in silicon that were made using the e-beam lithography method. These channels are 75 μm long, 0.8 μm wide and tall, and are spaced 20.8 μm apart. They have a rectangular cross-section, as seen from (c). (d) shows platinum channel deposited using the FIB method. It has a semi-elliptical cross-section (image kindly provided by Stefano Pagliara). Image (a) is taken at 0 deg angle, while (b), (c) and (d) are taken at 45 deg angle.

Name	Length (μm)	Type	Width (nm)	Height (nm)	Connections
B4-5um	5	Square	800 ± 40	800 ± 40	Small
B4-13um	13	Square	800 ± 40	800 ± 60	Small
B4-25um	25	Square	800 ± 40	850 ± 30	Small
S1-7um	7	Square	800 ± 40	800 ± 60	Large
B2-30um	30	Square	800 ± 30	850 ± 30	No
B2-10um	10	Square	890 ± 30	630 ± 60	No
S1-5um	5	Elliptical	850 ± 100	900 ± 100	Large
S2-5um-1	5	Elliptical	1020 ± 130	1100 ± 150	Large
S2-5um-2	5	Elliptical	1150 ± 130	1100 ± 150	Large
S2-5um-3	5	Elliptical	1150 ± 130	1100 ± 150	Large
S3-10um	10	Elliptical	800 ± 100	950 ± 100	Large

Table 3.1: Table of moulds used for PDMS replica moulding. Dimensions were measured using SEM or AFM. We use a naming convention to identify channels from the same mould. The name comprises of three components separated by a dash. The first two symbols indicate the design of photolithographic layer that are shown in Figure 3.4: S1, S2, and S3 correspond to design (a); B4 corresponds to design (b); and B2 corresponds to design (c). The second number indicates the width of the barrier, which is equal to the length of the channels. The third number identifies the channel on the chip. Normally, each chip has multiple channels for redundancy.

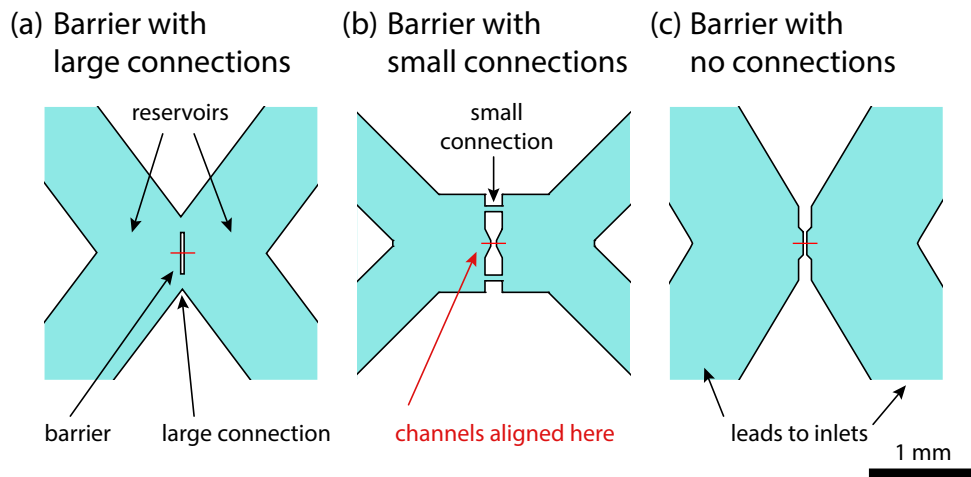


Figure 3.4: Designs for photolithography layers that contain two reservoirs separated by a barrier of width L . The red line indicates where the layer with channels is aligned. (a) Has been designed by Stefano Pagliara and it contains large connections between the reservoirs that facilitate pressure equilibration. In design (b) the connections have been moved further away from the channels and made smaller ($50 \mu\text{m}$ wide). This allows applying predictable pressure or electric potential across the barrier. Design (c) contains no secondary connections.

piece of Scotch tape. Immediately afterwards, the coverslip and PDMS are placed in a plasma oven (Diener Femto, 40 kHz). Here, their surfaces are treated with an oxygen plasma for 10 seconds at power 100 W and gas flow rate of 25 sccm. After plasma treatment, the PDMS is placed onto the glass coverslip, where the activated surfaces form a permanent bond between the PDMS and the glass [59].

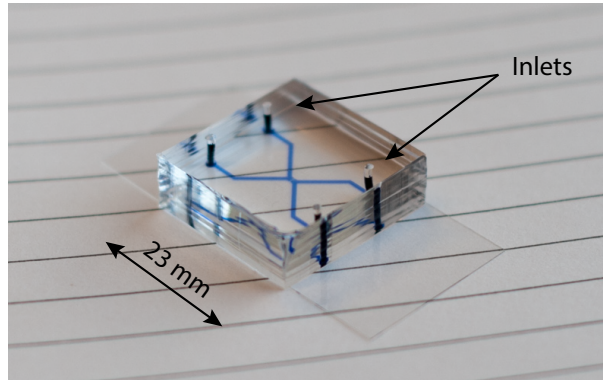


Figure 3.5: Photograph of the completed microfluidic chip. It was filled with blue ink to highlight where the liquid is.

A completed microfluidic chip is filled by injecting a solution with a syringe in each inlet. The solution contains deionised water, 5 mM KCl salt and colloidal particles that are roughly spherical and made of polystyrene. We used two batches supplied by Polysciences Inc., with diameters of 505 ± 8 nm and 510 ± 10 nm (catalogue id 07307). Figure 3.5 shows a completed chip. Finally, pieces of Scotch tape are placed onto the inlets to reduce evaporation.

The chip is then mounted on an inverted bright-field microscope ($100\times$, 1.4 numerical aperture; UPLSAPO, Olympus), and the subsequent particle motion is recorded using a CMOS camera (DMK-31BF03, Imaging Source) or a CCD camera (Mikrotron MC1362).

3.1.2 Particle tracking

Particle trajectories are extracted from the acquired videos using an image analysis procedure [60]. Here, we describe this semi-automated process and then follow it up with detailed discussions on two vital components: sub-pixel localisation algorithm and position linking algorithm.

Figure 3.6a shows a typical bright-field image. The large structure in the middle is the barrier that contains three horizontally positioned channels. The bright blobs are particles, where our goal is to estimate their positions in $\hat{x}\hat{y}$ plane. For this, we must extract a foreground image that contains information only about the particles by subtracting a background image from the raw image.

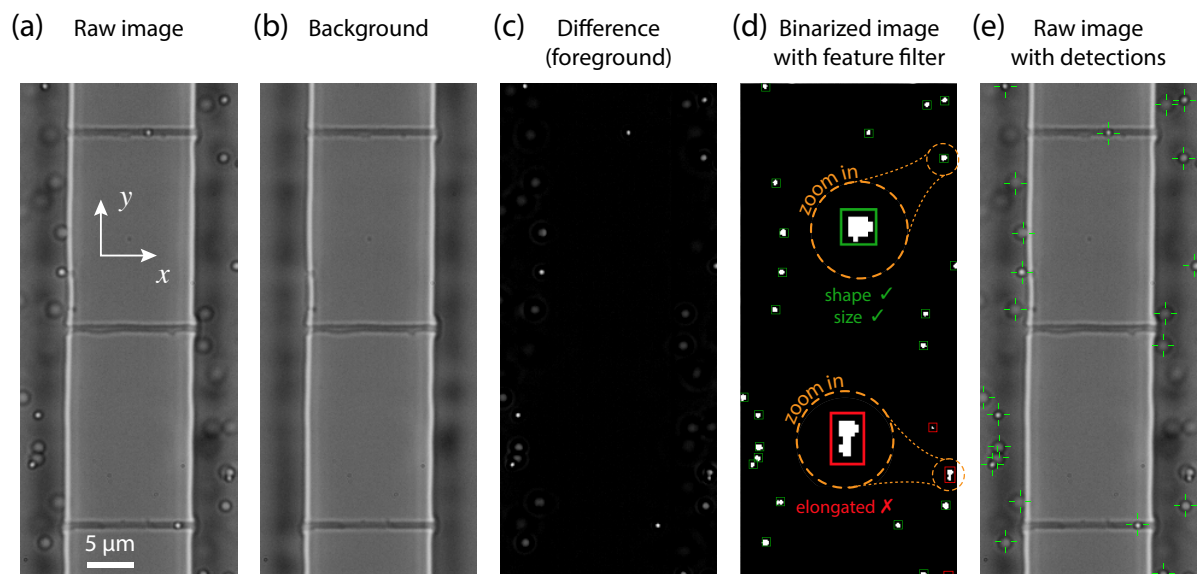


Figure 3.6: Illustration highlighting the particle detection procedure. First, the background image (b) is estimated from multiple raw images. It is subtracted from the raw image to give the difference (c) that contains information about moving particles. This image is binarized (d), which allows identification of particles of round shape and expected size – indicated by the green boxes. If a detected blob does not fit the particle criteria, it is discarded, as shown by the red boxes. Finally, the precise positions of selected blobs are determined using a sub-pixel localisation algorithm. The result is shown in (e).

The background image contains information about the stationary objects that do not change throughout the measurement, i.e. the barrier and average illumination. Separating the background from foreground image is a classic problem in the field of image analysis, where we are dealing with the case of stationary background with a low number of foreground objects [61]. The background can be estimated from a stack of images by taking the median pixel values. It works well since most of the time there is no particle in a given position. The resulting image has no ghosting artefacts at a moderate computation cost. To improve the performance, we use a subset of images picked randomly from an experiment video. Empirically, we found that 500 images produces a satisfactory background image at small computational cost (takes about 10 s to compute). The resulting background image is shown in Figure 3.6b.

Figure 3.6 shows the resulting foreground image, where the blobs correspond to particles. However, the image also contains undesirable features, such as clusters of particles, noise or an occasional artefact. To separate them from the particles, we binarize the image and then analyse the resulting blobs, as shown in Figure 3.6d. Specifically, we check that particle size is in an expected range, and the shape is roughly circular, because elongated shapes typically correspond to clusters or contaminations. If one of these tests fails within the channel, we omit that image from the final analysis to avoid influencing our measurement.

The typical values for this analysis are: binarization threshold at 0.15; particle size range from 10 px to 30 px; maximum elongation set to 0.4, where it is defined as $1 - \text{width}/\text{height}$. However, these values are manually tuned for each experiment to include only single particles in our detection algorithm.

Next, the position of the particle is estimated using a sub-pixel localisation algorithm. For this, the foreground image is cut to a rectangular boxes that enclose the binarized blobs, as shown by the green boxes in Figure 3.6d. For each box, we find the intensity peak that corresponds to particle position, using a method called sub-pixel localisation algorithm. Figure 3.6e shows the estimated positions superimposed on the raw image. A detailed description of sub-pixel localisation is presented on page 28.

Finally, the positions are linked into trajectories using a hybrid linking algorithm. Analysing the trajectories instead of the raw positions enables identification of particle tracking mistakes. We provide details of our linking algorithm on page 32.

Sub-pixel localisation

In bright-field micrograph, particles appear as bright blobs, as shown in Figure 3.7. Here, we aim to determine their position with the maximum accuracy. A naive approach is to take the brightest pixel in the blob for the position, which has tracking error of one pixel width. However, we can do better by utilising the information in the intensity profile to obtain higher spatial

resolution. As the name suggests, sub-pixel localisation allows to determine the particle's position to within a pixel in camera's sensor. This approach is similar to blob fitting used in super-resolution microscopy [62, 63]. Here, we explain the technical details behind our approach.

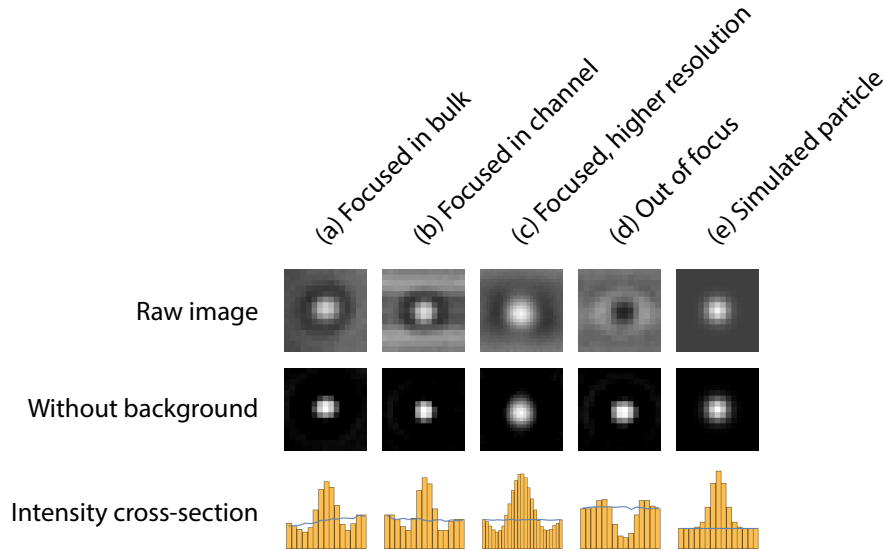


Figure 3.7: Bright-field microscopy images of 500 nm wide polystyrene particles. The first row shows unprocessed images from camera sensors, while the second row shows the same image with subtracted background, leaving only the information about the particle. This image is used for sub-pixel localisation. The third row shows light intensity, along a horizontal line in the images on the first row. The blue lines indicate the background image. (a) and (b) images are almost identical after subtraction of the background. (c) has higher resolution due to higher pixel density on the Imaging Source CMOS camera. (d) particle is out of focus. It can be tracked by subtracting the background and then inverting the brightness, which gives a familiar bright blob. (e) is a simulated particles with a Gaussian shape and a peak to baseline intensity of 50%.

Figure 3.7 (b) and (c) show the typical blobs we observe in channels: approximately round with smoothly decaying intensity profiles. Literature suggests that the best accuracy can be achieved by fitting a Gaussian function to the intensity profile [62]. We tested this hypothesis by comparing the performance of different algorithms against simulated particles, which have a Gaussian profile with realistic width and noise. Figure 3.7e shows an example of simulated particles. Errors of the fitting algorithm are assessed by computing the mean squared difference between the fitted position and the simulated position.

We consider these algorithms: a weighted centroid algorithm, a radial center algorithm [64], fitting to a fixed 2D Gaussian, and fitting to a general 2D Gaussian function. Out of these, the Gaussian fitting methods outperforms the other two by an order of magnitude for the simulated

Algorithm	Computation time	Localisation error
Weighted centroid	4.2 s	0.1820 px
Radial center [64]	68.1 s	0.0800 px
Fixed 2D Gaussian (Levenberg-Marquardt)	31.9 s	0.0103 px
General 2D Gaussian (Conjugate Gradient)	721.8 s	0.1010 px
General 2D Gaussian (Gradient)	135.1 s	0.0142 px
General 2D Gaussian (Quasi-Newton)	459.3 s	0.0140 px
General 2D Gaussian (Newton)	481.2 s	0.0078 px
General 2D Gaussian (Levenberg-Marquardt)	70.5 s	0.0072 px

Table 3.2: Comparison of sub-pixel fitting algorithms. Each algorithm was tested using a set of 10000 simulated Gaussian particles with noise $\sigma_N = 0.004$ and peak to baseline intensity of 50%.

data. See Table 3.2. The performance was comparable between the two Gaussian functions. Both functions measured the width of the intensity distribution, but the general Gaussian fitting allowed to estimate the elongation and the direction. This information is useful for identifying tracking mistakes or artefacts in experiments, and therefore, we used the general 2D Gaussian function to find particle positions.

Fitting the general 2D Gaussian function to the experimental data involves finding six free parameters. This is a multidimensional optimization problem that does not have a universal solution. To aid the search, we provided an initial approximate position from the centroid method. We tested a few different multidimensional search algorithms that are listed in Table 3.2. The best results are produced by the Levenberg-Marquardt method. We, therefore, use the Levenberg-Marquardt method and fall back to fixed 2D Gaussian, if the fitting does not converge. The code for our implementation is available at [65].

We assess the accuracy of our chosen sub-pixel localisation algorithm by running the simulation for realistic noise levels. Figure 3.8a shows the localisation errors as a function of a Gaussian noise that is added on top of simulated particles. Not surprisingly, the accuracy worsens with higher noise. We measured the noise levels in our experimental setup by recording the PDMS/glass interface that has no motion. Then we subtracted the background image and measured the leftover intensity variation. It was $\sigma_N = 0.004$ for the Mikrotron camera and $\sigma_N = 0.007$ for the Imaging Source camera (noise is unitless since camera measures a relative luminosity in a range $[0, 1]$). These noise levels are marked on in Figure 3.8a as red lines. From the plot, the corresponding errors are $\sigma_{static} = 0.0072$ px and $\sigma_{static} = 0.0108$ px, respectively. Please note that errors have normal distributions and the reported values are standard deviations. Figure 3.8b shows an error distribution that follows a Gaussian distribution with no directional bias. Table 3.3 summarises these results. The tracking errors in our experiments are expected to

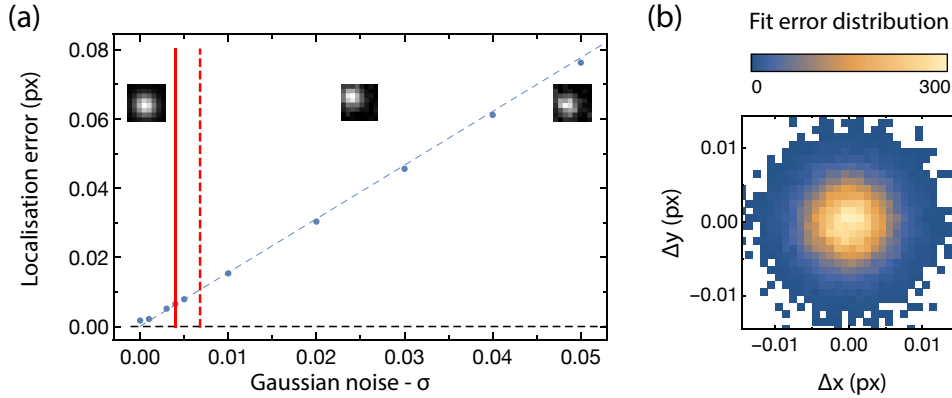


Figure 3.8: Simulation of noise impact on the subpixel localisation algorithm. (a) Average localisation error as a function of noise levels in a simulated image. For each data point a set of 10000 simulated normal particles was fitted using the “SPFGaussianOptimised” function [65]. The errors increase almost linearly with noise, as indicated by a linear fit (dashed blue line). The red lines indicate noise levels measured in the experiments. (b) Distribution of errors in 2D for Gaussian noise levels of $\sigma_N = 0.004$. The image confirms that the majority of errors are within $2\sigma_{static} \approx 0.01$ px and have no directional bias.

Camera	Pixel density	Typical noise	Expected error	Measured error
Mikrotron MC1362	128 px/ μm	0.0040	0.96 nm	–
Imaging Source DMK	60 nm/px	0.0067	0.68 nm	1.7 nm

Table 3.3: Static tracking errors for two different cameras. The expected errors are simulation results for the given noise.

be higher, since the particles are not exactly Gaussian and there is motion blur, which produces dynamic tracking errors [66].

To assess the tracking accuracy in crowded situations, we run the same simulation with two particles near each other. In this case, the second particle is placed randomly around the original particle at a distance from 4 to 7 px. Resulting tracking error increases to $\sigma_{static} = 0.234$ px, because the second particle biases the Gaussian fit [67]. For real data, the errors might be a bit smaller as there is a dark ring around the particles that increases the contrast. Nonetheless, we consider this value to be the limiting accuracy when other particles are close [68].

Finally, we test the accuracy with real particles using a piezo positioning stage. In this experiment, a colloidal particle is attached to the glass surface and the sample is loaded on the piezo stage (model PI P-561.3CD) that allows moving the sample in increments of 5 nm, 10 nm, or 20 nm. The resulting image is tracked with our sub-pixel localisation algorithm and

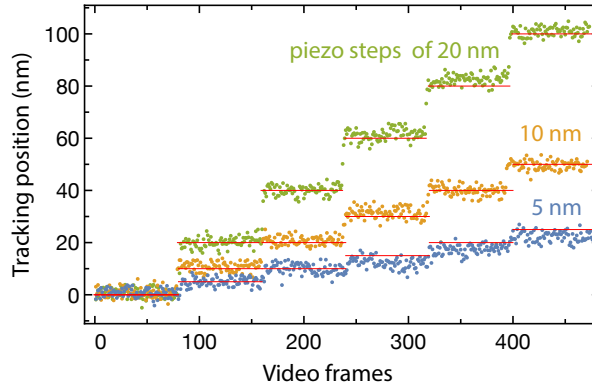


Figure 3.9: Assessment of the sub-pixel fitting algorithm by tracking a fixed particle that was moved with a piezo stage. The stage was moved in 3 second intervals with step sizes of 20 nm, 10 nm and 5 nm, respectively. The red lines show the expected positions for the piezo stage. From the plot, we can easily identify all the steps, but the position tracking has variation around the mean positions: $\sigma_x = 1.7$ nm. Experiments performed together with Yizhou Tan.

the results are shown in Figure 3.9. All steps can be identified. Within each step, the position variation around the mean value is $\sigma_x = 1.7$ nm (for ImagingSource camera with a pixel size of 60.3 nm). This corresponds to errors of 0.028 px, which is a factor of three worse than predicted by our simulations. This value is our best estimate for the static tracking errors. However, it does not account for the dynamic tracking errors [66].

Trajectory linking

Positions are linked together into trajectories, using a hybrid method: the nearest neighbour linking combined with the global optimization [63, 69]. Briefly, the algorithm connects positions that are unambiguous, i.e. the consecutive frame contains a single particle in the immediate proximity (5 px). If there are more than one particle or the particle number changes, multiple combinations of links can be made, but only one corresponds to physical trajectory. To find it, we minimise a cost function: $k_x|\mathbf{x}_1 - \mathbf{x}_0| + k_t(t_1 - t_2)$, where \mathbf{x} is the position, t is the frame number and k_x, k_t are weighting coefficients [63, 69]. For our application, we found values $k_x = 1$ and $k_t = 2$ to produce satisfactory results. The global minimum of the cost function is found using the Hungarian assignment algorithm [70]. This linking algorithm is tested by visual inspection of the trajectories.

We keep track of errors that occur throughout the image analysis. For example, if the sub-pixel localisation algorithm fails to converge, it raises a flag that allows us to come back to that image for inspection. Other monitored errors come from particle shape filter that we described earlier, and the trajectory linking algorithm that raises a flag when there is a time gap in the trajectory. In a typical experiment, almost all the errors come from particles exiting the

field of view since their shape gets cut in half; or from two particles being too close to resolve. The next most frequent error ($\sim 5\%$ of the cases) is due to particle clusters, while other errors are rare (less than 1%). As a result, we understand where and when the problems occur in our trajectories.

3.2 Brownian motion experiments

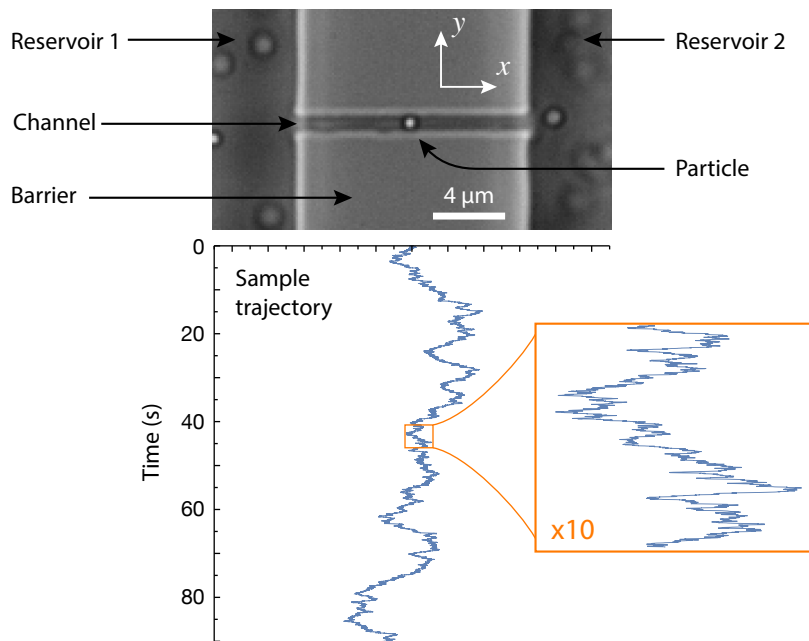


Figure 3.10: Bright-field microscopy image of a channel with a single colloid inside. The graph below shows a typical trajectory in \hat{x} , where the particle performs Brownian motion in 1D.

We use the experimental methods described above to study passive Brownian motion in channels. Figure 3.10 shows a typical image taken with our microscope and the subsequent trajectory of that particle. This particle performs an unbiased random walk, with no net progress $\langle x \rangle \approx 0$. The mean squared displacement (MSD) grows linearly in time as expected for Brownian motion, as shown in Figure 3.11. The red line indicates a linear fit, where the slope gives a diffusion coefficient of $D_x = 0.152 \mu\text{m}^2/\text{s}$. This value is much smaller than the diffusion coefficient in bulk, $D_0 = 0.876 \mu\text{m}^2/\text{s}$, due to increased hydrodynamic friction inside the channel.

Table 3.4 gives diffusion coefficients for the different channels that we used throughout this thesis. Please note that values fluctuated as much as 15% between experiments, which can be attributed to the small differences in channel shape and temperature fluctuations. The channel

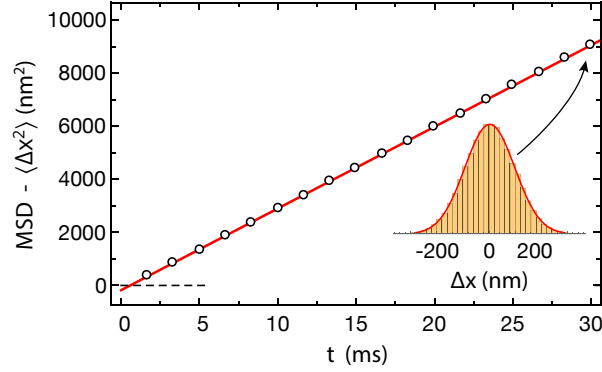


Figure 3.11: Mean squared displacement (MSD) as a function of time. Experiment performed with a single particle of diameter $2a = 510\text{nm}$ inside a channel of length $L = 13\mu\text{m}$. Red line shows a linear fit where the slope gives the diffusion coefficient: $D_x = 0.152 \pm 0.06\mu\text{m}^2/\text{s}$; the offset is -154.9nm^2 , which can be attributed to particle tracking errors [60, 66, 71]. The inset shows histogram of displacements after 30 ms, where the red lines indicates a fit to a normal distribution.

Date	L (μm)	$2a$ (nm)	a/R	D_x ($\mu\text{m}^2/\text{s}$)	D_x/D_0
2015-12-09	5	510	0.56	0.181	0.202 ± 0.020
2015-12-09	5	510	0.56	0.173	0.192 ± 0.020
2015-02-16	10	505	0.60	0.110	0.126 ± 0.006
2016-03-30	10	510	0.61	0.101	0.116 ± 0.010
2015-11-24	13	510	0.56	0.153	0.176 ± 0.010
2015-12-07	13	510	0.56	0.150	0.172 ± 0.010
2015-11-28	13	510	0.56	0.152	0.174 ± 0.010
2015-11-28	13	510	0.56*	0.169	0.193 ± 0.010
2015-12-11	25	510	0.55	0.152	0.173 ± 0.010
2015-12-11	25	510	0.55	0.152	0.173 ± 0.010

Table 3.4: Diffusion coefficients for isolated particles inside channels. Measurements performed on the same day are values for different channels. The star highlights the channel B4-13um-2, which is wider than the nominal value. See Section 3.2.2.

shape varies due to a subtle differences in PDMS replicas or the PDMS/glass bonding strength. We tried to minimise this variation by following the procedure described in Section 3.1.1. In turn, the diffusion coefficients are affected by the variation of the confinement ratio [40].

Diffusion coefficients depend on the temperature as given by the Einstein-Smoluchowski relation in Equation (2.4). In addition to the linear temperature term, the hydrodynamic friction is a function of the dynamic viscosity, which varies strongly with temperature [72]. This affects the diffusion coefficient, making it difficult to compare between experiments. Therefore, we normalise the reported coefficient values with the theoretical bulk value $D_0 = k_B T / 6\pi \eta a$, which eliminates both contributions to the temperature dependence. In the experiments, the temperature was measured using a thermocouple placed close to the microscope (typically it was 21.5 °C, but occasionally varied as much as 2 °C).

3.2.1 Spatially resolved diffusion coefficients

The diffusion coefficients reported in Table 3.4 are averaged within the channel. Here, we present a measurement of spatially resolved diffusion coefficients inside and around the channels. This method was predominately developed by Stefano Pagliara and Simon Dettmer, where Simon Dettmer performed the experiments. Our results were reported in [73].

To achieve high spacial resolution, the frame rate of the Mikrotron camera was increased to 500 fps or $\Delta t = 2$ ms, thus minimising the area that particles explores. The diffusion coefficient can be estimated from three consecutive frames, as reported in [60, 66, 71]. These three points translate to two MSD points, which is sufficient to determine the slope and minimises the area explored by the particle. For example, the three point measurement takes 6 ms that translates to $\sqrt{2D_x t} \approx 60$ nm. With this spacial resolution, we group the measurements into boxes based on the average position. These boxes were picked to match the pixel size: 129 nm \times 129 nm. Figures 3.12 (a) and (b) show the resulting diffusion coefficient maps for \hat{x} and \hat{y} directions, respectively. This is the only time that we consider the diffusion coefficient in \hat{y} direction.

From the figure, we can see that the diffusion coefficients decrease when they enter the channels. Inside, D_x is uniform along the \hat{x} axis – see the projection shown in Figure 3.12c. We will exploit this symmetry in our analysis further on. The variation of D_x along the \hat{y} axis is small, which will be explained using simulations in Section 3.4.

3.2.2 Channel dimensions

The particle-channel interaction and the corresponding diffusion coefficients critically depend on the confinement of the particle. Theoretical models typically consider ideal cylindrical channels that have a well-defined width, $2R$ [39]. Meanwhile, our experimental channels have

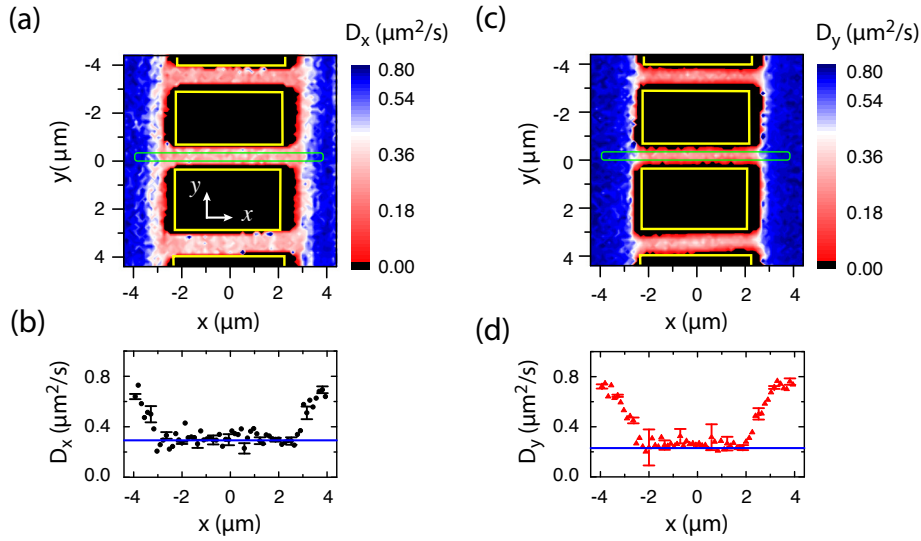


Figure 3.12: Localised diffusion coefficients for channels of length $L = 5 \mu\text{m}$ (S2-5um). (a) and (b) show the diffusion coefficient map for \hat{x} and \hat{y} directions, respectively. The yellow boxes highlight the barrier. The diffusion coefficients decrease just before entering the channels. (c) and (d) show diffusion coefficients along the channel as highlighted with the green boxes above. The data for this figure was collected by Simon L. Dettmer and reported together in [73].

rectangular or semi-elliptical cross-sections, as shown in Figure 3.3. In both cases, we kept the ratio between width and height close to one, so that the experimental channels would be closer to the theoretical ones. Furthermore, we define an effective radius, R , to quantify the size of our experimental channels. It is defined as a cylindrical channel with the cross-section area matching the experimental channel. For semi-elliptical cross-sections, it is $R = \sqrt{WH/4}$, where W is the channel width and H is the channel height. For rectangular channel cross-sections, it is $R = \sqrt{WH/\pi}$. The impact of this approximation will be studied in Section 3.4.1 and additional information is available in the literature [74, 75].

Table 3.5 reports the effective channel dimensions, which were estimated from the SEM images. However, some channels are consistently wider than expected (measurement method described later). This might be due to in inaccurate SEM measurement or a residue accumulation on the mould. Specifically: the channel B4-13um-2 has a small localised defect that widens the channel by $100 \pm 60 \text{ nm}$; channels in chip B4-25um are $30 \pm 30 \text{ nm}$ wider in the middle than at the outlets.

An independent measurement for a channel width is obtained from the particle trajectories. Figure 3.13 shows a 2D density histogram for particle detections superimposed on top of a micrograph of the same channel. The height of the histogram is around 305 nm. To get the width of the channel, we must add the excluded volume and few Debye lengths for electrostatic

Name	L (μm)	Effective R (nm)	a/R
B4-5um-4	5	451 ± 20	0.564 ± 0.026
B4-13um-2	13	451 ± 20	0.564 ± 0.027
B4-13um-5	13	451 ± 20	0.564 ± 0.027
B4-25um-3	25	465 ± 15	0.548 ± 0.020
B4-25um-4	25	465 ± 15	0.548 ± 0.020
S1-5um-1	5	437 ± 35	0.577 ± 0.048
S2-5um-1	5	530 ± 50	0.476 ± 0.045
S2-5um-2	5	562 ± 50	0.449 ± 0.040
S2-5um-3	5	562 ± 50	0.449 ± 0.040
S1-7um-2	7	451 ± 20	0.564 ± 0.027
S3-10um-1	10	424 ± 35	0.595 ± 0.051
B2-10um-1	10	422 ± 21	0.604 ± 0.033
B2-30um-1	30	465 ± 15	0.548 ± 0.020

Table 3.5: Channel properties: lengths and effective widths. The confinement ratio was estimated using $2a = 505 \text{ nm}$ or $2a = 510 \text{ nm}$, depending on which colloids were in that channel. The naming convention is explained in Table 3.1.

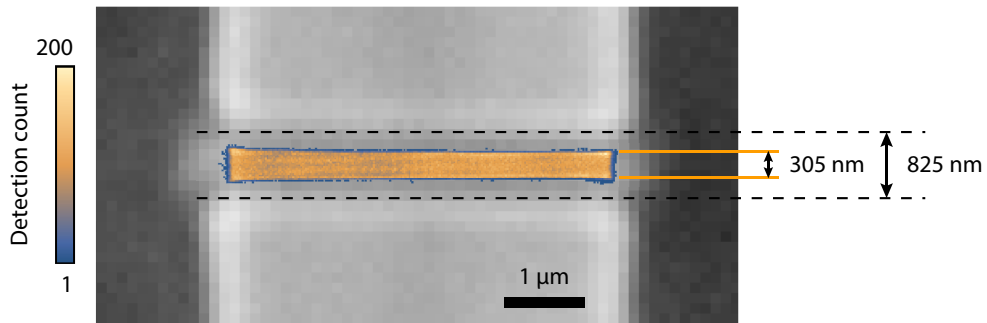


Figure 3.13: Density histogram of particle positions overlaid on top of the channel picture. The histogram was computed from 496'000 points in a channel of length $L = 5 \mu\text{m}$ (B4-5um-4). The width of the histogram is $305 \pm 40 \text{ nm}$. The closest proximity between particle centers and the channel walls is $a + \lambda_D$. Then the width of the channel can be estimated by adding these back to the histogram width. The estimated channel width is $825 \pm 60 \text{ nm}$, which is close to the SEM measurement of 800 nm .

repulsion: $2a + 2\lambda_D$. Therefore, the width estimate is 825 ± 60 nm, which compares well with the nominal width of 800 nm.

3.3 Method for hydrodynamic simulations

To interpret the experimental data, we compare it with hydrodynamic models. However, these models can be analytically solved in only a few cases, and thus, we rely on numerical simulations to make quantitative predictions about the hydrodynamics inside channels. Here, we explain our method behind these simulations.

We solve Stokes' equation, given by Equation (2.10), using a numerical solver called COMSOL Multiphysics V4.4. Briefly, it uses the finite element method, which discretises the geometry into a mesh of small elements. For each element, the physical equations are solved and updated iteratively until they converge to a solution [76, 77]. COMSOL is a commercial package with optimised numerical solvers, allowing us to focus on the physics, while leaving the technical details to the software.

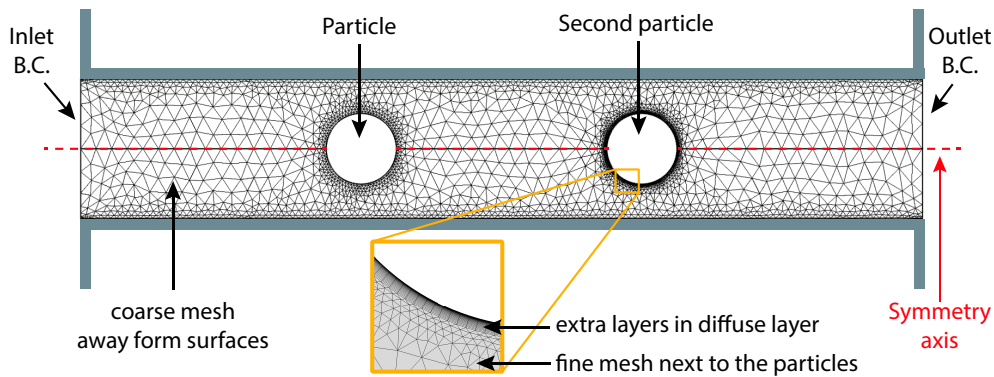


Figure 3.14: Illustration of mesh for a typical simulation geometry. It is a 2D axis symmetric simulation with two particles inside a channel. The complex geometry is divided into triangular elements that are collectively called a mesh. Inside them, the physical equations are linearised and solved iteratively. Higher element density results in more accurate simulation results, while decreasing the element density reduces computation time. The illustration shows an adaptive mesh where the density is high next to the particles because the electric field and flow field vary in that region.

The automated mesh generator often produces unsatisfactory results, forcing us to increase the mesh density on the particle walls. The higher mesh density improves the accuracy, but takes longer to compute. Therefore, we only increase the mesh density in regions where we expect the solution to vary. For example, to model the diffuse layers we had to add tiny boundary layers next to the walls. Figure 3.14 shows a typical mesh with these two characteristics.

The quality of numerical solutions is tested using three methods. First, the residuals of a solver are checked to be much smaller than the required accuracy [78]. This is done automatically by the COMSOL software. Secondly, the mesh quality is verified by running two simulations: one with guessed mesh density, and another with twice the density of elements. If both produce the same results, the guessed density is sufficient. Finally, the numerical solutions are compared to known analytical solutions.

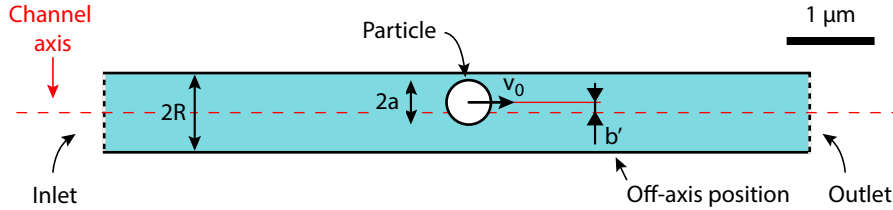


Figure 3.15: Simulation geometry: a single spherical particle is placed in the middle of a cylindrical channel. The tangential position of the sphere is characterised with the parameter b .

To model the hydrodynamic particle-channel interactions, we need to estimate the hydrodynamic friction coefficients. They are directly related to the diffusion coefficients via the Einstein-Smoluchowski relation, see Equation (2.4). Consider the geometry shown in Figure 3.15, where $2R$ is the diameter of the channel, L is the length, $2a$ is the diameter of the spherical particle, and b' is an off-axis position of the particle. If $b = 0$, the problem is rotationally symmetric and a 2D simulation can be used, but otherwise a 3D simulation is needed. The boundary conditions on the particle are set to a moving wall ($\mathbf{u} = \hat{x}v_0$), which corresponds to a particle moving at velocity v_0 . Note that the geometry is stationary, while the boundary conditions represent the motion. The boundary conditions on the inlet and the outlet depend on the channel length. For an infinitely long channel, there is no flux across the inlets ($\mathbf{v} = 0$). This limits the extent of the flow field, allowing us to simulate an infinite channel with $L \sim 8R$. On the other hand, for short channels we use periodic boundary conditions, because they capture the flows across the inlets. This approach will be explained in detail later.

The hydrodynamic friction coefficient is estimated via $\zeta_x = F_{drag,x}/v_0$, where $F_{drag,x}$ is the drag force on the particle in the \hat{x} direction. It is computed by taking a surface integral of the total stress tensor in \hat{x} , where the total stress tensor is a combination of the viscous stress tensor and the hydrostatic pressure [38]. The final result is often reported as the diffusion coefficient for an easy comparison with our experimental results.

3.3.1 Diffusion coefficients in infinite channels

Consider infinitely long channels that have a translational symmetry. There is no flux across their boundaries, since a moving particle cannot displace an infinite column of water. This

problem has been studied extensively in literature [39, 40, 79], allowing us to validate our simulations with analytical solutions. Our second intention is to understand the variation of diffusion coefficient with the confinement ratio, a/R .

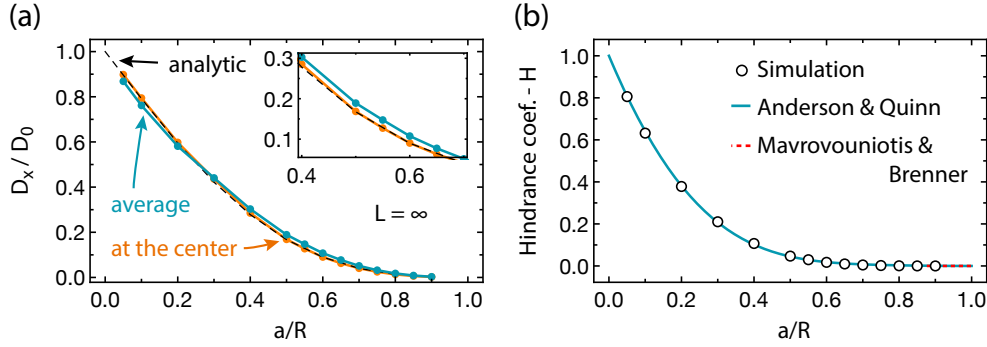


Figure 3.16: Simulation of diffusion coefficient in an infinite channel. (a) Diffusion coefficient as a function of a/R . The orange line shows the coefficient value for a particle placed on the centerline of the channel, while the blue line shows an averaged coefficient over all radial positions, b' . The black dashed line is an analytic solution by Haberman [39] and it agrees well with the simulation for a particle on the axis. The inset shows a closer look at the relevant particle size range. (b) Hindrance coefficient as a function of a/R . Lines show literature values [40], which are in good agreement with the simulation data.

Figure 3.16a shows simulated diffusion coefficients versus the a/R . Notice that values were normalised with the diffusion coefficient in bulk, $D_0 = k_B T / 6\pi\eta a$. The figure suggests that the diffusion coefficient decreases with confinement ratio. The orange line corresponds to a particle kept on the centerline of the channel. It agrees well with the corresponding analytical solution, shown as the black dashed line. Meanwhile, the blue line shows a simulation where D_x is averaged over all the possible positions in the radial direction. This gives a more realistic value for the diffusion coefficients, because particles explore the entire cross-section of the channel in the experiments. It is interesting to observe that curves cross at $a/R = 0.28$: for small particles the average diffusivity is lower than at the centerline. Meanwhile, for large particles the average diffusivity is higher than at the centerline. We will explain the reason for this behaviour in Section 3.4.

The averaged diffusion coefficient can be alternatively expressed as hindrance coefficient [40]:

$$H = 2 \int_0^{1-a/R} K_1^{-1} e^{-E(\beta)/k_B T} \beta d\beta \quad (3.1)$$

where $K_1 = \zeta/\zeta_0$ is normalised friction coefficient, $\beta = b/R$, and $E(\beta)$ is the potential energy. The integral averages over all the positions, b , with weights taken from Boltzmann distribution $e^{-E(\beta)/k_B T}$. In our channels, the double layers are small compared to the channel width, $\lambda_D/2R \approx 0.5\%$. Therefore, the particle experiences almost no electric potential, leading to the approximation $E(\beta) \approx 0$. Figure 3.16b shows our simulation results for the hindrance coefficients alongside the analytical solutions. Again, the simulation agrees well with the literature values. Throughout this thesis, we will use the diffusion coefficients instead of the hindrance coefficients, because this allows a straightforward comparison with the experiments.

3.4 Simulation of spacially varying D_x

The position of particles in a channel has two components: an axial position and a radial position. In our notation, the axial position corresponds to the \hat{x} axis and the radial position corresponds to the $\hat{y}\hat{z}$ plane. The diffusion coefficient does not depend on the axial position [39, 40], which we confirmed by measuring the localised diffusion coefficients, see Figure 3.12. Meanwhile, we normally approximate the radial position with a particle at the centerline of the channel. Here, we drop this approximation and investigate how the radial position affects the diffusion coefficients.

In these simulations, the particle is placed at a distance b' from the cylindrical channel's centerline, as shown in Figure 3.15. The particle touches the channel wall when $b' = R - a$. For simplicity, we use a scaled position parameter that we define as $b/R \equiv b'/(R - a)$, which varies in the range $b/R \in [0, 1]$. The inlet boundary conditions were set to no-flux corresponding to the infinite channel model, allowing us to compare our results with the literature.

Figure 3.17 shows the hydrodynamic friction coefficients for two particle sizes³. For small particles (or large channels), the friction increases as the particle approaches the channel walls, because the viscous shear increases closer to the wall. This is similar to a particle approaching a flat surface [80]. We validate our simulations using approximate analytical solutions shown as dashed lines [39, p. 318]. For large particles ($a \sim R$), the friction coefficient decreases when the particle moves away from the centerline. In this specific case, it is 23% smaller at the position $b/R = 0.85$. Beyond this point, the friction rapidly grows when approaching the wall. This result is counter-intuitive, because Faxen's law suggests that the friction should increase when the particle is approaching the wall.

This phenomenon has been observed before in asymptotic expansions, shown in Figure 3.17a, and also in hydrodynamic simulations [79]. We further investigate this behaviour and

³We use the hydrodynamic friction coefficient representation, since it is more intuitive when talking about drag.

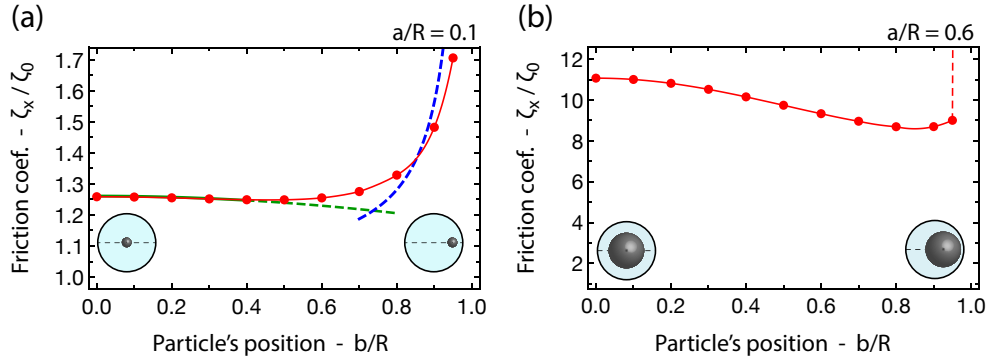


Figure 3.17: Simulation of friction coefficient as a function of particles position. (a) Large channel with a small particle ($a/R = 0.1$). The red circles indicate our simulation results, while the lines were interpolated. The green and blue lines show an approximate asymptotic expansion solutions for limits $b/R \approx 0.0$ and $b/R \approx 1.0$. For clarity, their magnitude was adjusted to coincide with the analytical solution for $b/R = 0.0$, see [39, p. 318]. (b) Case where the diameter of the particle is comparable to the channel ($a/R = 0.6$). The red circles indicate our simulation results, while the lines were interpolated. The insets illustrate the positions of the particle for different values of b/R .

its cause. Figure 3.18 shows the friction coefficient as a function of position and confinement. In the upper region, corresponding to large particles, the friction is smaller close to the wall. Meanwhile, in the lower region, corresponding to small particles, the friction is smaller in the middle of the channel. The transition between these behaviours happens around $a/R \approx 0.3$. It explains a crossover that was observed in Figure 3.16a, when comparing the centerline approximation with the averaged diffusion coefficients.

We now try to give an intuitive explanation for this effect of decreased friction near the wall. Consider a wide particle at the centerline of a channel, where the hydrodynamic drag is radially symmetric. We move it closer to the wall and inspect the drag distribution in the COMSOL simulation. The surface area facing the wall has an increased drag, as expected by the Faxen's Law. However, on the other side of the particle, the drag decreases since there is more liquid between the particle and the channel walls. The decrease happens over much larger area than the increase in drag, thereby resulting in a net reduction of the drag. This explains why for large particles, the friction coefficient decreases when they are close to the walls. In contrast, small particles do not experience this decreased drag on the other side.

3.4.1 Complex cross-section shapes

In our experiments, the channels are not cylindrical, but rather an approximations to a cylinder. Here, we investigate the impact of complex cross-section shapes found in experimental channels.

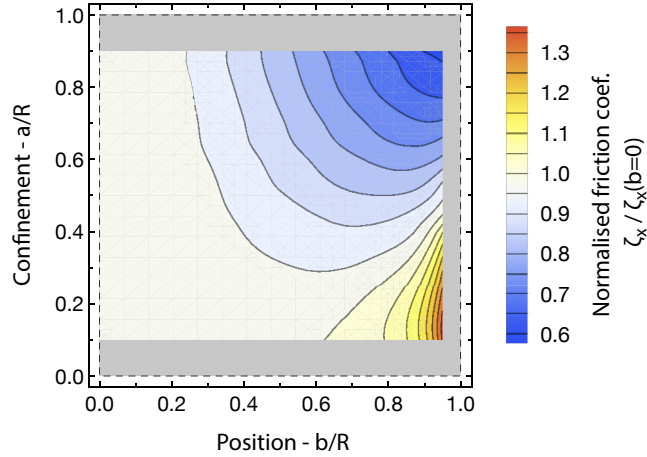


Figure 3.18: Contour plot of friction coefficients as a function of the position (b/R) and the confinement ratio (a/R). The friction coefficients were normalised with the value at the centerline ($b/R = 0$) to remove the variation due to confinement – see Figure 3.16. The grey area was not included in our simulations. The simulation suggests there is a transition with an increasing confinement ratio. For small confinements, the particle moves fastest in the middle of the channel, while above $a/R \approx 0.3$ the particle moves faster if it is close to the walls.

Specifically we compare simulation results for a cylindrical channel, a semi-elliptical channel, and a square channel. The channel dimensions were chosen to closely match the experimental channels: S2–5 μm –2 and B4–13 μm –5.

Figure 3.19a shows diffusion coefficient as a function of \hat{y} and \hat{z} coordinates, i.e. $D_x(y, z)$, for the cylindrical channel. This figure is an alternative representation of Figure 3.17b. Notice that the particle is more diffusive when it is closer to the channel walls. Figure 3.19c shows $D_x(y, z)$ for the semi-elliptical cross-section, where we see a similar diffusivity pattern. The particle is less diffusive in the middle of the channel and more diffusive when it is closer to the walls. In addition, there are diffusion maximums that are close to the two corners and the narrow end. Figure 3.19e shows $D_x(y, z)$ for the square cross-section. All the same features hold, while most diffusive points are in the four corners. Importantly, in all the cases, the diffusion coefficient varies by less than 23% and the particle is always less diffusive in the middle of the channel.

In the experiments, we only track particles in the $\hat{x}\hat{y}$ plane. To model this, we assume that particles explore the entire cross-section with equal probability, suggesting that the projection onto $\hat{x}\hat{y}$ is an average along \hat{z} . The right column in Figure 3.19 shows the averaged values along \hat{z} for the (b) circular channel, (d) semi-elliptical channel, and (e) square channel. In all the cases, variation of diffusion coefficients is less pronounced than in full cross-section simulations. For circular and square channels the variation decreased from 23% to 7%.

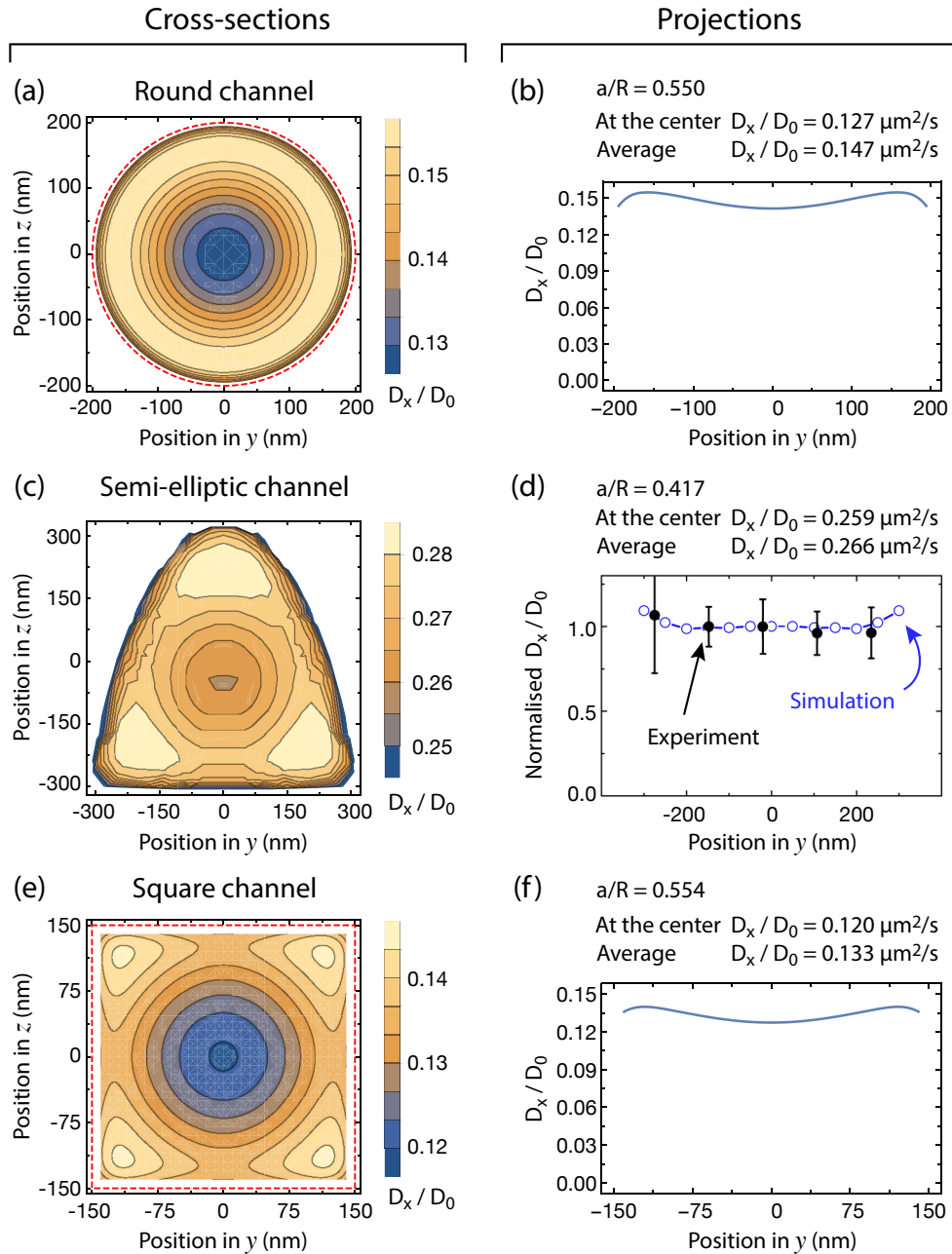


Figure 3.19: Simulation of diffusion coefficients, $D_x(y, z)$, for channels with (a,b) round, (c,d) semi-elliptic, and (e,f) square cross-sections. The left column shows contour plots, while the right one shows projections onto the \hat{y} axis. The three channels have dimensions: (a) $2R = 910\text{nm}$, (b) $W = 1200\text{nm}$, and $H = 1200\text{nm}$, (c) $W = 800\text{nm}$, and $H = 800\text{nm}$, while the particle has a width of $2a = 500\text{nm}$. For the semi-elliptic channel, black circles in (d) show experimental measurements [73].

We compare these simulation results with the experimental results that were presented in Figure 3.2.1a. The experimental data was averaged along the \hat{x} axis within the channel. Figure 3.19d shows the experimental data overlaid with the simulation results, where the values are normalised to account for discrepancy in absolute values [73]. Both are almost constant with \hat{y} position, which explains why the experimental data showed almost no variation in $D_x(y)$.

Particle rotation

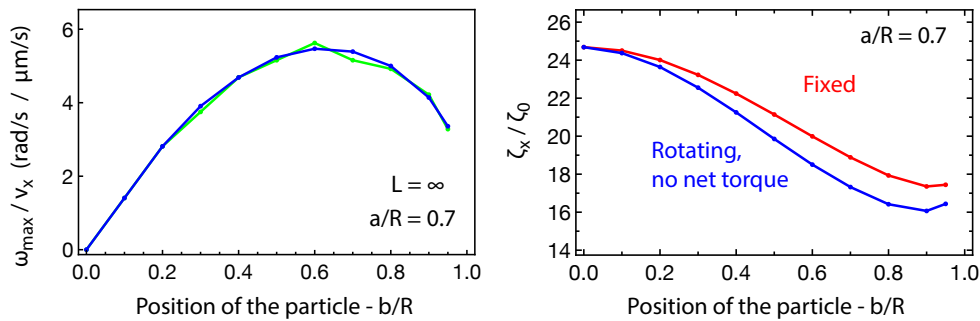


Figure 3.20: Simulation of a rotating particle that is moving along the channel with velocity v_0 . The angular velocity was found such that the torque on the particle is zero. (a) Angular velocity of the particle as a function of position. The rotation is linearly proportional to v_0 , as illustrated by the overlapping curves: blue line for $v_x = 10 \mu\text{m/s}$ and green for $v_x = 1000 \mu\text{m/s}$. (b) Hydrodynamic friction coefficient as a function of position for rotating and fixed particles. The rotation reduced the friction closer to the walls, resulting in increased diffusivity.

We have mentioned earlier that particles have an unevenly distributed drag on their surface. The resulting torque should induce a rotation, which was not included in the previous simulations. Therefore, we probe a limit when the particle is rotating with a maximum angular velocity ω_{\max} , at which the torque is zero. We find this limit by running a gradient climbing script on MATLAB. It runs a COMSOL simulation with a guessed angular velocity applied on the particles boundary, then measured the torque and adjusted its guess for the next simulation. The script stops when it finds zero torque, and thus, the maximum angular velocity.

Figure 3.20a shows the angular velocities computed using this method. Angular velocity is linearly proportional to the particle's velocity v_0 , as expected. Figure 3.20b suggests that rotation reduces the hydrodynamic friction coefficient. The average difference between fixed particle model and rotating particle model is on average 5%. This simulation gives an upper limit for our accuracy, because it is not clear how much rotation there is in real systems.

With finite channel model

It will be shown in Section 3.5 that channels of finite length should be modelled with periodic boundary conditions set on the inlets. Here, we investigate how radial position influences that model. Figure 3.21a shows the diffusion coefficients as a function of radial position. The different levels are due to decreased pressure resistance as described earlier. Importantly, the variation is smaller in the finite channel, where the particle still diffuses faster closer to the boundary. The difference between maximum and minimum diffusivity is smaller at 6.0%, while after projection onto $\hat{x}\hat{y}$ the difference is only 1.9%. This suggests that the diffusion coefficients are almost always uniform in \hat{y} direction for narrow channels.

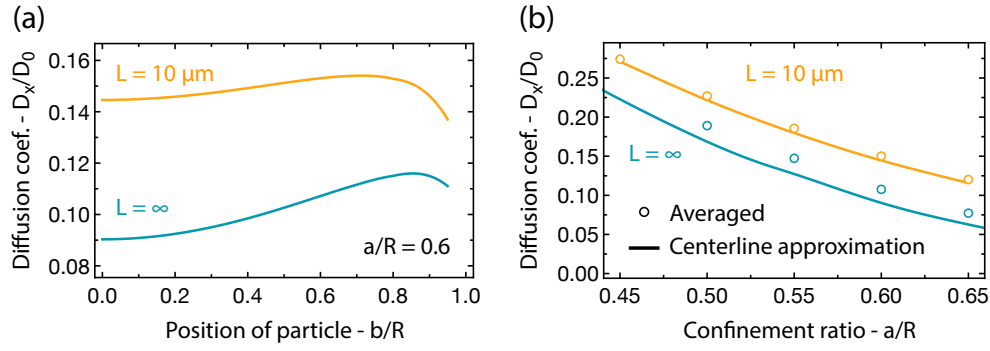


Figure 3.21: Simulation of varying position of A $2a = 500\text{nm}$ particle inside a cylindrical channel of length $L = 10\mu\text{m}$. Finite channel was simulated with periodic boundary conditions on the inlets of the channel and results are shown in orange. For comparison the teal curves show results for the infinitely long channel. (a) Diffusion coefficient as a function of position of the particle. (b) Diffusion coefficient as a function of confinement ratio. The circles correspond to averaged values across all possible positions, while lines correspond to values on the centerline of the channel. The difference between averaged and centerlines values is much smaller in the short channel.

3.4.2 Approximations in all simulations

Throughout this thesis we use two approximations: (1) the centerline approximation, where the hydrodynamic properties are estimated while keeping the particle at the centerline of the channel. (2) Effective radius approximation, where the channel is treated as cylindrical with a matching cross-section area. These approximations reduce the complexity and allow for quick computations. For example, the position dependant simulations require from 10 to 40 simulations in 3D, while the approximations reduce it to a single simulation in 2D. Here, we will discuss the impact of these approximations on the diffusion coefficient estimates.

For the centerline approximation, Figure 3.21b shows a comparison between centerline and the averaged diffusion coefficient. The figure suggests that the centerline approximation underestimates the diffusion coefficients by about -11% in the range $a/R \in [0.4, 0.6]$ for infinite channels. For short channels the difference is smaller, at -2.6% in the range $a/R \in [0.45, 0.6]$. Therefore, simulations with these approximations slightly underestimate the diffusion coefficients.

For the effective radius approximation, Figure 3.19 shows three different cross-sections and their respective diffusivity. The semi-elliptical channel has an effective confinement of $a/R = 0.417$ and an average diffusion coefficient of $D_x/D_0 = 0.266$. From Figure 3.16a, the cylindrical channel with same a/R has average coefficient of $D_x/D_0 = 0.281$, which is 5.6% higher. The same estimate for the channel with square cross-section gives 10.8% higher results. Thus we are overestimating the diffusion coefficient with the effective radius approximation.

The two approximations roughly cancel each other. The combined error should be within 10% , where the exact number depends on the geometry. For the experimentally relevant confinement ratios, the biggest correction is at $a/R = 0.65$, where the diffusion coefficient is 6% higher; while at $a/R = 0.4$, the correction is only 1% . Furthermore, for finite channels the corrections are even smaller since the position dependence is weaker. We expect our other simulations to have a similar accuracy.

3.5 Increased diffusivity in finite channels

Here, we examine the diffusion coefficients inside finite channels. The label ‘finite’ is used to differentiate from infinite channels. We argue that the finite channels are fundamentally different, because they permit flows across the inlets. In such case, a moving particle acts like a piston, thus inducing a Poiseuille flow inside the channel. Assuming that most resistance to such flow comes from the narrow channel itself, we can model this with periodic boundary conditions set on the inlets of the channel.

To the best of our knowledge, this is an unprecedented approach to modelling finite channels, where we will provide strong experimental evidence for this boundary condition in Chapter 4. In this section, we explore the consequences of the periodic boundary conditions for the diffusion coefficients.

Figure 3.22 shows simulated diffusion coefficients for channels with periodic boundary conditions. The diffusivity is higher than in the infinite channel case and depends on the length of the channel. The two models converge in the limit $L \rightarrow \infty$, as expected.

The difference between the two model predictions becomes obvious when comparing the flow profiles induced by the moving particle. Figure 3.23a shows the flow profile inside the

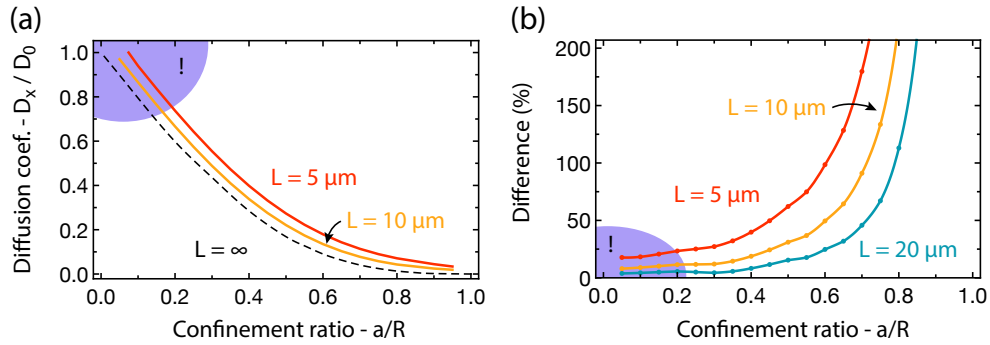


Figure 3.22: Simulation of finite channels with periodic boundary conditions on the inlets. (a) Diffusion coefficients as a function of confinement ratio. The particle size was kept fixed at $2a = 500 \text{ nm}$. (b) Difference between the finite channel predictions and the infinitely long channel predictions. The diffusion coefficients are higher in shorter channels. The purple regions highlight artefacts due to the periodic boundary conditions.

infinite channel. The induced flow circulates around the particle, extending about $2R$ distance into the channel. This agrees with the literature [39, 40, 44, 81].

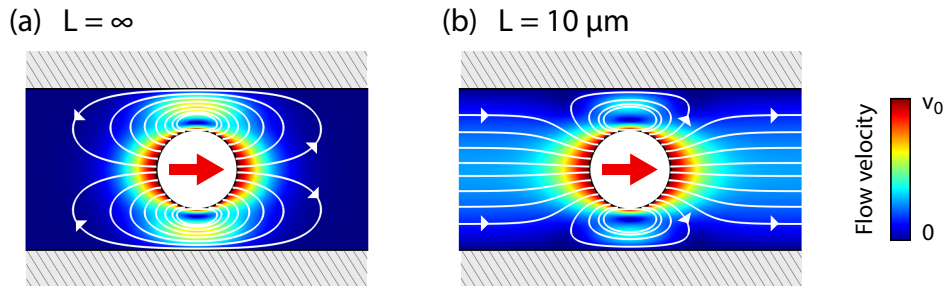


Figure 3.23: Flow profile around the particle for (a) an infinite channel and (b) a finite channel. In both simulations the particles had diameter of $2a = 500 \text{ nm}$ and the channels had diameter of $2R = 1000 \text{ nm}$. For clarity, the plots show only short segments of the channels. In both cases, the particles are moving to the right with velocity v_0 , which creates a pressure difference across the particle. (a) In the infinite channel, the endless liquid column resists motion, thus forcing all the liquid to circulate around the particle. The flow does not extend far into the channel. (b) In the finite channel, the pressure induces a circulating flow around the particle, and also a Poiseuille flow along the channel, which escapes through the inlets. This reduces the hydrodynamic friction and thus increases the particle's diffusion coefficient.

In the finite channel, the flow is fundamentally different, as shown in Figure 3.23b. Here, we see two modes of flow. The first is the circulation around the particle that is weaker than in the infinite channel. The second mode is the Poiseuille flow, which is induced by the piston like motion of the particle. The periodic boundary conditions facilitate this mode. Physically this corresponds to flow into and from the reservoirs, where its origin is discussed in

Chapter 4. Importantly, the second mode reduces the hydrodynamic drag force on the particle, and therefore, increases the diffusivity.

3.5.1 Access resistance

Our model has a flaw at low confinement ratios: it does not recover the bulk diffusion coefficient in the limit $a/R \rightarrow 0$, as indicated by the purple areas in Figure 3.22. We overestimate the diffusion coefficients, because the flows outside the channel have been assumed to be negligible. This condition is satisfied in long and narrow channels, where almost all the pressure drops inside the channel. However, for wider channels, the pressure drop outside the channel is significant. Here, we will develop a correction to account for the pressure drop outside the channel.

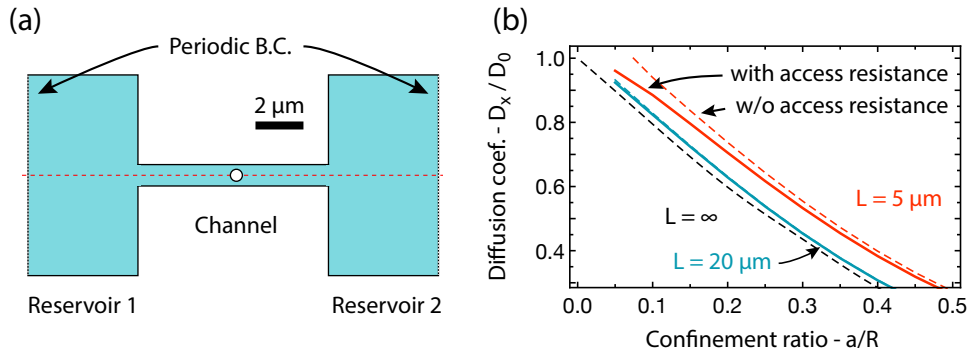


Figure 3.24: Impact of access resistance. (a) Modified simulation geometry that includes two reservoirs at either end. The periodic boundary condition was moved to the end of the reservoir. It had width and length of $40 \mu\text{m}$ and $20 \mu\text{m}$, respectively. (b) Diffusion coefficients as a function of confinement. The dashed lines show previously estimated values with periodic boundary conditions on the channel inlets. Meanwhile, the solid lines correspond to the modified geometry shown in (a), which takes into account the access pressure resistance. The access resistance changes the diffusion coefficient for the short channel, but has less impact on the longer channel.

In our first attempt, we add two reservoirs at either end of the channel, as shown in Figure 3.24a. The size of the reservoirs did not affect the solution as long as it was ~ 5 times wider than the channel. This suggests that pressure drop occurs in the access area next to the inlets. Figure 3.24b shows the resulting diffusion coefficients, where they converge to the bulk value in the limit $a/R \rightarrow 0$. The coefficients are also slightly smaller than predicted before, where the correction is significant for short channels and less important for longer channels.

Including reservoirs in the simulation increases the computation time and complexity of the model, both of which are undesirable. Therefore, we incorporate the effects of reservoirs into the boundary conditions on the inlets. Here, we explain how to achieve this in COMSOL.

Within our model, everything is linearly proportional to the velocity of the particle, v_0 . For this reason, we use *pressure resistance* defined as $G = \Delta p/Q$, where $Q = \langle u_x \rangle \pi R^2 \propto v_0$ is the flow rate. Sampson has solved pressure resistance through a circular aperture in 1891 [39, p. 153]:

$$\Delta p = \frac{3\eta}{R^3} Q \quad (3.2)$$

It accounts for the pressure drop in the area outside the inlets that we call access resistance. In our model, it is added to the periodic boundary conditions as a pressure drop. In COMSOL's periodic boundary module, we add a pressure difference of $-3*\mu*Q/R^3$. Then we define a variable under 'definitions': $Q = \text{inlet_integral}(2*\pi*r*w)$, where the 'inlet_integral' is defined as a surface integral over one of the inlets. This procedure allows us to incorporate the pressure resistance into the COMSOL simulation.

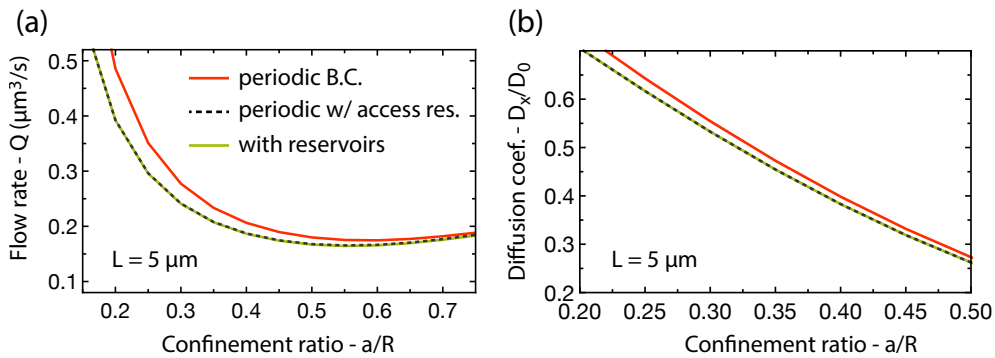


Figure 3.25: Assessment of periodic B.C. with added access resistance via Equation (3.2). In the simulation, a single particle of diameter $2a = 500 \text{ nm}$ was moving at a velocity of $v_0 = 1 \text{ } \mu\text{m/s}$, while the channel geometry had three variations: periodic B.C.; periodic B.C. with access resistance via Equation (3.2); and simulation with reservoirs as shown in Figure 3.24a. (a) Flow rate as a function of confinement ratio. (b) Diffusion coefficient as a function of confinement ratio. The simulation reservoirs and periodic B.C. with access resistance agree very well, suggesting that Equation (3.2) can be used to account for access resistance.

Figures 3.25 compares the two different methods for including access resistance. It suggests that adding Equation (3.2) is equivalent to including the reservoirs as shown in Figure 3.24a. Including the access resistance through Equation (3.2) is computationally fast, and does not risk destabilising the meshing process of the simulation. Therefore, we will use this modified boundary condition in most our simulations.

3.5.2 Comparison with experimental data

Figure 3.26 compares our model predictions for the diffusion coefficients with the experimental data. The black dashed line corresponds to the infinite channel model, which is below all the measured values, suggesting that the infinite channel model can not accurately describe finite channels. This discrepancy has been observed before [73, 74, 82].

Instead, the red points are distributed around the red line that corresponds to finite channel simulation with $L = 5 \mu\text{m}$. Other points are also color coded according to their length. In each case, our simulations for finite channels agree very well with the experimental data.

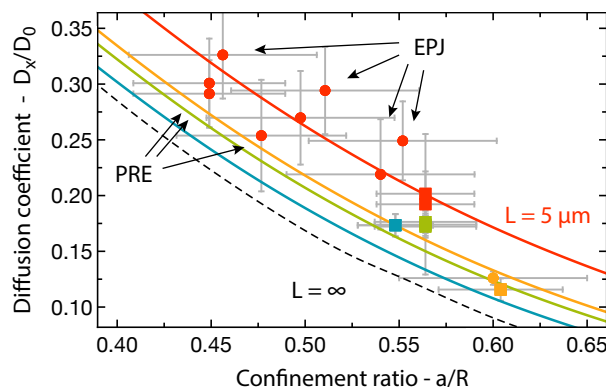


Figure 3.26: Diffusion coefficient comparison between simulation and experiments. Lines correspond to simulations with different channel lengths. From top to bottom: $L = 5 \mu\text{m}$; $L = 10 \mu\text{m}$; $L = 13 \mu\text{m}$; $L = 25 \mu\text{m}$; $L = \infty$. Points correspond to experimental measurements where the color indicates the channel length as before, and the shape indicates the cross-section shape: square for square and round for semi-ellipse. “PRE” arrows show data taken from [73], while “EPJ” are taken from [74]. Other values were reported in the Table 3.4. The measured diffusion coefficients are higher than predicted by the infinite channel model. Meanwhile, our model agrees with measurements within the error bars.

Overall, our finite channel model with the periodic boundary conditions predicts the diffusion coefficients better than the infinite channel model. This suggests that our model captures the physics happening inside channels. Furthermore, Chapter 4 will provide stronger evidence for the validity of our model.

3.6 Conclusion and impact

We have demonstrated that microfluidic lab-on-a-chip devices can be used to study Brownian motion inside narrow channels. In addition, we presented a method for estimating diffusion coefficients inside channel by solving Stokes equations using COMSOL. Importantly, our synthetic channels have a uniform cross-section and well-defined dimensions, allowing us to

compare the experimental data directly with the simulation results. This high degree of control leads to new insights about the physics inside channels. We will use the same methods to study particle-particle interactions in the following chapters.

In this chapter, we have shown that the measured diffusion coefficients are significantly higher than previously thought [40]. We resolved this discrepancy by introducing a new model for hydrodynamic particle-channel interactions, which has periodic boundary conditions set on the inlets of the channels. This model successfully reproduces the experimental data without any fitting parameters, as shown in Figure 3.26. Importantly, our model suggests that diffusion coefficients depend on the length and the diameter of the channel. In contrast, previous models only considered the diameter. These results have far-reaching implications for transport phenomena, since the diffusion coefficients come as a parameter in most transport models [40, 83].

Chapter 4

Hydrodynamic Particle Interactions

In this chapter, we study particle-particle interactions, which are important for understanding collective behaviour. We are mainly interested in narrow channels where $a/R \gtrsim 0.3$, since large channels resemble bulk, where interactions are well understood [42, 84, 85]. Some of our findings are reported in [86].

In narrow channels, the hydrodynamic interactions were previously measured to decay rapidly with particle separation [22, 24, 25]. Indeed, the steady flow induced by particle motion decays exponentially with $r/2R$, where $2R$ is the channel width [39, 40, 44, 81]. Consequently, the particle-particle interaction strength is also expected to decay exponentially with their separation [22, 44]. However, the previous experiments used microfluidic chips with a groove geometry to mimic channels, where sedimentation kept the particles in the groove, but the liquid could escape. Therefore, these experiments did not capture far field hydrodynamics of channels [17, 22, 24, 25]. The lack of controlled experiments in a 1D confinement leaves many unanswered questions about the magnitude and spacial extent of hydrodynamic interactions inside narrow channels [17, 87].

In this chapter, we present the first measurement of the interactions between two Brownian particles inside a finite narrow channel, in which both the particles and the liquid are confined. Figure 4.1 illustrates our experiments. The ‘closed’ channel, shown on the left, has only one end connected to a bulk reservoir, while the ‘open’ channel, shown on the right, has both ends connected. Here we demonstrate a fundamental difference between diffusion in open and in closed channels [22, 39, 44].

4.1 Method for placing particles in channels

Our microfluidic channels are produced using the method described in Section 3.1. Crucially, the PDMS chips are oxygen plasma bonded onto a glass slide which provides a bottom wall

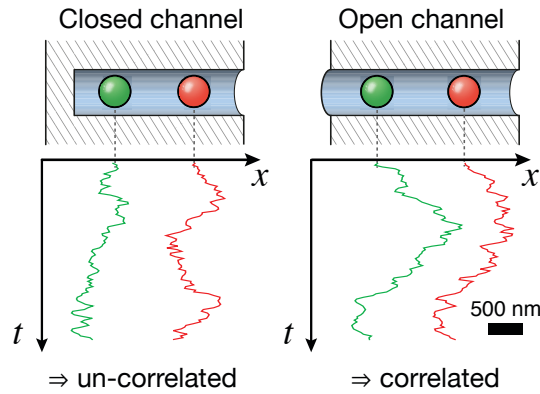


Figure 4.1: Trajectories of two particles undergoing Brownian motion in closed and open channels. The trajectories are visibly un-correlated in the closed channel, suggesting the particles move independently. In the open channel the trajectories resemble each other, which leads to strong motion correlation.

confinement for the channels. This constrains the liquid to the channel, and thus, offers the first experimental insights into the full hydrodynamic interactions between Brownian particles in narrow channels.

We use low particle concentrations to prevent undesired interactions with particles from outside the channel, and also to minimise particle sticking. At these concentrations, finding two or more particle inside the channel is unlikely. Therefore, we developed two methods for placing particles inside the channel. For the first method, we use a custom-built holographic optical tweezers [15, 88, 89] to position two particles inside the channel, and then turn off the laser trapping, which releases the particles and allows them to diffuse freely. Subsequent motion is recorded using the CMOS camera (DMK-31BF03, Imaging Source) at a rate of 30 frames per second until one particle escapes the channel. See a video demonstration online [90].

The second method uses an external electric field to drive particles into the channel. Once a desired number of particles is inside the channel, the electric field is switched off and the subsequent Brownian motion is recorded using the CCD camera (Mikrotron MC1362). A detailed description of this method is available in Section 5.1. Throughout this chapter, we employ the first method unless indicated otherwise.

In this chapter, we will be performing control measurements using closed channels that have one of the inlets sealed. They were produced by shifting the alignment of the photolithography layer, where the underlying channel no longer spans the entire barrier. Figure 4.2a shows a closed channel, while Figure 4.2b shows a channel with both inlets open.

4.2 Nondecaying interactions

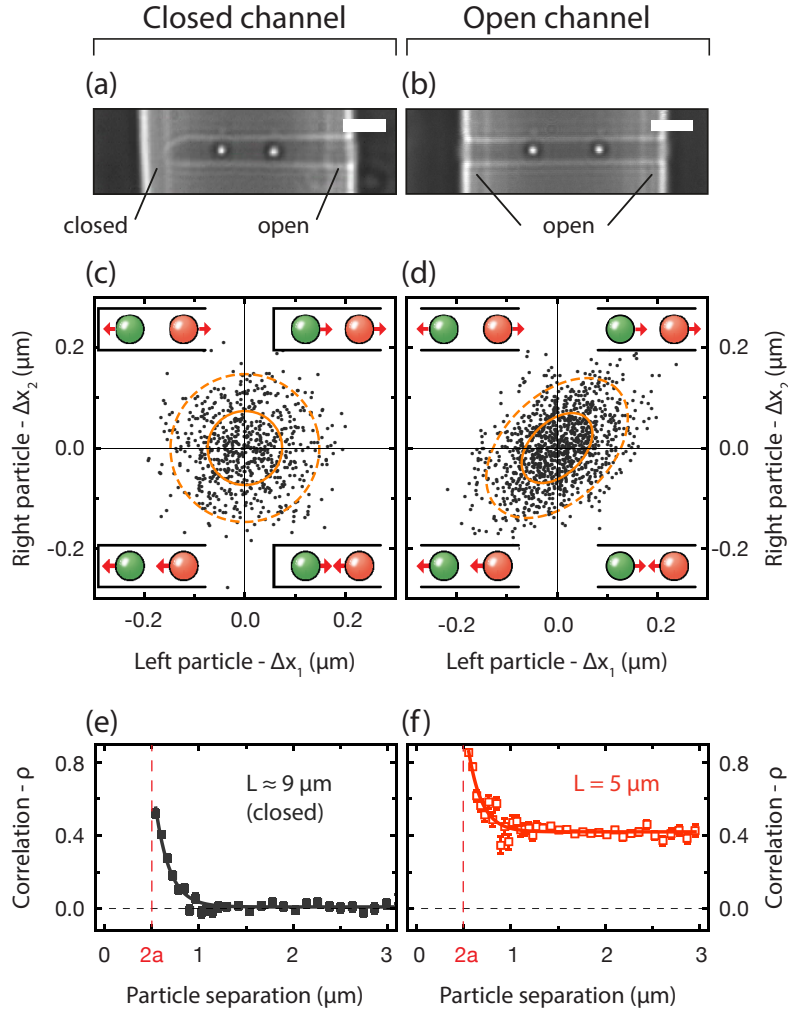


Figure 4.2: Comparison between a closed channel (left column) and an open channel (right column) experiments. The top row (a,b) shows bright-field images of microfluidic channels containing two colloidal particles. Scale bars indicate $2\ \mu\text{m}$. The middle row (c,d) shows displacements of the second particle (\hat{y} axis) as a function of the displacement of the first particle (\hat{x} axis). Each distribution contains 1000 displacement pairs with an initial particle separation of approximately $2.5\ \mu\text{m}$. The overlaid lines indicate contours for σ and 2σ from a 2D normal-distribution fit. Insets illustrate the direction of motion for each quadrant. The bottom row (e,f) shows the correlation coefficients versus the separation between the two particles. The solid lines indicate the fits to the phenomenological model $y = A \exp(-x/B) + C$ where the fitted parameters are: (e) $A = 18 \pm 8$, $B = 0.15 \pm .02\ \mu\text{m}$, $C = 0.005 \pm .004$; (f) $A = 20 \pm 9$, $B = 0.14 \pm .02\ \mu\text{m}$, $C = 0.419 \pm .005$. The two-particle motion is strongly correlated in the open channel, suggesting a presence of long-range non-decaying interaction.

We start with the case of two particles. For data analysis, particle trajectories are divided into displacement steps between consecutive frames: Δx_1 and Δx_2 denote the displacements of the first particle (one on the left) and the second particle (one on the right), respectively. The two-particle interaction strength is expected to be a function of their separation, and therefore, we group the pairs of displacements according to the distance between the centres of the particles.

For the closed channel, Figure 4.2c shows the displacements of the second particle (Δx_2) as a function of displacement of the first particle (Δx_1). The distribution is circular with points distributed equally in each quadrant, suggesting the two particles move independently from each other. This is expected for a large particle separation of $10a$ [22, 44]. In contrast, the distribution for the open channel, shown in Figure 4.2d, is elliptical with the major axis along $y = x$ and ellipticity of 0.75. This implies that the two particles moved in the same direction more frequently than in opposite directions, suggesting the presence of long-range interaction between the particles.

We quantified the interaction strength using the Pearson product-moment correlation coefficient defined as [91]: $\rho = \text{cov}(\Delta x_1, \Delta x_2) / \sigma(\Delta x_1) \sigma(\Delta x_2)$, where cov is the covariance, and σ is the standard deviation. The value $\rho = 0$ indicates independent particle motion and $\rho = 1$ corresponds to fully correlated motion.

Figures 4.2e and 4.2f show the correlation coefficients as a function of particle separation. Evidently, the correlation is stronger and has a longer range in the open channel. A detailed examination of the closed channel results shows a high correlation when particles are close to one another that exponentially decays to zero in a separation of $\sim 4a$. We fitted a phenomenological model, $y = A \exp(-x/B) + C$, that captures the decay rate and has an additional offset parameter. The fit yielded $B = 0.15 \pm .02 \mu\text{m}$, $C = 0.005 \pm .004$, where we introduced the offset to characterise the novel behaviour observed in the open channel. As evident from the data, the correlation coefficient exhibits the same initial exponential decay, but in stark contrast, it asymptotes to a constant offset. This finite correlation coefficient is captured by the fit to the phenomenological model, yielding $B = 0.14 \pm .02 \mu\text{m}$, $C = 0.419 \pm .005$. This constant, nondecaying component was not expected. Furthermore, the correlation persists even at the largest measured distances, suggesting that the two particles always interact, as long as they are both inside the open channel. To the best of our knowledge, this is the first observation of such distance-independent interactions between Brownian particles.

We further investigated the effect of the channel length on the particle-particle interaction strength. Figure 4.3 shows the correlation coefficients for open channels of lengths $L = 5, 10$ and $17 \mu\text{m}$. The data clearly indicates that the interaction strength decreases with L . In the longest channel, shown as circles, we observed particles interacting at separations of more than

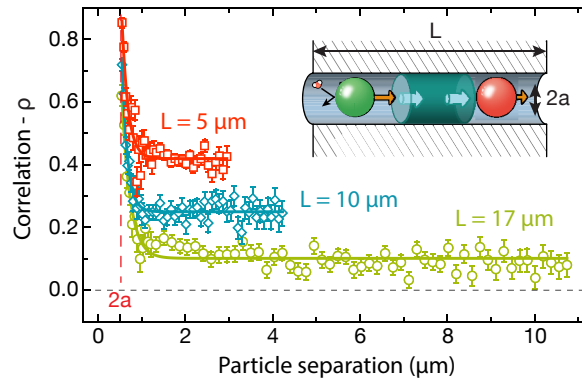


Figure 4.3: Correlation coefficients for two interacting particles for different channel lengths. The three curves correspond to open channels with different lengths, from top to bottom: $5 \mu\text{m}$, $10 \mu\text{m}$, $17 \mu\text{m}$. The solid lines show the fit to a model $y = A \exp(-x/B) + C$, where the offset coefficients were (from top to bottom): $C = 0.420 \pm .006$; $0.250 \pm .005$; $0.101 \pm .004$. Evidently, the long-range two-particle correlation coefficient decreases with the channel length. Inset illustrates the proposed model for long-range hydrodynamic interaction.

$40a$. This is the largest relative distance measured between interacting Brownian particles, even exceeding the $\sim 20a$ separation measured in bulk [42, 84]. This is a surprising result because the geometric confinement typically reduces the maximum interaction distance [22, 39, 84].

4.2.1 Hydrodynamic interaction model

Based on our observations we propose a hypothesis for the distance-independent interaction mechanism, that is schematically illustrated in the inset of Figure 4.3. Suppose the first particle, shown on the left, moves to the right due to a thermal impulse that gives it momentum. At steady state, its motion induces a flow that is constrained by the channel geometry to flow either around the particle or along the channel. Importantly, the latter flow has been previously neglected [22, 39, 40, 44] because the studies considered infinitely long channels, in which the finite pressure exerted by the moving particle cannot displace an infinite liquid column. In contrast, we argue that for finite open channels flows extend throughout the whole channel. Consequently, the induced flow along the channel has a constant mean flow velocity that is proportional to the driving force, i.e. the first particle's velocity [29, 39]. This flow encounters the second particle, shown on the right, and exerts a viscous drag force on it. The magnitude of this force is a function of flow velocity [92] and thus also a function of the first particle's velocity, but is independent of the particle positions. The opposite case of the second particle moving can be inferred by symmetry, and the final interaction is a combination of the two cases. This gives rise to the particle-particle interaction that we observed with our correlation

coefficient measurements and also explains why the value is distance-independent in open channels. In a limit, where the particle size matches the channel, this problem resembles two pistons in a pipe and the trajectories would be perfectly correlated [41]. On the contrary, in the closed channels, the dead end blocks the flow along the channel, thus eliminating the non-decaying hydrodynamic interaction. Therefore, our hypothesis qualitatively explains the long-ranged interactions observed in the open channels.

To quantitatively capture the experimental results, we employ the numerical simulations described in Section 3.3. Here, the geometry has two spherical particles inside a cylindrical channel with periodic boundary conditions on the inlets. We apply an instantaneous velocity on one particle and calculate the resulting drag forces on both particles. This gives the hydrodynamic friction coefficients, which for the two particle system in 1D is a 2×2 symmetric matrix. Its diagonal terms ($\zeta_{1,1}$; $\zeta_{2,2}$) describe hydrodynamic drag experienced by the moving particles (first; second), and the off-diagonal elements ($\zeta_{1,2} = \zeta_{2,1}$) correspond to a force exerted by the moving particle on the other particle. The friction matrix values are computed directly from the numerical simulation. In addition, the friction matrix can be obtained from the experiments using a diffusivity matrix, $\mathbf{D} = k_B T \boldsymbol{\zeta}^{-1}$ [29], with components $D_{i,i} = \langle \Delta x_i^2 \rangle / 2\Delta t$ and $D_{1,2} = D_{2,1} = \langle \Delta x_1 \Delta x_2 \rangle / 2\Delta t$ [93]. This allows us to compare the hydrodynamic interactions predicted by our simulation with the measured data.

Figures 4.4a and 4.4b illustrate the typical flow patterns computed with our simulation. Notice that the flow in the closed channel curls around the particle and does not extend far into the channel. This contrasts with the open channel, where the flow around the particle is weaker and there is a Poiseuille flow along the whole channel length. This moving fluid column exerts a force on the second particle that gives rise to the non-decaying interaction. Figures 4.4c and 4.4d show a quantitative comparison between the numerical simulation and experimental data. The friction with the channel walls is the same for both particles, leading to the overlapping curves $\zeta_{1,1}$ and $\zeta_{2,2}$. Meanwhile, the interaction force, $\zeta_{1,2}$, asymptotes to a non-zero value for the open channel only, which is similar to the correlation coefficient that was reported earlier. At small separations, the discrepancy between simulation and experiment is likely caused by electrostatics and finite tracking resolution. Meanwhile, at large separations, the values compare very well, with the largest discrepancy below 20%. This is a good agreement given the approximations made in our simulations.

4.2.2 Analytical model

Here, we present an analytical model for the particle-particle interaction developed by Eric Lauga and John R. Lister [86]. The model focuses on physical scalings and omits detailed

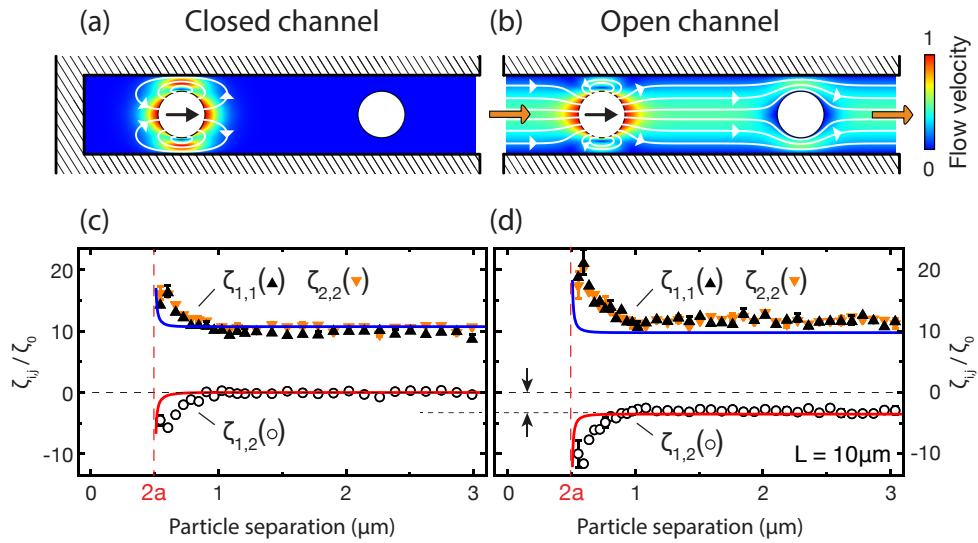


Figure 4.4: Comparison between the experimental data and the simulation results. Top row illustrates flows inside the (a) closed and (b) open channel based on simulation results. The left particle has an instantaneous velocity to the right while the right particle is kept fixed. The proportions were chosen for illustrative purposes. The bottom row compares the friction matrix values as a function of particle separation for the (c) closed and (d) open channel. The points indicate the experimentally measured values, while the solid lines show the corresponding simulation results obtained without any fitting parameters. All values are normalised with the friction coefficient in the bulk: $\zeta_0 = 6\pi\eta a$. Error bars are shown for every fifth data point. Arrows highlight the non-zero interaction term, which agrees well with our simulation results, suggesting that the non-decaying interaction is caused by the induced flow inside the channel.

numerical pre-factors. For the full derivation see Appendix C. Our goal is to estimate the typical mean flow velocity in the channel resulting from the motion of one particle.

Consider a spherical particle of diameter $2a$ located in the centre of an open cylindrical channel of radius R and length L . We assume that the particle moves instantaneously to the right with velocity U . The fluid displaced by the particle must either be pushed along the channel to the right channel end, with more fluid drawn in at the left, or leak from right to left through the thin gap between the particle and the channel wall. The pressure increase across the sphere, Δp , is proportional to the flow rate in the channel, Q , according to Poiseuille law

$$\Delta p \sim \frac{\eta Q L}{R^4}, \quad (4.1)$$

where η is the dynamic viscosity. We neglect any hydrodynamic resistance due to the recirculation from the exit of the channel to the entrance, equivalent to imposing a periodic boundary condition. Mass conservation around the moving sphere (in the frame moving with the sphere) leads to

$$Q - UR^2 \sim Rq, \quad (4.2)$$

where q is the leakage flux through the thin gap between the sphere and the channel. It is approximately given by lubrication theory [38]

$$q \sim -Uh - \frac{\Delta p h^3}{\eta l_0}, \quad (4.3)$$

where $h \equiv R - a$ is the minimum gap width, and $l_0 \sim (ah)^{1/2}$ is the characteristic lubrication length-scale. Combining these equations and taking the limit $h \ll R$, we obtain the flow rate

$$Q \sim UR^2 \left(\frac{R^3 a^{1/2}}{R^3 a^{1/2} + L h^{5/2}} \right). \quad (4.4)$$

Combining with the mean flow in the channel, $\langle u \rangle \sim Q/R^2$, we get the final expression

$$\frac{\langle u \rangle}{U} \sim \frac{R^3 a}{R^3 a + L h^{5/2} a^{1/2}}. \quad (4.5)$$

Our result shows that the mean flow in the channel is non-zero, but a function of the channel dimensions R and L . Importantly, our model reproduces the observed decrease with the channel length - scaling with $1/L$. The long channel limit ($L \rightarrow \infty$) gives no external flows ($Q = 0$) equivalent to the closed channel case.

Quantitatively, our model agrees with the simulations in the limit of $a/R \approx 1$. Below this value, the analytical model deviates away due to the lubrication approximation that was used in

the derivation. Nonetheless, the model proves that the scalings obtained with the numerical simulations are correct.

4.3 Many particle interactions

We have shown that two particles interact by inducing the Poiseuille flow, which affects all the particles inside the channel. Therefore, the interactions are not limited to two particles, but will act on an arbitrary number of particles. Here, we investigate how the number of particles affects the nondecaying hydrodynamic interactions.

Henceforth only the open channels are discussed and we drop the label. Also, the subsequent analysis excludes frames where particles are closer than d_{\min} . This eliminates the close range interactions that comprise electrostatic repulsion, close range hydrodynamics, and the nondecaying interactions. Meanwhile, at large separations only the nondecaying interactions persist. Figure 4.3 suggests that the close range interactions decay to zero at $1 \mu\text{m}$. Thus we set the cut-off distance at $d_{\min} = 1.2 \mu\text{m}$.

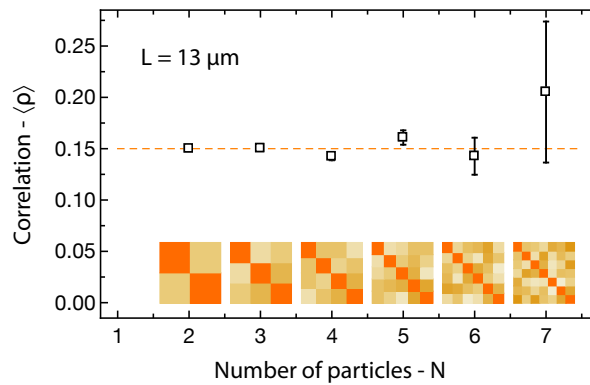


Figure 4.5: Average correlation coefficient as a function of particle number. The experiment was performed in a $L = 13 \mu\text{m}$ long channel (B4-13um-2), where the particles were placed using the electrophoretic method. The insets show a color representation of the correlation matrices, where the red diagonal elements are equal to 1, while white represents 0. Each element of the matrix corresponds to the correlation between two particles. These matrices have no structure, suggesting that all particles are equally correlated with each other. Error bars show an average error for the correlation coefficients in the matrix.

Figure 4.5 presents correlation coefficient for different particle numbers, N . The coefficient is calculated for each pair of the particles and then averaged. Within our measurement accuracy, the correlation coefficient is independent of N , suggesting that the nondecaying hydrodynamic interactions persist even when particle densities are high.

The many-particle correlations can be represented as a correlation matrix, where the matrix elements are correlation coefficients between the pairs of particles. It is a symmetric matrix with a unit diagonal. The insets in Figure 4.5 show the correlation matrices with color coded values. Importantly, notice that there is no obvious structure to the matrices, meaning that any two pairs interact in the same way. This statement is also supported by the observation that the correlation fluctuations are within the statistical variance. This result suggests that all particles interact in the same way, no matter what their relative position is. This further highlights the uniqueness of the nondecaying hydrodynamic interactions, because earlier studies only considered the nearest neighbour interactions, while assuming that others are negligible [22, 94].

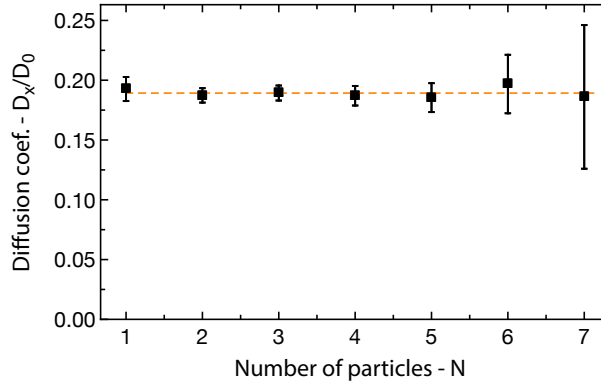


Figure 4.6: Diffusion coefficient as a function of particle number in a channel. Data was estimated from the same trajectories as in Figure 4.5. The D_x was estimated using seven MSD points, where the distance between the particles was greater than $d_{min} = 1.2\mu\text{m}$. The dashed orange indicates the mean value, suggesting that the diffusion coefficient is independent of N .

Additionally, Figure 4.6 shows that the diffusion coefficient is also constant for different N (same experiment). Therefore, the particle number does not affect the diffusivity of individual particles. The error bars increase with N , because we collect less data due to the distance exclusion requirement and a limited imaging time until one particle escapes.

4.3.1 Generalised interaction model

The simulation method presented in Section 4.2.1 and in reference [86] works only for two particles. In that model one particle is moving, while the other particle is fixed. The drag force is estimated on the fixed particle without accounting for an induced motion. However, this approach introduces an unphysical artefact if more than two particles are studied: pressure drops across each fixed particle because they act as obstacles to the flow. In contrast, the

pressure drop is almost negligible for moving particles. In this section, we address this problem and generalise our simulation method.

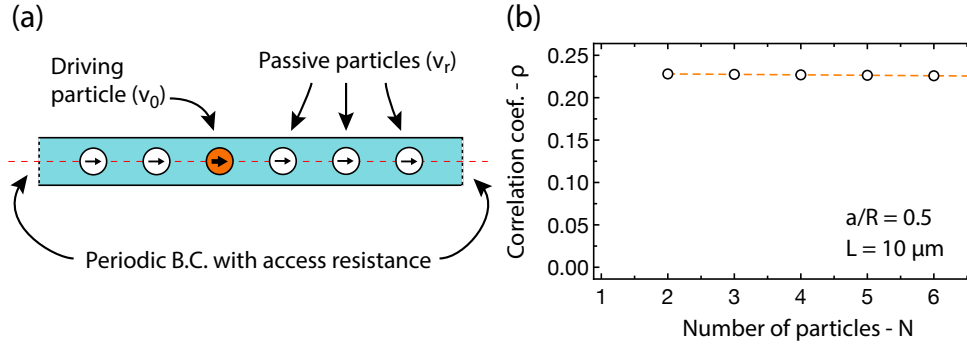


Figure 4.7: (a) Multi particle simulation geometry for the generalised method. Inlets have a periodic boundary condition with access resistance via Equation (3.2). Orange highlights the driving particle, while white particles move in the Poiseuille flow. (b) Simulated correlation coefficients as a function of particle number. The simulation predicts that interaction strength decreases with the particle number by 0.24% per particle.

Consider a geometry with six particles as shown in Figure 4.7a. The particles are positioned $3R$ apart, which omits the close distance hydrodynamics. The orange particle receives a thermal impulse and moves to the right with velocity v_0 . Its motion induces the Poiseuille flow that exerts a force on the other particles. In contrast to the previous approach, we allow the other particles to move at a response velocity, v_r , which corresponds to a zero net force on them. In this scheme correlation is simply the ratio $\rho = v_r/v_0$.

In COMSOL, we build on top of the simulation method described in Section 3.3 with the geometry shown in Figure 4.7a. To find the response velocity we run two simulations: one to estimate the drag and another one to compensate for particle motion. First, we solve for a moving orange particle, while keeping others fixed. This gives a drag force $F_{white}(v_r = 0)$. Then we move all the particles at the same velocity and estimate the resulting force, $F_{white}(v_r = v_0)$. Since our system is linear, we can simply interpolate where $F_{white}(v_r) = 0$, and thus obtain v_r . Finally, we verify that v_r is correct by solving for the orange particle moving at v_0 , while the white particles are moving at v_r . This always gives zero drag force on the white particles, as expected.

This allows to compute particle interactions for more than two particles, but it should be noted that it produces equivalent results as the previous method for $N = 2$. We further extend our generalised model by including the access resistance, as explained on page 49.

Figure 4.7b shows simulation results for particle interactions for up to six particles. The predicted correlation coefficient is almost constant with the particle number in the channel, where the interaction strength decreases by a mere 0.24% per particle. This agrees well with

our experimental observations presented in Figure 4.5. For this reason, we treat the correlation coefficient as a constant, which we evaluate at $N = 2$.

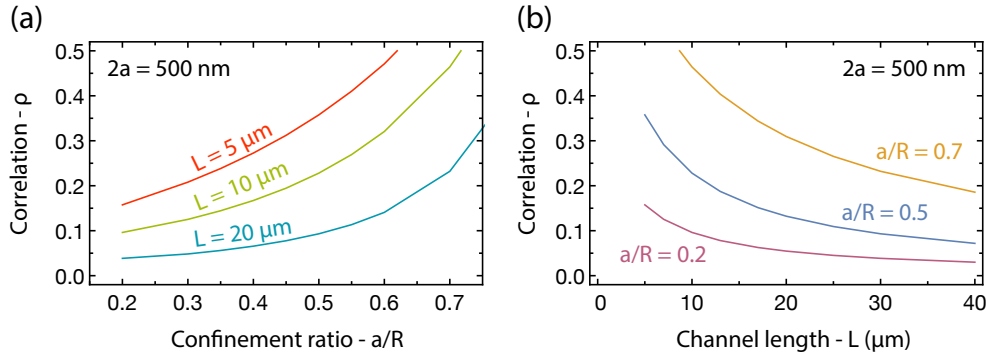


Figure 4.8: Simulation of hydrodynamic interactions for different channel widths and lengths. (a) Simulated correlation coefficient as a function of the confinement ratio. The interaction weakens with increasing channel width, but in the computed range it never reaches zero. (b) Simulated correlation coefficient as a function of channel length. The interaction slowly weakens with the channel length. In our simulations the interaction persisted even in $100 \mu\text{m}$ long channels (not shown).

Figures 4.8 (a) and (b) show predicted correlation coefficients for different channel widths and lengths. The particle interaction weakens with channel width, where in the limit $a/R \rightarrow 0$ we recover the normal particle interaction in the bulk. The interaction also weakens with the channel length, where in the limit $L \rightarrow \infty$ there is no interaction at large separations.

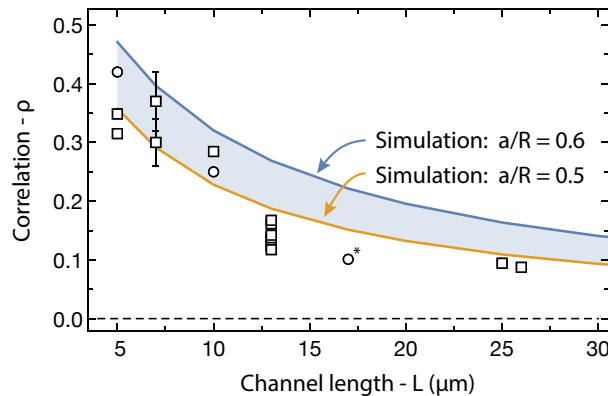


Figure 4.9: Correlation coefficient as a function of the channel length. Data points correspond to experimental values, where the shape indicates the cross-section shape: square for square channels, and circle for semi-elliptical channels. The point with the star had defects in the structure. Our simulations expect the correlation coefficients to be within the blue region, where the confinement ratios correspond to the experimental range, $a/R \in [0.5, 0.6]$. The experimental values are about 0.05 smaller than our simulation expects.

Figure 4.9 compares the simulation predictions with the experimental data. The overall agreement between the two is very good: our model captures the decay with channel length and also has correct magnitude, while we used no fitting parameters. However, the experimental values are smaller by ~ 0.05 , which suggests that there is a systematic over-estimate. One of the causes could be the centerline approximation, where the particles are placed in the middle of the Poiseuille flow in the simulation. Letting them move in the radial direction would decrease the interaction strength. Another possibility is that our model is too simple and does not capture all the energy dissipation modes. For example, it is known that sound carries away small amounts of energy and results in very different interaction modes [30, 34]. Nonetheless, our simple model agrees qualitatively with the experimental data, suggesting that channels must be modelled with periodic boundary conditions set on the inlets.

4.4 Discussion and special cases

In this section, we discuss the pressure exchange mechanisms, which are necessary for the nondecaying hydrodynamic interactions. Then we describe the relation between the correlation coefficient and other interaction metrics, justifying the extensive use of the correlation coefficient. Finally, we present three experiments that further verify our model for the particle interactions.

4.4.1 Pressure exchange mechanism

In our model, the moving particle induces a Poiseuille flow, which requires the two reservoirs to be in equilibrium. Otherwise, the pressure would build up and stop the Poiseuille flow. Mathematically, this equilibrium is achieved by imposing periodic boundary conditions on the inlets of the channel. Physically, this can be achieved with multiple channels, with a flexible membrane, or with open boundaries. Here, we discuss these alternatives in the context of our experiments.

First, the pressure can relax through other channels. In our experiments, chips S1, S2 and B4 have large channels connecting the two reservoirs as shown in Figure 3.4 (a) and (b). At the same time, there are at least five narrow channels across the barrier. All of them may facilitate pressure exchange between the reservoirs because the liquid can flow across the barrier. We test this idea experimentally by creating a chip with a single channel and no other connections between the two reservoirs (chip B2-10 μ m-1). This experiment is performed together with Soichiro Tottori, who also made the chip. The particles are positioned using the electrophoretic method. The measured correlation coefficient is $\rho = 0.28$, which agrees well with the previous measurements as seen in Figure 4.9 (the upper data point at $L = 10\mu\text{m}$). Therefore, this observation rules out the necessity of having multiple channels and also suggests that this phenomenon happens in a wide range of systems.

The second possible pressure exchange mechanism is via a flexible membrane separating the two reservoirs. In this case, an increased pressure deforms the membrane, without the need to exchange any liquid. There will be no net effect on the membrane in practice, since the pressure fluctuations are minuscule, short-lived, and have no directional bias. In practice, the PDMS is rather stiff [95], making it an unlikely explanation.

Lastly, the pressure fluctuations may be absorbed in the open boundaries or at the reservoirs themselves. For example, both reservoirs are exposed to air at the inlets. When one of the particles moves, it creates a short pressure increase that deforms the liquid-air boundary, but it is restored soon after. Or, alternatively, the reservoirs themselves might absorb the pressure fluctuations because the liquid is not truly incompressible. In both cases, we assume that

short-lived pressure fluctuations can be absorbed, while no build up of pressure would happen. However, these explanations are complex and further experiments are required to determine the nature of pressure exchange.

4.4.2 Relation between correlation and $\zeta_{i,j}$

Throughout this chapter, we used the correlation coefficient as a proxy for particle interactions, because its normalisation makes it easy to interpret and it is widely used in science. Here, we present the relation between the correlation coefficient and the hydrodynamic friction coefficients for the two particle system. From the definition of Pearson product-moment correlation coefficient we have [91]:

$$\rho = \frac{\text{cov}(\Delta x_1, \Delta x_2)}{\sigma_1 \sigma_2} \approx \frac{\langle \Delta x_1 \Delta x_2 \rangle}{\sqrt{\langle \Delta x_1^2 \rangle \langle \Delta x_2^2 \rangle}} = \frac{D_{1,2}}{\sqrt{D_{1,1} D_{2,2}}}, \quad (4.6)$$

where we used $\langle \Delta x_1 \rangle \approx 0$ and $\langle \Delta x_2 \rangle \approx 0$, which is satisfied exactly at large separations. In the third equality, we used the definition of diffusion matrix for two particles [93]: $D_{i,i} = \langle \Delta x_i^2 \rangle / 2\Delta t$ and $D_{1,2} = D_{2,1} = \langle \Delta x_1 \Delta x_2 \rangle / 2\Delta t$ [93]. Using Einstein-Smoluchowski relation Equation (2.4), we get the relation to the hydrodynamic friction matrix coefficients:

$$\rho \approx -\frac{\zeta_{1,2}}{\sqrt{\zeta_{1,1} \zeta_{2,2}}}. \quad (4.7)$$

This equation suggests that the correlation coefficient is directly proportional to the hydrodynamic friction coefficient corresponding to the particle-particle interaction, $\zeta_{1,2}$. Furthermore, ρ is normalised with particle-channel interaction, which makes it less sensitive to variations of the confinement ratio. For two particles of the same diameter, we need only two parameters to quantify the particle behaviour: one for particle-channel interaction, and one for particle-particle interactions. Therefore, we often present either $\{D_x/D_0, \rho\}$ or $\{\zeta_{1,1}/\zeta_0, \zeta_{1,2}/\zeta_0\}$.

We validate this relation by analysing virtual trajectories with known hydrodynamic properties. These trajectories are generated using a random walk method called the Brownian dynamics simulation [96]. Two particles are placed in a 1D channel. The electrostatic repulsion is modelled as an exponential potential with the decay rate set to the Debye length. The hydrodynamic interactions are taken from the COMSOL simulations for friction matrix coefficients. Interpolation is used to get all particle separation values. The generated trajectories are sub-sampled at 30 fps. The code for this simulation is available at [97].

The trajectory analysis yields the friction coefficients that match the input from the COMSOL simulations. This confirms that trajectories can be used to estimate the hydrodynamic

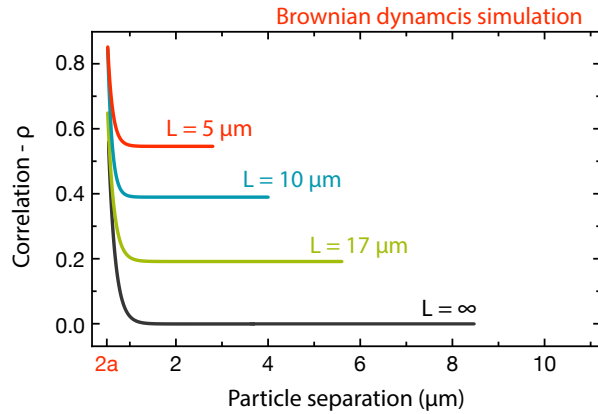


Figure 4.10: Brownian dynamics simulation for the two particle correlation coefficients. In this simulation [96] the effects of dynamic evolution were assessed by computing 1D trajectories for particles with repulsive potential and hydrodynamic interactions. Hydrodynamics were taken from the COMSOL simulation for friction matrices. No fitting parameters were used. The curves show similar behaviour to the experimental data seen in Figure 4.3. Noticeably, the simulated values are higher, because predicted friction matrices underestimate the diagonal elements – see Figure 4.4. This simulation demonstrates that our experimental analysis does not introduce artefacts into interaction measurements.

coefficients. Furthermore, we confirmed that Equation (4.7) holds at large particle separations, where Figure 4.10 shows the simulation results for different channel lengths.

4.4.3 Varying particle size

To further test the universality of our interaction model, we perform experiments with smaller particles. Figures 4.11a, 4.11b and 4.11c show friction coefficients for pairs of particles with different diameters. Notice that small particles have smaller hydrodynamic friction with the channel, $\zeta_{1,1}$ or $\zeta_{2,2}$. Also, the interaction between the particles decreases with the particle size, which is expected from our interaction model. For quantitative comparison, the solid lines show simulation results that have no fitting parameters. At large separations, our model correctly reproduces the friction coefficients. Meanwhile, at close proximity, the measurement errors and electrostatic interactions contribute to the large discrepancies. Importantly, these results further validate our model with the periodic boundary conditions.

4.4.4 Interaction at the entrances

As a further control we measured how the nondecaying interaction changes at the entrances of channels. In this experiment, we position one particle in the middle of a channel, and the other

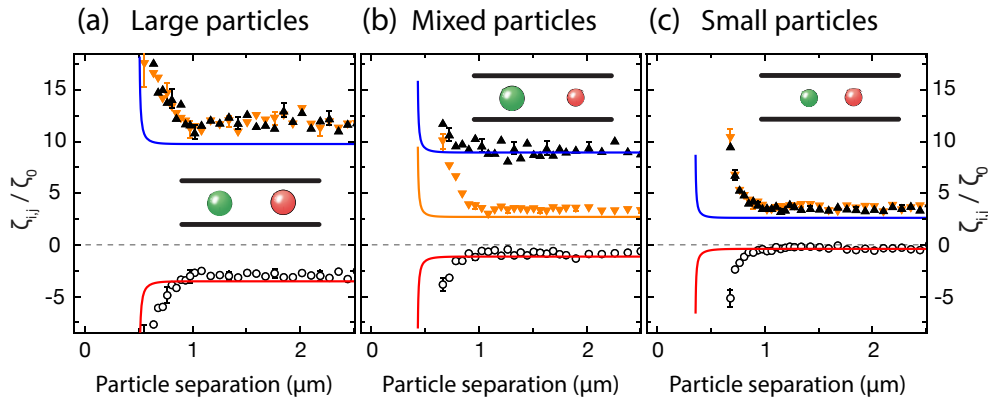


Figure 4.11: Friction matrix coefficients for different particle sizes. All experiments were performed in a $L = 10\mu\text{m}$ long open channel with a mixture of particle sizes: (a) 500nm and 500nm; (b) 500nm and 350nm; (c) 350nm and 350nm. The points are the experimentally measured values: \blacktriangle for $\zeta_{1,1}$; \blacktriangledown for $\zeta_{2,2}$; and \circ for $\zeta_{1,2} = \zeta_{2,1}$ is the interaction term. The solid lines show the simulation results: $-$ for $\zeta_{1,2} = \zeta_{2,1}$; $-$ for $\zeta_{1,1}$; and $-$ for $\zeta_{2,2}$. All values are normalised with the friction coefficient in the bulk: $\zeta_0 = 6\pi\eta a$. Error bars are shown for every fifth data point. Simulations were performed using a cylindrical channel that has a width of 800 nm and a length of $10\mu\text{m}$. No fitting parameters were used in the simulations. Disagreement at small separations is caused by electrostatics, finite frame rate, and position tracking errors. At large separations the simulation results agree well with the experimental data in all cases, suggesting that the proposed interaction model is correct.

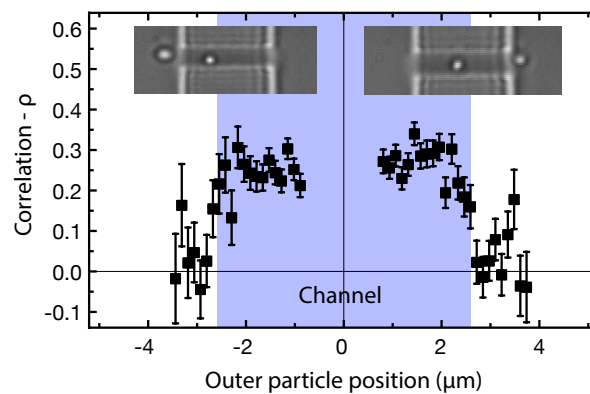


Figure 4.12: Correlation coefficient versus the position of the right particle on the right half, and the left particle on the left half, while the other particle is inside the channel. The colored area shows the boundaries of the channel. Experimental parameters are: $2a = 505\text{ nm}$; $L = 5\mu\text{m}$.

one at $\approx 0.5\mu\text{m}$ away from either inlet. The latter particle typically escapes the channel before the former one. From their trajectories, we measure the correlation coefficient in the usual way.

Figure 4.12 shows the correlation coefficient as a function of the position of the escaping particle. The interaction strength decays to zero when the particle leaves the channel. This decay starts while the particle is still in the channel. For this reason, our interaction analysis always excludes a region of $0.5\mu\text{m}$ around the inlets.

4.4.5 No external oscillations

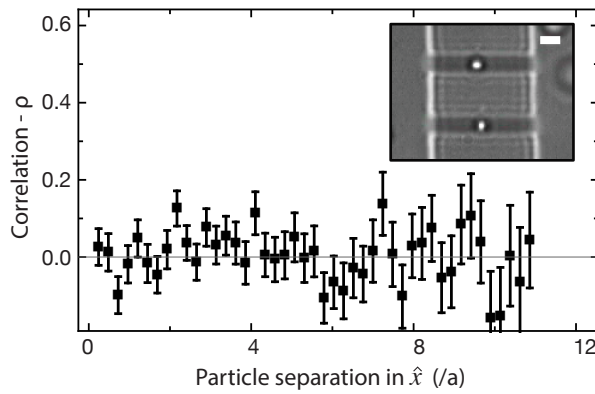


Figure 4.13: Correlation coefficient between two particles placed in separate channels. Horizontal axis indicates the particle separation in \hat{x} direction. Particles were positioned in separate channels (inset) to test if there is any correlations due to external flows. No correlation was observed. Channels were $L = 5\mu\text{m}$ long. The scale bar indicates $1\mu\text{m}$.

An alternative cause for the particle correlation could be externally driven pressure fluctuations, like sound waves. We eliminated this possibility by measuring the correlation between particles in separate channels, as shown in the inset of Figure 4.13. If an external driver causes the correlations, the motion in separate channels would also be correlated. Figure 4.13 demonstrates that there is no correlation between two particles in separate channels, suggesting that an externally oscillating flow does not cause the nondecaying interactions.

4.5 Conclusion and impact

We utilised a highly controlled microfluidic system coupled with holographic optical tweezers to investigate the interaction of particles in confinement. Our measurements prove that interactions extend over the full channel length and have a constant strength that does not decay with particle separation. We explain the coupling mechanism using hydrodynamics with both a qualitative

analytical model and quantitative comparisons with the numerical simulations. The excellent agreement between the theory and the experiments suggests that we understand the properties of hydrodynamic particle interactions in microfluidic channels. The nondecaying interaction extending across the whole channel has significant implications for transport through channels. Here, we present few examples.

First, the diffusion coefficients are higher. Our interaction model suggests that pressure in front of the moving particle has an additional relaxation mode. This reduces the hydrodynamic drag, resulting in higher diffusion coefficient. We have analysed this in Chapter 3, where our model agrees with the experimental data, as shown in Figure 3.26. Therefore, our model is important for predicting the diffusivity of particles.

Secondly, the collective dynamics is fundamentally different, since all particles interact with each other over arbitrary distances. This will affect single-file diffusion, where the local particle interactions cause a transition to a sub-diffusive regime. We expect that the newly discovered non-local interactions prolong the transition from Fickian diffusion to the sub-diffusive domain [94]. In biology, such interactions might be used to control transport rate through protein pores. Imagine a molecule trapped in a potential, where it can only escape if a second molecule enters the same channel and contributes an additional push. It also affects polymers in confinement, because the monomers are coupled through hydrodynamics. This might influence the confirmation of the entire polymer.

Finally, our model suggests that particles moving due to an externally applied force should also induce the Poiseuille flow. Therefore, driven particles should experience similar hydrodynamic interactions, which is particularly important for technological applications, such as electrophoresis or pressure flow. We explore this idea in Chapter 5.

Chapter 5

Driven Transport

In this chapter, we study the hydrodynamic particle-particle interactions for driven particles. Three driving sources are considered: pressure flow, electric fields, and gravity. We will demonstrate that they each produce a different particle-particle interactions.

Pressure driven particles have been extensively studied theoretically [39, 98–100] and experimentally [101, 102]. In large channels, particles move with the flow without perturbing it [39]. Therefore, such particles do not experience hydrodynamic interactions. In narrow channels, on the contrary, each particle contributes to a small pressure drop, thus slowing down the flow [98]. As a result, the particle velocity should decrease with the number of particles inside the channel. However, note that such interaction originates from hindering the flow and does not involve the piston-like effect that causes the nondecaying interactions.

In contrast, when a charged particle migrates in an electric field, it induces a flow around it. Other particles in the vicinity move with the induced flow, thus resulting in hydrodynamic interactions. This interaction has been studied extensively in bulk [103–107], but is much less well studied in narrow channels. The absence of experimental studies might be due to an increased complexity in confinement, because there are three additional components to consider [53]: (1) electric charge on the channel walls causes electro-osmotic flow; (2) the channel alters the interaction between the particle and the applied electric field; (3) the channel increases the hydrodynamic friction. These effects have been studied extensively for isolated particles [53, 108–110] and confirmed experimentally in long channels [26, 111–114]. Meanwhile, the particle-particle interactions in channels have received limited attention with only a few theoretical studies [115, 116], which used the infinite channel approximation. Naturally, they predict no interactions when particles are separated by more than $2R$. This problem has also been studied by the gel electrophoresis community, but to the best of our knowledge, they omit any long ranged hydrodynamic effects [26]. Here, we will experimentally investigate

the hydrodynamic interactions between particles migrating in an electric field. Then we will compare our results with our interaction model that utilises the periodic boundary conditions.

Finally, we drive particles with gravitational force that acts only on the mass of the particle. This simplifies the theoretical description, thus allowing us to test our interaction model. The experiments themselves are similar to the falling-ball viscometers [117], where a ball falls under gravity in a cylindrical channel. This technique is often used to determine the viscosity of the liquid, but instead, we focus on particle-particle interactions during the fall.

We start by introducing the experimental techniques for controlling pressure, electric fields, and gravity. Then we will discuss single particle electrophoresis through microfluidic channels, which is necessary for understanding the complex interplay between the different phenomena happening during electrophoresis in channels. Afterwards, we will present our principal findings on particle-particle hydrodynamic interactions for different driving sources. Importantly, we find a constructive interaction between particles that are driven by electrophoresis or gravity, but no interaction between the pressure driven particles. We will then explain these results with simulations that incorporate the periodic boundary conditions.

5.1 Methods for driving particles

We devise methods for applying each force: pressure, electric fields, and gravity. The pressure control system is used in each experiment, since it allows quick pressure equilibration between the two reservoirs.

5.1.1 Pressure

To apply pressure across the channel, we attach a PVA tubing to the inlets of the microfluidic chip, as shown in Figure 5.1a. The other ends are attached to 1 mL syringes that perform the function of large reservoirs. One of these reservoirs is fixed, while the other one can move up or down on a translation stage controlled by a micrometer drive. Adjusting it creates a height difference between the reservoirs, which corresponds to the pressure exerted on the liquid:

$$\Delta p = -\rho_f g \Delta h \quad (5.1)$$

where g is the acceleration of gravity, ρ_f is liquid density, and Δh is the height difference. The micrometer drive has engravings every 10 μm , which corresponds to a pressure difference of $\Delta p_{\text{min}} \approx 0.1 \text{ Pa}$. Applying such pressure across the barrier induces a flow of $\langle u \rangle \sim 7 \text{ nm/s}$, which

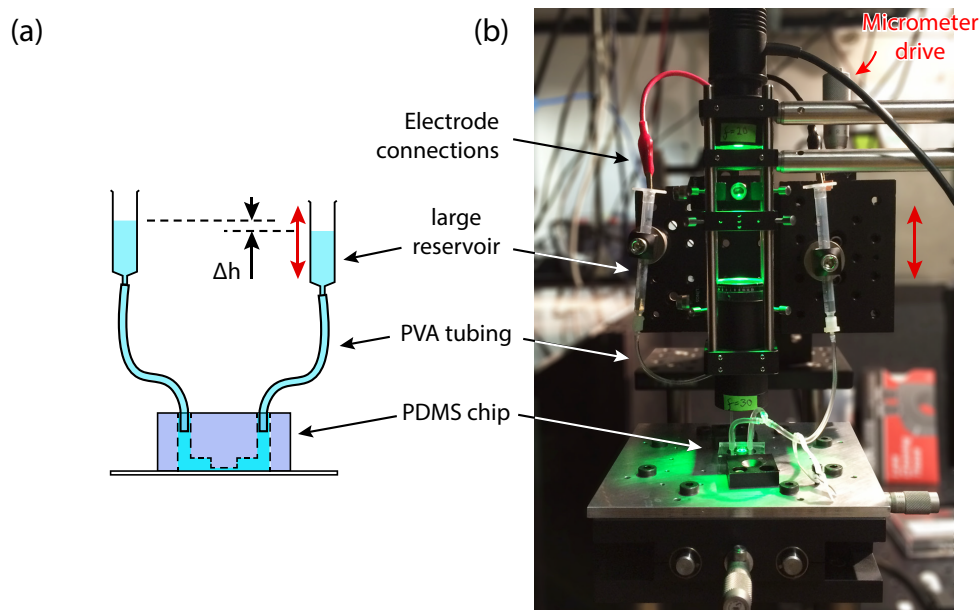


Figure 5.1: Method for applying pressure using a micrometer drive. (a) Setup diagram: the microfluidic chip is connected to tubing, which is connected to two large reservoirs. The right reservoir is mounted on a translation stage that can move up or down as highlighted by the red arrow. This creates a height difference between the liquid in the reservoirs, thus creating a pressure difference. (b) Picture of experimental implementation of pressure regulation system. In addition, the crocodile clips are connected to platinum wires that are dipped in the reservoirs. These electrodes apply an electric potential.

allows to precisely control particle motion and flows within the channel. Figure 5.1b shows the complete setup.

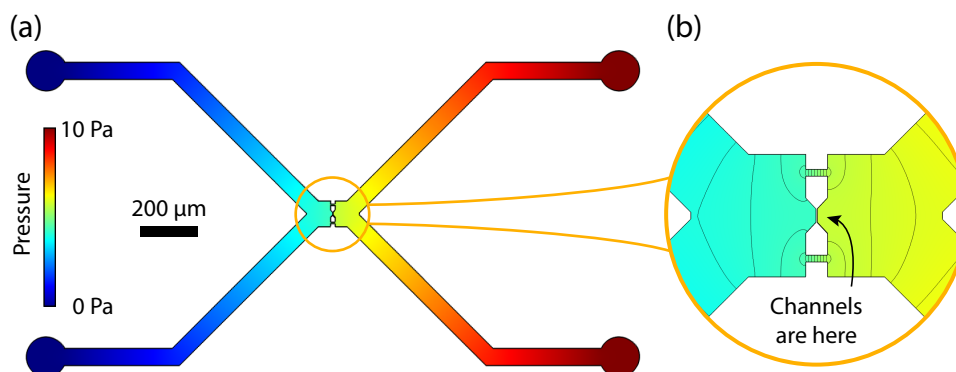


Figure 5.2: Simulation of pressure drop across B4 class chips. (a) 10 Pa are applied across the chip, which decreases gradually across the entire chip. The pressure across the small channels, located in the middle of the chip, is 1 Pa or 10% of the initial pressure. (b) Shows a close up, where the black lines indicate pressure contours. The pressure is constant across all the channels.

Not all of the pressure drops across the barrier. Figure 5.2 shows a simulation of pressure drop in the microfluidic chip. Notice that the pressure across the channels is only 10% of the applied pressure. This reduction is caused by the secondary large connections and it allows us to control the pressure difference to a greater precision.

The addition of the PVA tubing makes filling the chip more complicated. We pre-fill the chip as described in Section 3.1 and then insert the empty tubing. Using a syringe with a thin needle, we pierce the PDMS and inject the solution directly into the chip. This drives the air out of the tubing, leaving it filled with no air bubbles. Once the needle is removed, the hole plastically seals itself.

To find the pressure equilibrium between the reservoirs, we observe the direction of particle migration in the channel, and then adjusted the pressure to counter this motion, until no noticeable migration is left.

5.1.2 Electric fields

Our polystyrene colloidal particles have a small negative charge, which causes electrophoretic migration in an external electric field. To create the electric field, we immerse two electrodes into the reservoirs, as shown Figure 5.1b. The other ends of the electrodes are connected to a computer controlled DAC (NI USB-6211) that applies an electric potential. This completes the electrical circuit, allowing us to create electric fields inside the channel.

The electric field lines follow the conducting liquid, thus focusing the field into the channels. We model this using a COMSOL simulation with an Ohmic conductivity assumption. Figure 5.3a shows a simulation for electric potential in the chip. As with the pressure, much of the electric potential drops in the access connections, while only about 14% of the potential drops across the barrier. Note that simulation did not include the PVA tubing, which is expected to increase electrical resistance.

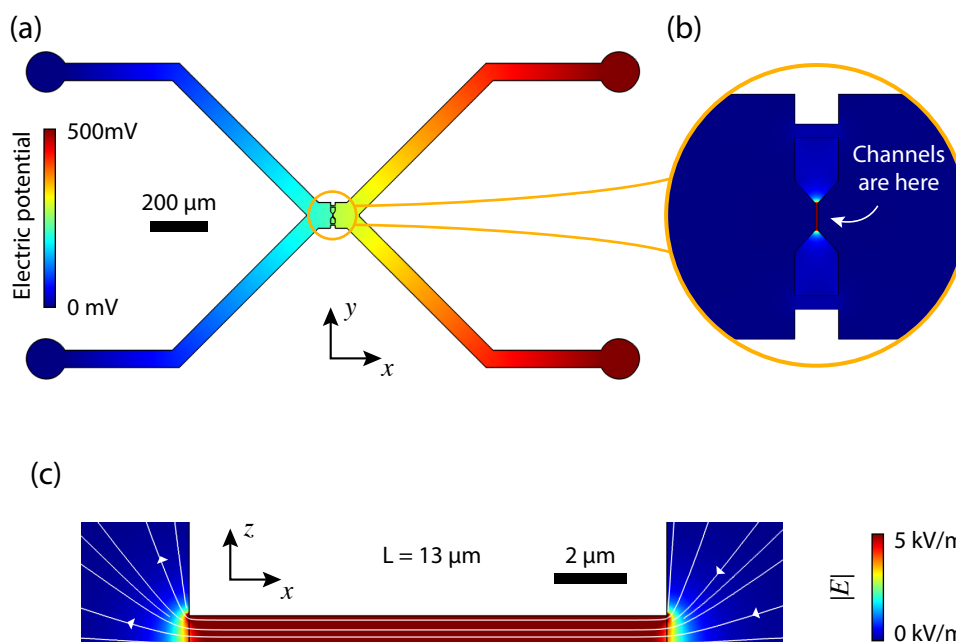


Figure 5.3: Simulation of electric fields in B4 class chip. (a) Shows electric potential that is applied at the circular inlets. The potential drops gradually with the steepest drop of $\sim 14\%$ happening across the barrier. (b) Shows electric field strength in the middle of the chip, where the barrier is located. The strength is uniform along the barrier. (c) Shows a simulation of electric fields in a single channel with a square cross-section. The electric field is uniform inside the channel, but varies around the entrances (the variation extends $\sim 400\text{nm}$ into the channel).

Figure 5.3b shows a simulation for a single channel with a square cross-section. The electric field gets focused into the channel, where its strength reaches approximately 5 kV m^{-1} . Inside the channel, the electric field is uniform, suggesting that electrophoretic velocity should be constant throughout the channel. However, if the channel tapers, the electric field varies with position, which would result in speed-up or slow-down of the particles¹. In either case, the field variation is small inside the channel, suggesting that dielectrophoresis is negligible.

¹We avoid using term acceleration, since it implies velocity change in time. Here the velocity is changing with respect to position.

Throughout this chapter, we focus on measurements of relative velocity, because determining electrical mobility requires precise knowledge of many parameters that have high experimental uncertainty in our system, such as particle charge and the electric field strength, where the latter depends on the geometry. Thus, we circumvent these uncertainties by performing relative measurements.

Electrodes and salt solution

We explored two sets of electrode/solution pairs. First, we used silver/silver-chloride electrodes with 5 mM KCl solution. This approach produces all the effects that will be described in following sections. However, these electrodes showed a significant drift that decreases the electrophoretic velocity over time. We think this is caused by electrode degradation, because after about five hours we were unable to drive the particles. Furthermore, this electrode/solution pair produces a membrane polarisation that is discussed in Section 5.1.5. For these reasons, we switched to platinum electrodes (0.2 mm, purity 99.99%, Advent PT5415) and added 1 mM Potassium Ferricyanide and 1 mM Potassium Ferrocyanide (FF) salts to decrease the reduction potential [118]. The resulting redox pair is more stable [119–121], allowing us to run the experiment for 5 hours or longer. Therefore, the platinum electrodes with KCl and FF salt is our preferred method for driving particles.

Buffering to increase stability

In experiments, the particle velocity decreases over time, which we attribute to a pH drift. Therefore, we add either MES or HEPES buffers that have $pK_a = 6.15$ and $pK_a = 7.55$, respectively. The molar concentration of the buffering agent is kept low to avoid offsetting the salt concentration; typically it is 1.6 mM.

Figure 5.4 shows a comparison of buffered and unbuffered solutions over time. Typically, the buffered solutions are stable for at least 4 hours, with an average velocity decrease of $2.232 \mu\text{m s}^{-1} \text{V}^{-1}$ per hour. Meanwhile, the unbuffered solutions show orders of magnitude larger drifts that varies between experiments. For this reason, we kept experiments with unbuffered solutions brief; typically around 30 minutes long.

For safety, we measured the velocity drift in each experiment. Normally, the drift was below 5% for the duration of the experiment. If it exceeded 10%, the experiment was automatically discarded from further analysis.

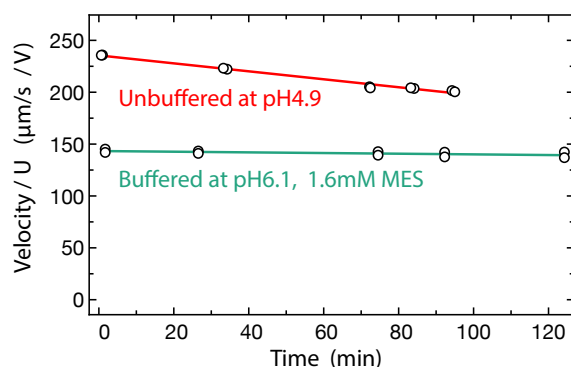


Figure 5.4: Stability of electrophoretic velocity for buffered and unbuffered solutions. The lines show linear fits where the slopes are: $23.0 \mu\text{m s}^{-1} \text{V}^{-1}$ per hour for unbuffered solution, and $1.93 \mu\text{m s}^{-1} \text{V}^{-1}$ per hour for buffered solution. Buffering increases the stability of the sample by an order of magnitude.

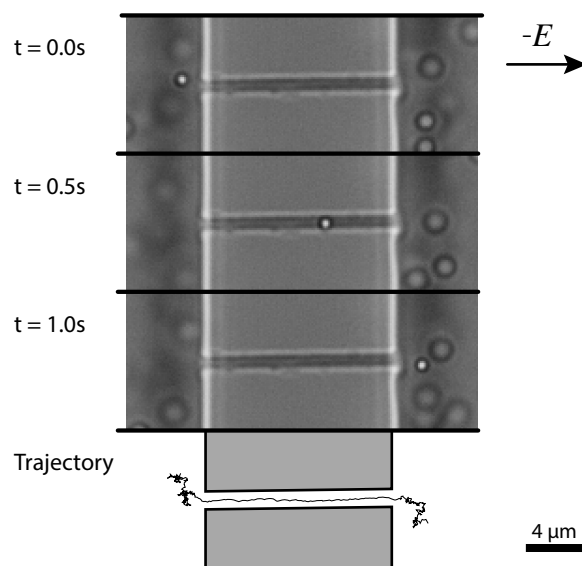


Figure 5.5: Images of a particle moving through a channel in an external electric field. The bottom image shows the corresponding trajectory, where the tracking begins once the particle enters the focus plane and ends with the particle exiting the focal plane on the right. The particle took 0.45 seconds to pass the channel at $U = 200 \text{mV}$.

5.1.3 Electrophoresis of isolated particles

This section investigates electrophoresis of isolated particles inside channels. Figure 5.5 shows sample images for one such event and the corresponding trajectory. We aim to explain the procedure for data analysis and to lay the foundations for understanding driven particle transport.

For the analysis, we select segments of the trajectories that satisfy the following criteria: here we are interested in single particle motion, and thus, we discard frames with more than one particle, leaving only trajectory segments with $N = 1$. Then we discard frames with particles stuck to the channel walls or stuck to other particles, both of which were rare. Lastly, we discard frames where the particle is closer than 500 nm from the either inlet, since the electric field varies around the inlets, as shown in Figure 5.3c.

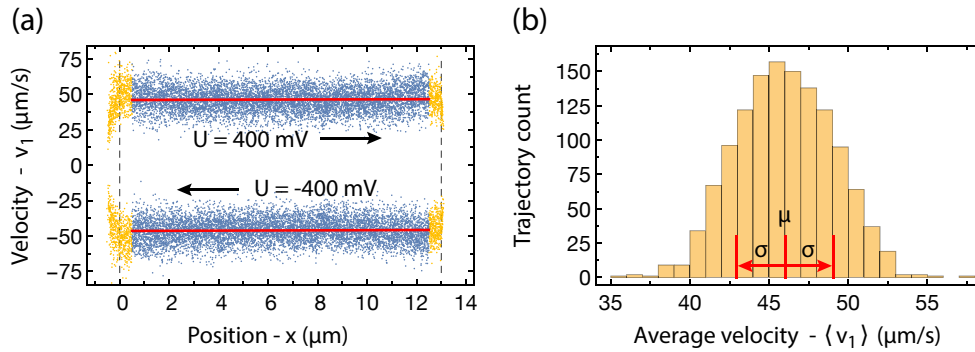


Figure 5.6: Electrophoresis of a single particle in a $L = 13 \mu\text{m}$ long channel. (a) Velocity as a function of position inside the channel. The upper part corresponds to the particles moving under a positive electric potential, while the lower part corresponds to a negative potential. The dashed lines indicate channel bounds. The blue points were used for subsequent analysis, while the yellow points were discarded. The red lines correspond to linear fits, which are almost completely horizontal. (b) Histogram of average velocities of trajectories. For each trajectory, an average velocity was computed from ~ 50 frames with an estimated error of $1.5 \mu\text{m/s}$. The middle red line indicates the mean of the distribution at $\mu = 46.0 \mu\text{m/s}$, where the variation around it is $\sigma = 3.0 \mu\text{m/s}$. This variation is a consequence of the measurement error and a variation of particle size.

Figure 5.6a shows the measured velocities at different positions in the channel. The yellow data points are discarded since they do not pass the criteria, while the blue points are analysed further. The velocity is uniform everywhere except around the inlets, as expected. Notice that we measure at positive and negative electric potentials, which allows us to verify that our system is symmetric.

In Figure 5.6a, the measured velocities scatter around the averages, shown as the red lines. This variability is caused by the measurement errors, the Brownian motion, and an intrinsic

variability of particle mobility. The latter depends on the size and charge of the particles. To measure this intrinsic variability, we calculate the average velocity for each trajectory, thus eliminating the former two effects. Figure 5.6b shows the resulting distribution, which has a mean of $46.0 \mu\text{m/s}$ and a standard deviation of $\sigma = 3.0 \mu\text{m/s}$. The width of this distribution depends on the measurement errors ($\approx 1.5 \mu\text{m/s}$) and the variability of the particle mobility. We subtract the former and get that average velocities varied by $2.6 \mu\text{m/s}$ or $\approx 5.6\%$. This value agrees with other measurements that are presented in Appendices B.3 and B.4.1. The nominal size variation for our colloids is $\text{CV} = 2\%$, which is smaller than the measured variation, but remember that the friction coefficient has the non-linear response to the confinement ratio, as discussed in Section 3.3.1. In addition, the variation of surface charge density also contributes.

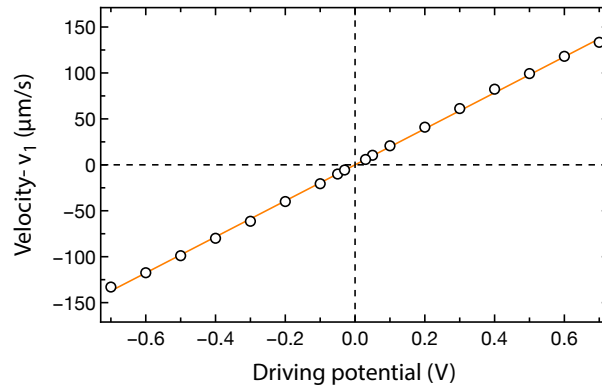


Figure 5.7: Electrophoretic velocity as a function of the electric potential (B4-13 μm -2). The orange line is a linear fit to the data, suggesting a linear relationship between applied potential on the electrodes and the velocity. The small deviation away from the linear regime is caused by the pH drift.

We also checked that the particle velocity is proportional to the applied electric potential, as shown in Figure 5.7. This linear relation is expected by the theory that was discussed in Section 2.3.5.

5.1.4 Electrophoretic velocity versus c_0 and pH

The same theory from Section 2.3.5 suggests that the electrophoretic velocity decreases with salt concentration and varies with the surface charges. Therefore, we expect our system to depend on the salt concentration and the pH, which is inversely proportional to the surface charge density [45, 122].

We investigate these dependences by performing two experiments: one for varied c_0 , and another for varied pH. For the first experiment, we prepared multiple solutions with pH 7, 1 mM FF salt, and a varied KCl concentration. To minimise other effects, we used a single

PDMS chip for all the c_0 values by flushing the chip with new solutions. For this experiment, we additionally coated the coverslip with a thin layer of PDMS (thickness below 0.15 mm, method [123]), because we empirically observed that the colloids stick less to the PDMS than to the glass. This is particularly important at high salt concentrations, where the electrostatic repulsion is weak. For the second experiment with varied pH, we prepared a new chip without the PDMS coated coverslip, and performed the same flushing procedure. This time, the salt concentration is fixed at 5 mM, while the pH is varied. The pH is increased by adding KOH, or decreased by adding HCl. We used micro-molar amounts to change the pH; thus, the baseline salt concentration was unaffected.

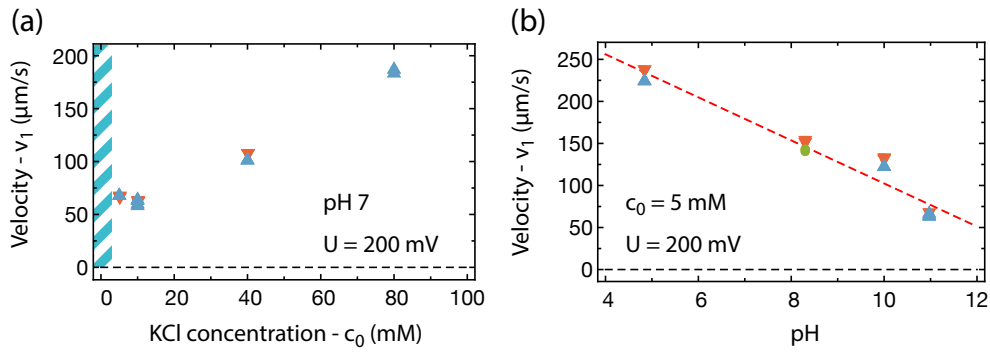


Figure 5.8: Electrophoretic velocity of a single particle as a function of (a) salt concentration and (b) pH. The markers indicate different channels: \blacktriangledown for channel 2; \bullet for channel 4; \blacktriangle for channel 5. In both experiments, B4-13 μm chips were repeatedly flushed with new solution containing different salt concentration or different pH. In all cases, the solutions contain 1 mM Potassium Ferri/Ferrocyanide. The pH was controlled by adding KOH or HCl in minuscule amounts. (a) The blue area highlights $c_0 = 3$ mM and $c_0 = 1$ mM experiments, where particles could not enter the channel due to a strong electroosmotic plug flow in the channel. The errors in the c_0 are expected to be about 15%. In this experiment, the coverslip was coated with a thin layer of PDMS to reduce sticking [123]. (b) The red line indicates a linear fit that reads $v_1(\text{pH}) = 358.5 - 25.6\text{pH}$. The errors in pH values are about 0.2.

Figure 5.8a shows that the electrophoretic velocity increases with the salt concentration, which is opposite to the expected behaviour: Equation (2.25) suggests that $v_{net} \propto c_0^{-0.5}$. This discrepancy is likely caused by an increasing charge density of the polystyrene particles with the salt concentration [124]. On the other hand, the literature suggests that PDMS surface charge density is approximately constant for all c_0 [125]. Therefore, the velocity scales as $v_{net} \sim \sigma_p \sim c_0$. However, it also suggests that polystyrene particles are a poor model system for studying the dependence on salt concentration, because multiple parameters get affected. In this thesis, we keep using the same particles to allow a comparison between different experiments, but note that further experimentation is required to understand the dependence on the salt concentration. Finally, we also note that particle velocity typically decreases with c_0 in bulk [124]. However,

we observed an increasing velocity with c_0 in channels, which might have practical applications for classifying particles.

Figure 5.8b shows the electrophoretic velocity as a function of the pH. The velocity decreases with the pH, because it affects the surface charge densities [45, 122]. Specifically, the PDMS surfaces become more negative at higher pH, because the H^+ dissociates from the surface leaving negatively charged groups on the surface [122]. Furthermore, the pH also affects the surface charge on the polystyrene colloids, but the variation is weaker [45, 124]. Therefore, from Equation (2.25), we get $v_{net} \propto \sigma_p - \sigma_w \sim -pH$, which agrees with our experimental data.

In both cases, further experiments are required to understand how the electrophoretic migration in channels is affected by the solution. However, our goal is to study the hydrodynamic interactions, and therefore, we limit ourselves to this basic study. To minimise variability between experiments due to changing solutions, we keep a constant particle density of 36 particles/pL (or 0.25% solids (w/v)) and sometimes buffer the solution to reduce the pH drift.

5.1.5 Charge polarisation with Ag/AgCl electrodes

In early electrophoresis experiments we used 5 mM KCl solution with Ag/AgCl electrodes, since silver chloride electrodes are widely used in our lab to drive molecules through nanopores. However, in our experiments, the currents are much higher, because we have multiple channels with large cross-sections. This results in complete electrode degradation within 3–4 hours of the experiment. To avoid these problems we switched to platinum electrodes with ferri/ferrocyanide salt, which is very stable. Both systems exhibit the same phenomena with one exception – the particle velocity profile looked different when using the Ag/AgCl electrodes with 5 mM KCl.

To quantify this, we measure the isolated particle velocity at different positions within the channel. The details of our analysis are discussed in Section 5.1.3. Figure 5.9a shows the velocity as a function of position for platinum electrodes with FF salt. The velocity is constant, as expected for the constant electric field shown in Figure 5.3c. All the experiments were run in both directions to check for any asymmetries. Normally, the lines were both horizontal as shown, but some channels had a tapering, resulting in lines converging towards each other on one side.

The behaviour is different for silver chloride electrodes with no FF salt. Figure 5.9b shows the velocity distribution, where the particles clearly speed-up inside the channel. It looks like acceleration, but the particles reach terminal velocities in microseconds due to the strong hydrodynamic friction. Furthermore, the speed-up is not caused by channel shape, because we could not observe any tapering optically, and the reversal of potential keeps the speed-up

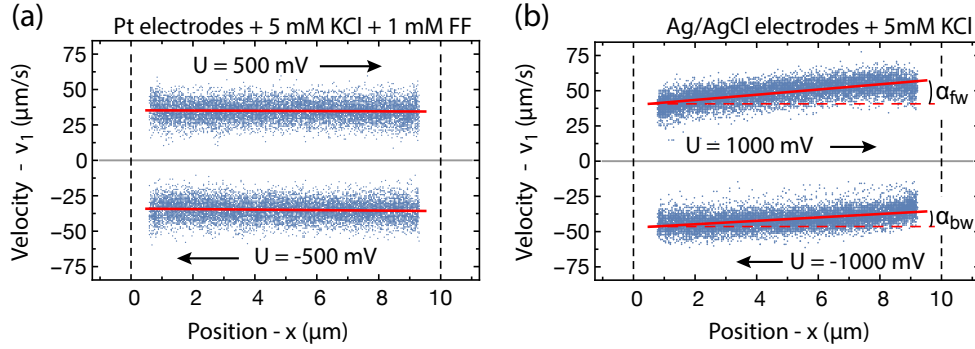


Figure 5.9: Particle velocity as a function of particle position in the channel for (a) Pt electrodes with 5 mM KCl + 1 mM FF solution, and for (b) Ag/AgCl electrodes with 5 mM KCl solution. The experiments were performed in channel S3-10um-1, where the entrances of the channel are indicated by the vertical dashed lines. The red lines are linear fits to the data. For the platinum electrode system, the particle velocity is constant throughout the channel. The angles to the horizontal axis are $\alpha_{fw} = -0.10 \pm 0.10 (\mu\text{m/s})/\mu\text{m}$ and $\alpha_{bw} = -0.18 \pm 0.10 (\mu\text{m/s})/\mu\text{m}$. On the contrary, for the silver electrode system, the fits intersect the horizontal axis at an angle, suggesting that particles were speeding up along the channel. The angles to the horizontal axis are $\alpha_{fw} = 1.82 \pm 0.10 (\mu\text{m/s})/\mu\text{m}$ and $\alpha_{bw} = 1.20 \pm 0.10 (\mu\text{m/s})/\mu\text{m}$.

direction, and switching to platinum system removed it. Therefore, we believe that this velocity speed-up indicates the electric field variation.

The cause of this electric field variation is unknown. One possible explanation is that a concentration polarisation produces electric field gradients. In such case, the ion concentrations across the barrier are slightly different because the channel is weakly permselective to positive ions [126, 127]. This uneven ion distribution produces an electric field variation that may explain the observed particle speed-up [128, p. 131].

To test this idea, Nadanai Laohakunakorn ran a simulation [129] with the typical dimensions of our channels. However, the resulting concentration polarisation was small, resulting in a negligible electric field variation. Such outcome was expected because our channels are much wider than the Debye length, resulting in a weak ion selectivity. We hypothesise that the presence of charged particles may induce the desired ion selectivity, because the effective cross-section becomes smaller. However, this does not explain why introducing 1 mM FF salt removes the effect. This is still an unresolved problem.

5.1.6 Gravity as driving force

Gravity pulls the mass of the particles earthwards. Normally, this effect is unnoticeable in our experiments, since the force is weak and the buoyancy counteracts it. The combined force is given by Equation (2.18). For our polystyrene colloids the force is only $F_g(\text{polystyrene}) \approx$

0.03 fN, that is equivalent to a terminal velocity of ≈ 7.5 nm/s. This minuscule force is not enough to counteract the Brownian motion, thus we neglect the gravitational pull in our experiments with the polystyrene particles.

However, heavier particles can be driven by gravity. For example, gold has a density of $\rho_p \approx 19300$ kg/m³, which corresponds to $F_g(\text{gold}) \approx 12.7$ fN for particles of width $2a = 400$ nm. Their terminal velocity is ≈ 2.7 μ m/s, which can be measured with our microscopy technique. Therefore, we used 400 nm gold nanoparticles (stabilised in citrate buffer; from Sigma-Aldrich; catalogue no 742090).

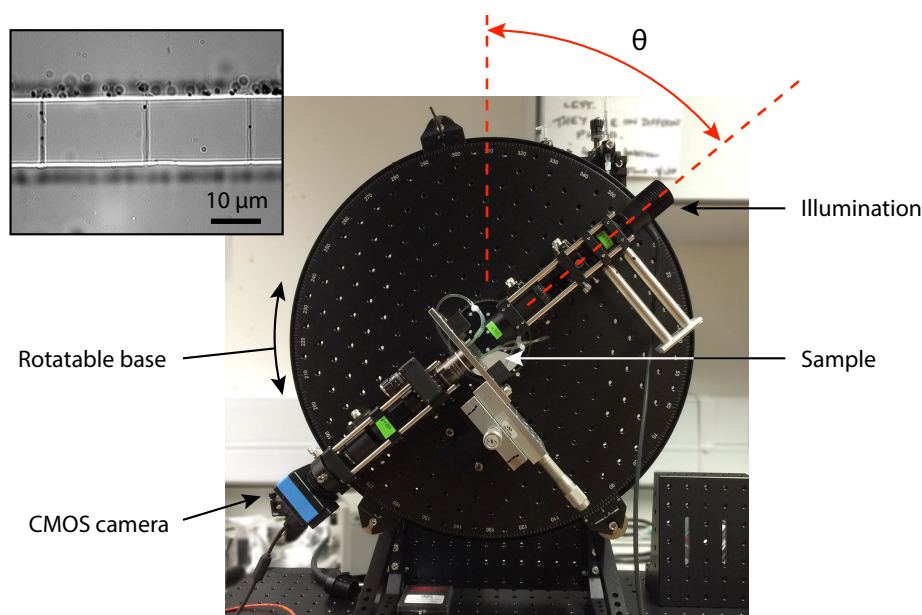


Figure 5.10: Tilt-able microscope for experiments with gravity driven particles. All optical components and the microfluidic chip are mounted on a rotatable base, while pressure control mechanism is mounted on a fixed platform. The angle of the base is θ , where at $\theta = 0$ the channels are in a horizontal position. A $100\times$, 1.4 NA, UPLSAPO objective was used. The inset shows an image of gold nano-particles falling under the influence of gravity at $\theta = \pi/2$.

For this purpose, we built a microscope on a rotatable base, as shown in Figure 5.10. It allows us to rotate the microfluidic chip at an angle θ to the horizontal plane. The force on the particles can be adjusted by changing θ , but we mostly ran the experiments at either 90° or -90° to avoid a force component towards a wall. Tubing and external reservoirs were added to eliminate the pressure fluctuations that occur during rotation (see Section 5.1.1). Critically, the external reservoirs were mounted on a stationary base.

The gold nanoparticles have a small signal to noise ratio when in focus, and therefore, we used an out of focus plane, where the nanoparticles appear black. Inset in Figure 5.10 shows a typical image, where the gravity is pulling particles downwards. Notice that particles

are pressing against the barrier, because the force vector always points downwards and the particles have to find the channel mouth accidentally. In contrast, pressure flow and electric fields converge towards the channel mouth. This difference reduces the number of translocation during gravity driven transport, leading to a much smaller data acquisition rate and thus larger statistical uncertainties. Furthermore, sometimes particles coalesced while bouncing against the wall, which in turn, blocked the channel and reduced the duration of the experiment. As a result, we have a low number of trajectories for the gravity fall experiments (below 100 trajectories per channel per experiment).

5.2 Driven particle interactions

The nondecaying hydrodynamic interactions should exist not only for particles undergoing Brownian motion, but also for particles driven through channels. In this section, we experimentally investigate this hypothesis with three different driving sources: pressure, electric fields², and gravity.

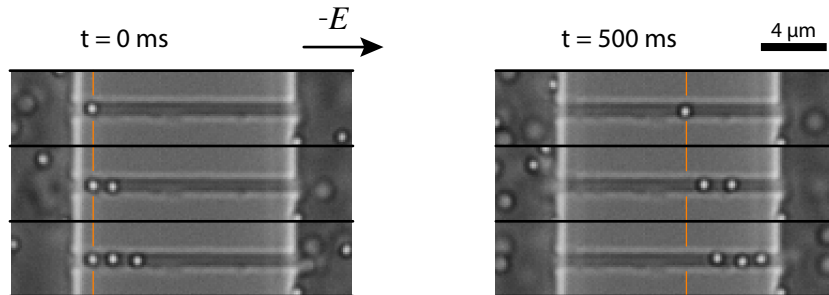


Figure 5.11: Electrophoresis of multiple particles. First column shows images with the leftmost particles aligned. Then the right column shows images taken after 500 ms. The negatively charged particles migrate left driven by the electric field. The migration velocity increases with the number of particles in the channel, suggesting the presence of the constructive interaction.

We hypothesise that particle interactions can contribute to the migration velocity. For a visual demonstration, Figure 5.11 shows electrophoretic migration through a channel filled with $N = 1$, $N = 2$, and $N = 3$ particles. On the left side, the leftmost particles are aligned next to the left channel entrance. Meanwhile, the right side shows their progress after half a second. Three particles travelled further than two particles, and two particles travelled further than one, suggesting that there is a positive interaction between the particles. The speed-up amount is proportional to the number of particles in the channel.

We quantify these results by analysing the trajectories as it was described in Section 5.1.3. This time, we select the time frames with a desired number of particles. However, we omit the frames where any two particles were closer than $1.2 \mu\text{m}$, because we want to understand large separation hydrodynamic interactions. This distance is motivated by Figure 4.3, which suggests that close range interactions disappear within $1 \mu\text{m}$.

Figure 5.12 shows the average velocity as a function of the particle number. The velocities are normalised by the $N = 1$ case, which permits an easy comparison between the datasets. Experimental data for all three driving sources are shown. In all these cases, the velocity, v_N

²Some of the early experiments were performed together with Antony J. Scott, who joined the lab for a Part 3 project.

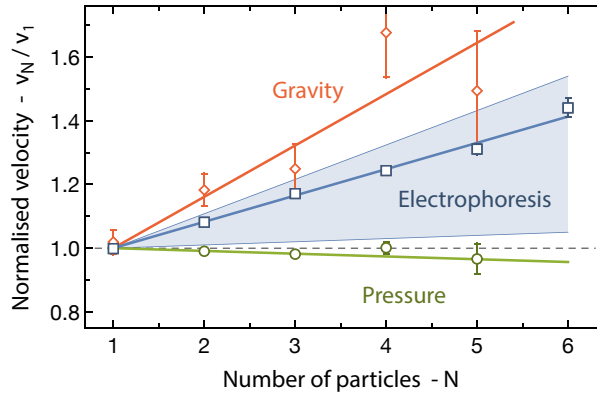


Figure 5.12: Velocity as function of number of particles inside the channel. Three modes of transport are shown: \square – electric field driven; \circ – pressure driven; \diamond – gravity driven. All the experiments were performed in $L = 13\mu\text{m}$ long channels (B4-13um-2; pH 6, 5 mM KCl; 1 mM FF). The gradient of electrophoretically driven particles depends on the pH and the salt concentration, where the blue region highlights the range of values that we measured. The driving force determines the type of interaction: pressure driven particles slow each other down, while gravity and electrophoretically driven particles interact constructively.

is linearly proportional to the number of particles, and therefore, we define an *enhancement coefficient*:

$$\text{En} \equiv \frac{v_N - v_1}{v_1(N-1)} \approx \frac{v_2}{v_1} - 1, \quad (5.2)$$

where v_N is the average velocity when there are N particles in a given channel. We now discuss the experimental results for each driving force.

Pressure driven particles have an almost constant velocity, where the enhancement coefficient is $\text{En} = -0.87\% \pm 0.20\%$. This value fluctuated between experiments, but always stayed negative and small. It suggests that pressure driven particles do not experience any significant interactions. We will explain this absence of interactions with a simulation in Section 5.3.1.

Electrophoretically driven particles speed-up with the particle number, suggesting the presence of long-ranged interactions. The enhancement coefficient for data that is shown in Figure 5.12 is $\text{En} = 8.27\% \pm 0.25\%$. However, we discovered that the coefficient depends on the composition of the liquid solution. The measured values were in the range from 1.0% to 10.7%, which is highlighted as the blue region. We will examine this dependence on the salt concentration and the pH in Section 5.2.1 and also, propose a model for interaction in Section 5.3.3.

Gravity driven particles have the largest speed-up, despite their smaller size. The enhancement coefficient is $\text{En} = 16.1\% \pm 3.8\%$. Please note that we had to combine multiple datasets to produce this plot, because the experiments had low trajectory numbers with high uncertainties.

All these data sets were taken on the same day and with the same chip. We will present an interaction model that explains this high enhancement in Section 5.3.2.

All in all, our measurements show a strong constructive interaction between particles transported in channels by electric fields or gravity. In contrast, particles driven by pressure flow show no interactions. These interactions are long ranged and are closely related to the nondecaying interactions described in Chapter 4.

5.2.1 Electrophoresis: enhancement coef. versus c_0 and pH

The enhancement coefficient for the electrophoretic migration varies with salt concentration and pH. This is not too surprising, since the electrophoretic velocity depends on both. Specifically, an increasing pH makes surfaces more electronegative [130, 131], thus increasing electroosmotic flow, as shown in Figure 5.8b. Here, we experimentally investigate how the enhancement coefficient depends on salt concentration and pH. Our aim is to measure qualitative trends that can be compared with the interaction model in Section 5.3.3, while avoiding the complexities of parametric studies.

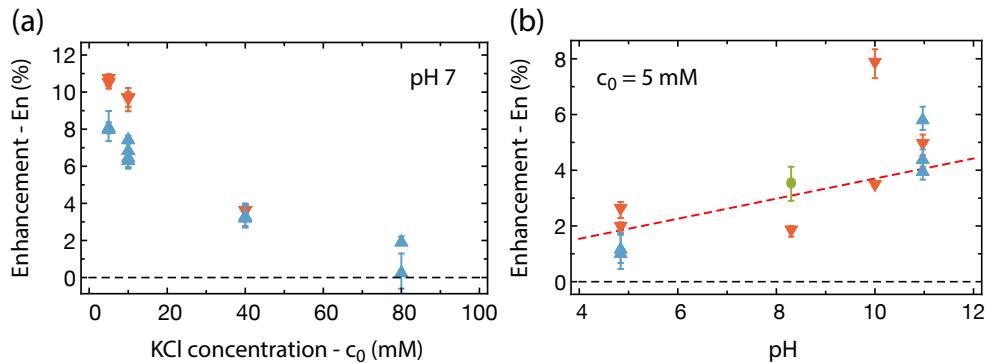


Figure 5.13: Enhancement coefficient dependence on the composition of the solution. The markers indicate different channels on the same chip: \blacktriangledown for channel 2; \bullet for channel 4; \blacktriangle for channel 5. In both experiments, B4-13 μ m chips were repeatedly flushed with new solution containing different salt concentration or different pH. In all cases, the solutions contain 1 mM Potassium Ferri/Ferrocyanide. The pH was controlled by adding KOH or HCl in micro-molar amounts. See Section 5.1.2 for more details. The lack of buffering agent accounts for strong drift, that is partially responsible for variation between experiments. (a) Enhancement as a function of salt concentration. In this experiment, the coverslip was coated with a thin layer of PDMS to reduce sticking [123]. (b) Enhancement as a function of pH. The dashed red line is a weighted linear fit, which highlights that the enhancement coefficient increases with the pH. The fit gives $En(pH) = 0.096 + 0.360 pH$.

Figure 5.13a suggests that the enhancement coefficient decreases with the salt concentration, where the shape reassembles hyperbola or exponential decay. These results should be interpreted

carefully, because the salt concentration increases the polystyrene particle charge density, as it was discussed in Section 5.1.2.

Figure 5.13b shows that the enhancement coefficient increases with the pH. The large variation around the line is due to three factors: (1) drift in time, because no buffer was used; (2) relatively low trajectory count, because we limited the duration of each experiment to measure all the data points in the same run; (3) the different channels had slightly different confinement ratios.

5.3 Model for driven particle interactions

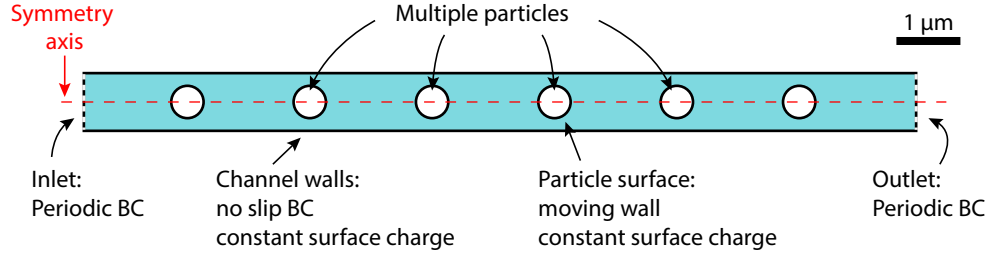


Figure 5.14: Simulation geometry for many particle electrophoresis. Two coupled equations were solved: the Stokes equation for flows and the Debye-Huckel equation for ion distribution.

Here, we present an interaction model that explains the experimental data for driven particles. All these models are based on a generalised interaction model for Brownian particles that was presented in Section 4.3.1. The geometry is shown in Figure 5.14, where we modify the boundary conditions to reflect the physics for different driving sources. Crucially, the inlets always have periodic boundary conditions with an added access resistance. This boundary condition permits flows into the reservoirs, which are necessary for the piston-like hydrodynamic interactions; just like the nondecaying hydrodynamic interactions in Chapter 4.

5.3.1 No interactions under pressure

Pressure difference induces Poiseuille flow in a channel, as given by Equation (2.17). This flow carries the particles, thereby inducing transport through the channel. We expect no nondecaying interactions, because the particles do not propel the medium, but merely respond to the medium's motion.

In COMSOL, we ran two simulations to find v_N and then another one to verify our solution. In the first simulation, we added an external pressure difference, Δp , to the periodic boundary condition on the inlets. This induces a Poiseuille flow inside the channel. Then, we computed the drag force exerted on the fixed particles by the moving liquid ($F_{\Delta p}$). With the second simulation, we accounted for particle motion by imposing an instantaneous velocity on all the particles. Here, $\Delta p = 0$. From the solution, we obtain the particle hydrodynamic friction coefficients. Then the response velocity is $v_N = F_{\Delta p}/\zeta$. Finally, we checked the solution by imposing the Δp and v_N and verifying that the net force on each particle is zero.

Figure 5.15a shows simulation results alongside the experimental data. The simulation reproduces the small velocity decrease with the particle number that we observed in the experiments. Both the simulation and experiment show that the decrease is linear with the particle number. But the simulation underestimates the coefficient at $En = -0.37\%$, while the

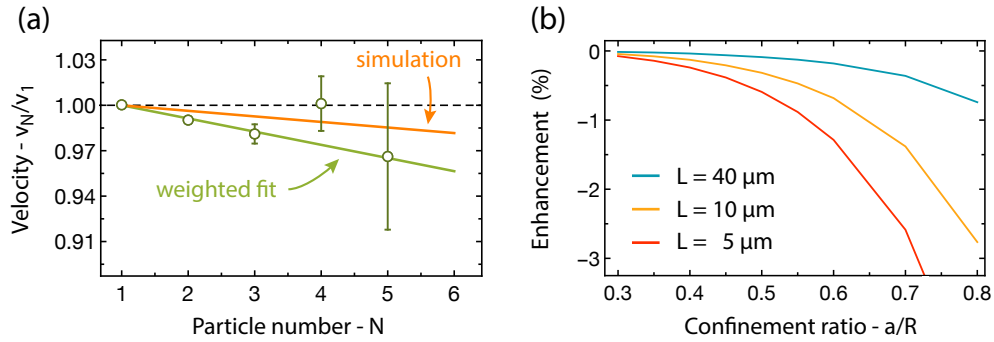


Figure 5.15: Simulation of particle interactions under pressure driven flow. (a) Normalised particle velocity as a function of particle number. Note that the vertical scale changed. The orange line shows simulation prediction with parameters matching the experimental geometry: $a/R = 0.55$ and $L = 13 \mu\text{m}$. The data points show experimentally measured values, where the green line corresponds to a weighted fit. (b) Simulated enhancement ratio as a function of confinement ratio. Simulations suggest that particles do not interact, but rather weakly obstruct motion.

average experimental value is $En = -1.18\%$ with standard deviation of $\sigma(En) = -0.52\%$. These values are small and the discrepancy between them can be attributed to the approximations made in our model – see Section 3.4.2. Importantly, the model suggests that the pressure driven particles have no constructive interactions, because they respond to fluid motion and do not drive it.

Using the simulation, we investigate how the geometry affects the enhancement coefficient. Figure 5.15b shows that the coefficient is always negative for the pressure driven migration. The slowing down is greatest for short and narrow channels, while it is negligible for wide channels. To understand the slowdown, consider that Poiseuille flow has a distinct parabolic flow profile. Large particles distort this optimum flow, and thereby, they produce a small pressure drop.

5.3.2 Hydrodynamic interactions under gravity fall

Unlike pressure, gravity exerts a force on the particle which then pushes the surrounding liquid. This is fundamentally different, since the particle acts like a piston and thus induces the particle-particle interactions. These interactions are closely related to the nondecaying interactions described in Chapter 4.

In COMSOL, to model the gravitational fall experiment, all particles were set to move at a constant velocity. The solution gives a collective hydrodynamic friction coefficient, from which we estimated the particle velocity as $v = F_g/\zeta$. This is essentially the same simulation as for two interacting Brownian particles, which was discussed in Section 4.3.1.

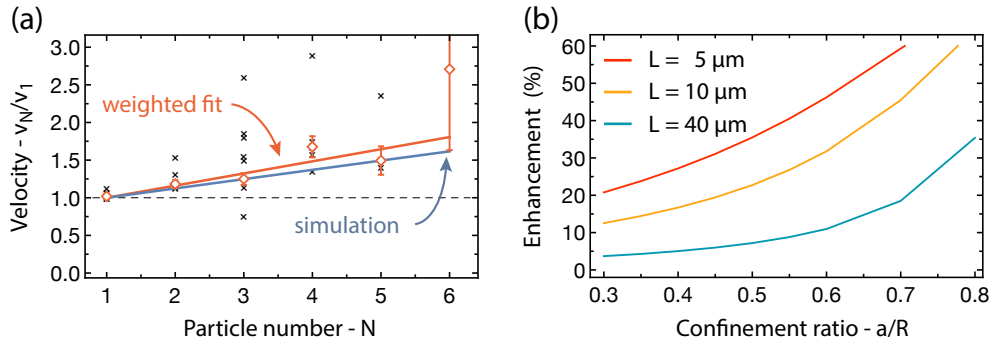


Figure 5.16: Simulation of particle interactions under gravity. (a) Normalised particle velocity as a function of particle number. The blue line shows the simulation prediction with parameters matching the experiment: $2a = 400\text{nm}$, $a/R = 0.44$ and $L = 13\mu\text{m}$. The black “x” show experimental values measured in 7 experiments, each with a low trajectory count. They were averaged to produce the red data points that have smaller errors. The red line shows a weighted fit with a slope of 16.1% per particle. Meanwhile, the simulation slope is 12.4% per particle. (b) Simulated enhancement ratio as a function of confinement ratio. The simulation values are the same as correlation coefficient predictions in Figure 4.8a.

Figure 5.16a shows simulation results together with the experimental data. Please note that the particle diameter was set to $2a = 400\text{nm}$, which corresponds to gold nanoparticles used in the experiments. The simulation predicts a linear velocity increase with the particle number, with an enhancement coefficient of $E_n = 12.4\%$, while the fit to the experimental data gives $E_n = 16.1\% \pm 3.8\%$. Our model agrees with the experimental data within the error bars, suggesting that our model captures the physics of interacting particles: the falling particles induce a Poiseuille flow that mediates the particle-particle interactions.

Figure 5.16b shows predictions for enhancement coefficients for different confinement ratios and channel lengths. These simulations match the predictions for the correlation coefficients, shown in Figure 4.8a. To test this similarity, we measured the correlation coefficient between two gold nanoparticles to be $\rho = 0.085 \pm 0.034$, which is below the simulation prediction of $\rho = 0.124$. Remember that our simulations have a tendency to overestimate the correlation coefficients slightly, as shown in Figure 4.9. These results suggest that interactions for gravity driven particles are slightly stronger than interactions between Brownian particles, but further experiments are necessary to reduce the statistical uncertainty in our observations.

All in all, our model captures the interaction strength well without any fitting parameters. It also reproduces the linear speed-up with the number of particles. All this suggests that the observed particle interaction is due to the nondecaying hydrodynamic interactions that we observed in Chapter 4.

5.3.3 Electrophoresis: competition between piston and backflow

In this section, we present an interaction model for particles driven by electric fields. This is the most complex case, since it comprises two independent components: electrophoresis of the particles and electroosmotic plug flow in the channel. We start our discussion with electrophoresis, assuming that electroosmosis in the channel is zero, $u_w = 0$. We will return to analyse effects of electroosmotic plug flow later.

As we have discussed in Section 2.3, electrophoresis has three force components: (1) electrostatic force forwards; (2) hydrodynamic drag due to induced electroosmosis around it, which we call backflow³; (3) and Stokes drag. We solve for each component independently and then superimpose the solutions to get the final result.

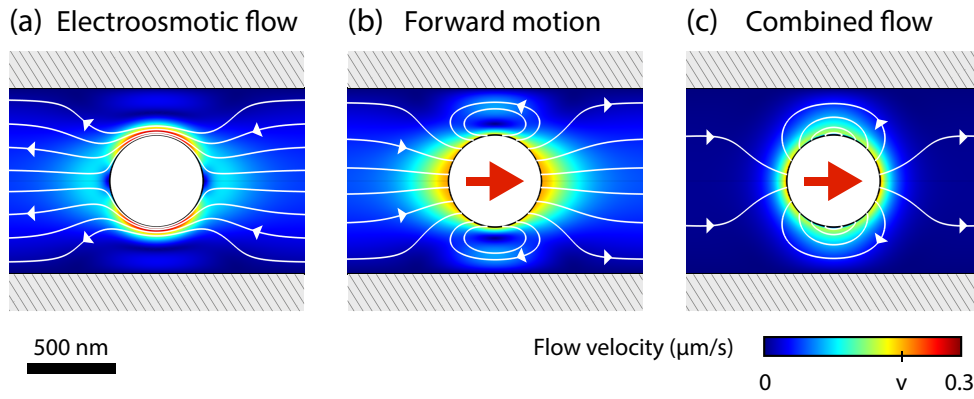


Figure 5.17: Flow profile around a moving particle under electrophoresis. (a) Electroosmotic flow induced around a stationary particle. The particle has surface charge density of $\sigma_p = 0.1 \text{ mC/m}^2$, while the solution has salt concentration of $c_0 = 6 \text{ mM}$, and the external electric field is $E_0 = 1000 \text{ V m}^{-1}$. The flow develops in a thin layer around the particle where the diffuse layer propels the liquid. The channel constraints this flow and reshapes it into a Poiseuille backflow. (b) Particle moving to the right with a velocity $v = 0.214 \text{ } \mu\text{m/s}$. Just like in the Brownian motion simulations, some of the flow curls around the particle, while other creates the Poiseuille flow forwards. (c) Combined flow profiles give the final solution. The Poiseuille backflow cancels most of the Poiseuille flow forwards, thus reducing the hydrodynamic interaction strength. This cancellation is not exact, leaving a weaker Poiseuille flow that carries the long-range interaction.

In COMSOL, we used the geometry shown in Figure 5.14. The electrostatic force is a surface integral of the surface charge, σ_p , times the electric field, $\mathbf{E} = \hat{\mathbf{z}}E_0 = \text{const}$, leading to $F_{pull} = -E_0 4\pi a^2 \sigma_p$. To calculate the electroosmotic backflow, we first estimate the charge distribution in the liquid using the Debye-Huckel equation – Equation (2.22). It is implemented

³We use the name backflow to distinguish from the electroosmosis induced in the channel. The name was chosen to reflect the direction: it is opposite to the particle's migration direction.

using Poisson's equation module with Neumann (flux) boundary conditions on the particle set to $-\sigma_p/\epsilon$. We also checked that the Poisson-Boltzmann equation produces equivalent results for relevant values of σ_p . In the external electric field, these charges migrate and induce electroosmotic backflow. Therefore, we added a laminar flow module with *volume force* set to $-\rho_C(\psi)E_0\hat{z}$. Figure 5.17a shows the resulting flow profile of electroosmotic backflow. Notice that the liquid accelerates in the thin diffuse layer around the particle. The resulting viscous drag is in the opposite direction to the electrostatic pull.

Next, the drag is estimated in a separate laminar flow module. All particles are set to move at a constant velocity and the resulting drag is estimated. This gives the hydrodynamic friction coefficient, allowing to estimate the terminal velocity using $v_N = (F_{pull} - F_{eo})/\zeta$. Figure 5.17b shows the flow profile caused by the particle motion. The flow is the same as in the Brownian motion simulations, where the moving particle induces a Poiseuille flow in the channel that would normally carry the interaction. However, in this case, the two solutions have to be superimposed to get the final result. Figure 5.17c shows the combined flow profile, where the electroosmotic backflow cancels most of the Poiseuille flow forwards. This reduces the interaction strength, thus explaining why the measured enhancement coefficients are smaller than the correlation coefficients for the same channel.

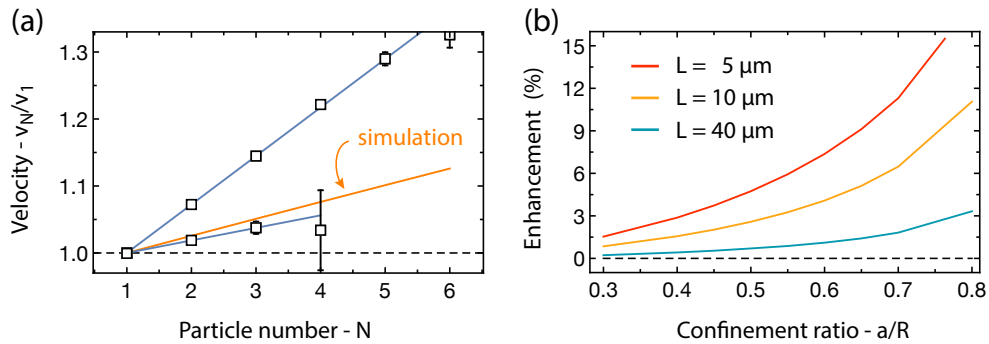


Figure 5.18: Simulation of particle interactions when driven by electrophoresis. (a) Normalised particle velocity as a function of particle number. The orange line shows simulation prediction with parameters matching the experiments: $2a = 500\text{nm}$, $a/R = 0.55$ and $L = 13\mu\text{m}$. The black squares show experimental values for two different experiments: the lower one illustrates that simulation can overestimate the interaction, but in most experiments the measured interaction was higher than the simulation prediction. The blue lines are weighted fits with slopes $En = 1.9\%$ and $En = 7.8\%$. Meanwhile, the simulations slope is $En = 2.6\%$. (b) Simulated enhancement ratio as a function of confinement ratio. The simulation values are smaller than the correlation coefficients, because the electroosmotic backflow reduces the interaction strength.

Figure 5.18a shows that the predicted velocity grows linearly with the particle number. This is consistent with the experimental observations and also follows the trend seen in previous models. The black points indicate experimental values, which were mostly higher

than the predicted enhancement coefficient, because the current simulation does not account for electroosmotic flow in the channel. Figure 5.18b shows the predicted enhancement coefficients for different channel geometries. The interaction strength decreases with channel width and length. Overall, the curves are similar in shape to gravitational fall (Figure 5.18b) and Brownian motion (Figure 4.8a), but have a smaller magnitude.

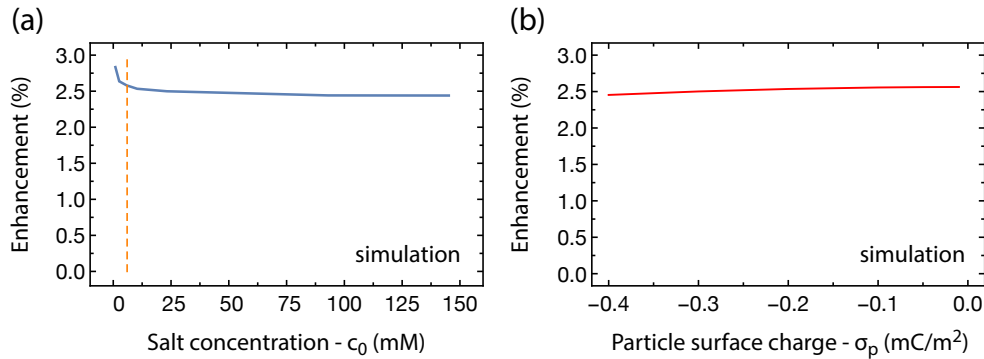


Figure 5.19: Simulation of the enhancement coefficients for different liquid solutions. In this model there is no electroosmotic flow on the channel walls. The geometry matches the experiments: $2a = 500$ nm, $a/R = 0.55$ and $L = 13$ μ m. (a) Enhancement coefficients as a function of salt concentration. It is almost constant above $c_0 = 6$ mM, which is marked as a dashed line. Below this concentration the enhancement coefficient increases. (b) Enhancement coefficients as a function of surface charge on the particle. It is constant within the numerical accuracy. The surface charge depends on the pH of the solution, suggesting that the enhancement coefficient should not vary with the pH.

Figure 5.19a shows the predicted enhancement coefficient dependence in salt concentration. Notice that the enhancement coefficient is constant at higher salt concentrations, and increases for $c_0 < 6$ mM. However, this increase has different shape to the experimentally observed curve in Figure 5.13a, suggesting that other effects could be contributing to the experimentally observed variation with c_0 . In this simulation, the increase at low salt concentrations originates from the increasing Debye length, because it determines the magnitude of the electroosmotic backflow. The weaker backflow cancels less of the constructive piston interaction, thus resulting in the increased enhancement coefficient.

Meanwhile, Figure 5.19b shows that the enhancement coefficient is constant for different surface charge densities of the particles (within simulation accuracy). This is not surprising, since the enhancement coefficient is a ratio between velocities, thereby eliminating direct dependence. However, the experimental values for the enhancement coefficient increase with the pH, which is proportional to the surface charge density [130, 131]. Furthermore, the predicted enhancement coefficients are considerably smaller than values measured in the

experiments. These discrepancies suggest that our model is incomplete, and therefore, we include the electroosmotic plug flow that develops due to charge on the channel walls.

With electroosmotic plug flow in the channel

The channel walls have a surface charge that creates an electroosmotic flow with a plug flow profile that was discussed in Section 2.3.4. This is different from the electroosmotic flow around the particles, which we call the electroosmotic backflow. In our experiments, the charge was always negative, resulting in electroosmotic flow in an opposite direction to the electrophoretic migration. This slows down the particle, as it was shown in Figure 5.8b. To understand the effect on the particle-particle interactions, consider a plug flow that has velocity, u_w , given by the Helmholtz-Smoluchowski slip velocity, see Equation (2.24). The velocity of the particle is then $v'_N = v_N - u_w$, where v_N is the electrophoretic migration velocity in a channel with no electroosmotic plug flow. The prime in v'_N indicates that we are including electroosmosis. The enhancement coefficient now reads

$$\begin{aligned} \text{En} &= \frac{v'_2}{v'_1} - 1 = \frac{v_2 - u_w}{v_1 - u_w} - 1 \\ &= \frac{\Delta v + v_1 - u_w}{v_1 - u_w} - 1 = \frac{\Delta v}{v_1 - u_w}, \end{aligned} \quad (5.3)$$

where $\Delta v = v_2 - v_1$ is the velocity gain due to particle interaction. This equation suggests that the enhancement coefficient increases with an increasing electroosmotic plug flow velocity. In other words, the plug flow reduces the migration velocity, but not the interaction strength. Thereby the interaction appears relatively stronger. This explains why the experimentally measured enhancement coefficients were larger than expected by our simulations – see Figure 5.18a.

Furthermore, to explain the salt concentration dependence, we consider the linear relationship $\Delta v \propto v_1$ that was observed in the simulations. We thus introduce quantity $\rho_{ep} \equiv \Delta v/v_1$. Combining it with Equation (5.3) gives

$$\text{En} = \rho_{ep} \left[1 + \frac{u_w}{v_1 - u_w} \right]. \quad (5.4)$$

This is a hyperbolic function with respect to the velocity, v_1 . From Section 5.1.4, we know that $v_1 \sim c_0$. Therefore, Equation (5.4) is a decaying function with the salt concentration. This model qualitatively explains the measured salt concentration dependence that was shown in Figure 5.13a.

A similar argument can be applied to the pH variation. However, that case can be analysed with simulations because only one parameter varied significantly with pH – surface charge density on the channel walls, σ_w .

In COMSOL, the electroosmotic flow is calculated directly by solving Equations (2.22) and (2.10). This is the same method used to calculate the electroosmosis around the particle, enabling us to compare the effects of salt concentration and charge density in the same way as in Figure 5.19. However, please note that equations are simplified models for describing the double layer. Previous experiments have demonstrated that surface potentials have non-trivial relations that depend on surface roughness, hydrophobicity, and ion types [45, 122, 132–134]. Our aim is to understand qualitatively the trends governing the particle interactions and thus, we study the simplified models.

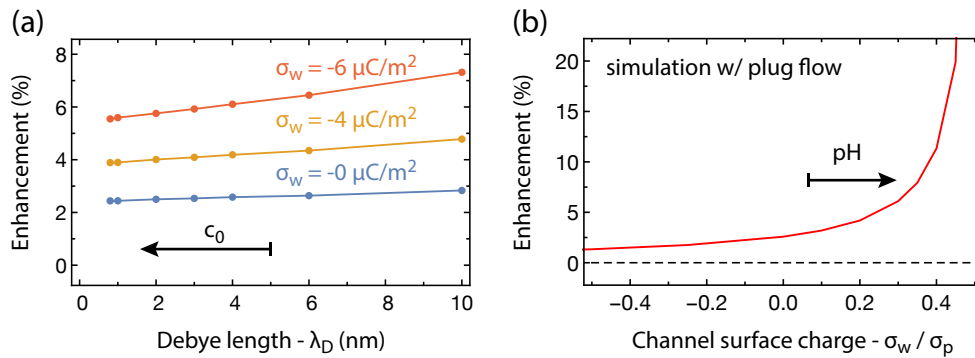


Figure 5.20: Simulation of the enhancement coefficients for different liquid solutions *with* the electroosmotic flow on the channel walls. The geometry matches the experiments: $2a = 500$ nm, $a/R = 0.55$ and $L = 13$ μ m. (a) Enhancement coefficients as a function of Debye length, which is inversely proportional to c_0 , as given by Equation (2.22). Lines correspond to three different wall charges, where the blue corresponds to no charge, as shown in Figure 5.19a. The black arrow indicates an approximate range and direction for experimental salt concentrations. (b) Enhancement coefficients as a function of surface charge on the channel walls. The charge on the particle was $\sigma_p = -20$ μ C/m². The black arrow indicates an approximate range and direction for experimental pH values. The enhancement coefficient increases with surface charge on the channel walls.

Figure 5.20a shows the enhancement coefficient dependence on the Debye length, which is inversely proportional to the salt concentration. Note that in this simulation particles have fixed surface charge density. The predicted variation is small, just like in the case with no electroosmotic plug flow. A much stronger variation is observed when we vary the surface charge density on the channel walls, as shown in Figure 5.20b. Here, the enhancement coefficient increases with the surface charge, because the u_w is proportional to the surface charge on channel walls. This confirms the relation presented by Equation (5.3). The black arrow indicates approximate values for the surface charge from the literature [122]. In that

range, the Enhancement coefficient increases by 3%, which is close to the experimentally observed increase of 2%. However, most importantly our model reproduces the experimental trends seen in Figure 5.13b.

To summarise, our interaction model suggests that hydrodynamic interactions are much weaker than in the Brownian motion case, because the electroosmotic backflow cancels much of the piston effect. On the other hand, the electroosmotic plug flow slows down the particles, but does not affect the interaction magnitude, thus increasing the enhancement coefficient. This allows controlling the enhancement coefficient by adjusting the pH of the solution. Further experiments are necessary to understand quantitatively how the enhancement coefficients depend on the salt concentration. In addition, our model suggests that the enhancement coefficients are sensitive to changes of the double layer around the particle. This might be a useful tool for identifying particles or measuring their surface properties, such as roughness.

5.4 Conclusion and impact

We investigated how the nondecaying hydrodynamic interactions affect driven transport. For this, we used three different forces to drive particles through channels: hydrodynamic pressure, electric fields, and gravity. Each showed a distinct behaviour that agrees with our hydrodynamic interaction model. For pressure driven particles, there was no interaction, but rather a small pressure blockade that decreases the migration velocity with the number of particles in a channel. This result demonstrates that particles must push the liquid to cause the nondecaying hydrodynamic interaction. For comparison, particles driven by gravitational pull showed a strong constructive interaction that results in linearly increasing migration velocity with the number of particles in a channel. Our model predicts that the interaction strength is numerically equal to the correlation coefficients, but the measurements suggest that it is slightly stronger. On the other hand, the electrophoretically migrating particles experience much weaker interactions, because the electroosmosis on the particle's surface induces a backflow that cancels much of the interaction. Furthermore, we showed that magnitude of this effect could be controlled by adjusting the surface charge densities. In all cases, the behaviour follows the predictions from our hydrodynamic interaction model which has periodic boundary conditions set on the inlets of the channel. This suggests that interactions observed in this chapter are hydrodynamic in nature and are closely related to the nondecaying interactions between Brownian particles.

Our findings have far-reaching implications that we discuss in the remainder of this section. Firstly, we saw that particles migrate faster at higher densities. This might affect biological protein channels where membrane potential can drive particle transport [1]. The effect is not limited to narrow channels and should persist for wide channels as well. In such case, the

contribution of each particle decreases, but the channel may fit in many more particles, where each contributes a small velocity enhancement. For example, consider a channel of $L = 40\mu\text{m}$ and $2R = 5\mu\text{m}$ filled with particles of diameter $2a = 500\text{nm}$. We expect the enhancement to be small at $\text{En} = 0.1\%$, but we can potentially fit a thousand particles that would give a velocity increase of 100%. This prediction is yet to be measured experimentally.

Another interesting consequence is for interconnected channels, where short channels are forming a network. An example of such network could be gels used for gel electrophoresis. In this case, our findings might affect the distribution of particles in the gel, since we predict that particle clusters travel faster than isolated particles. This allows the clusters to catch up with the isolated particles that are ahead. Therefore, the particle distribution should have a sharp front and a tail at the back. This could be particularly useful for gel electrophoresis, because it creates clear bands. However, further studies are necessary to see if this process happens in a polymer meshes that form gels.

5.4.1 Electrophoresis vs pressure

Our discovery also may enable novel designs for filtration devices or dosage control. For example, suppose that there is a pressure flow in an opposite direction to the electrophoresis and it is slightly stronger than the electrophoresis. Such flow stops single particles from translocating through the channel, but multiple particles can pass, because the velocity of two particles is higher due to the enhancement.

Experimentally, we setup an electric field and then increased the pressure until isolated particles stop moving through the channel. This state is shown in Figure 5.21a. Over time particles accumulated around the mouth of the channel, as shown in Figure 5.21b, until two or more particles accidentally entered the channel. Their net velocity is greater which leads to electrophoretic migration, as shown in Figure 5.21c. This allows transport, but only when there are enough particles in the channel. One possible application for such phenomena is a density selective filter⁴.

⁴This observation also explains behaviour seen by Timothee Menais, who performed early electrophoresis experiments and saw clustering at the channel mouth.

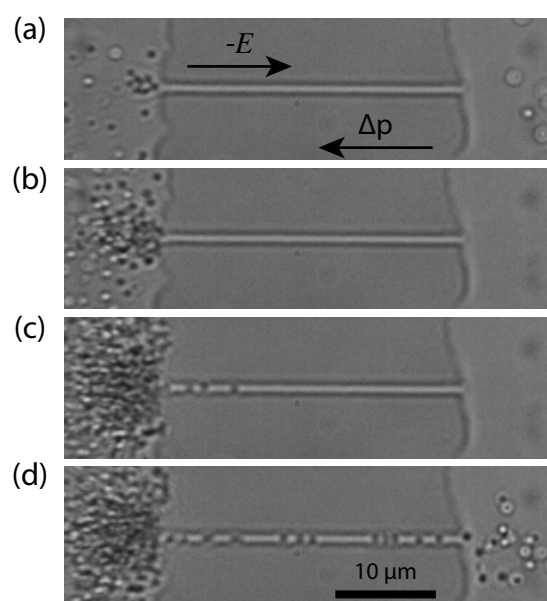


Figure 5.21: Competition between electrophoresis and pressure. The electric field drives particles to the right, while pressure drives them to the left. (a) The system was balanced so that a single particle cannot move to the right; (b) this leads to particle accumulation on the left side of the barrier. (c) At some point multiple particles enter the channel, where their combined velocity is greater than the pressure driven flow; (d) this leads to a rapid transport of particles through the channel. Importantly, the accumulation of particles must happen before particles can enter the channel.

Summary and Outlook

Throughout this thesis, we studied hydrodynamic interactions inside narrow channels. Our experiments imaged colloidal particles that move inside a microfluidic chip containing micron-sized channels. From the particle trajectories, we were able to infer particle-channel and particle-particle interactions, which are mediated by the liquid. To our surprise, we discovered that moving particles act like pistons, inducing a Poiseuille flow along the whole channel. This has never been observed before, thus raising new questions about particle behaviour inside narrow channels with a finite length.

First, we found that particles have higher diffusion coefficients than previously predicted, which also depend on the channel length (Figure 3.26). Secondly, we have discovered that the interaction between Brownian particles is distance-independent (Figure 4.3). This nondecaying interaction acts on all particles inside the same channel, which challenges the previous models that only considered local interactions. Finally, we have shown that this interaction holds for electrophoretically and gravitationally driven transport, leading to an enhanced migration velocity. In contrast, particles driven by the pressure gradient have no interactions (Figure 5.12).

We also have developed a numerical model for predicting the hydrodynamics inside channels. Crucially, it has periodic boundary conditions set on the inlets of a channel, which capture the flows across the boundaries quantitatively. This model reproduced all the experimental data with high accuracy and without any fitting parameters, suggesting that our interpretations are correct. Our discoveries have a broad range of implications for transport phenomena across many different length-scales.

Our study also raises new questions about the hydrodynamic effects in micro- and nano-systems. For example, are these interactions exploited by biological protein channels? Do they even exist at those length-scales? The latter question can be answered by investigating the nature of the periodic boundary condition found in our model. It captures the high pressure resistance of narrow channels that dominates the flows, thereby producing accurate predictions. However, there must be an underlying mechanism that permits the flows into reservoirs. Future research should investigate this mechanism, because it will reveal the necessary conditions for these phenomena, and it will advance our fundamental understanding of liquids in confinement.

In addition, we foresee practical applications for particle interactions during electrophoretic transport. Our model suggests that interaction strength is sensitive to surface properties of the particles. This might allow probing the surface roughness and the charge distribution of biomolecule, which also can be employed as a non-chemical way for identifying them. Other applications might utilise the observed interactions to filter particles or to cluster them together. These are just a few examples and we are certain that the best ideas are yet to come.

All in all, we have discovered a new particle interaction in channels, which illuminates the role of hydrodynamics in the transport phenomena, but it also raises many more questions. We leave you with the words of Winston Churchill:

“Every day you may make progress. Every step may be fruitful. Yet there will stretch out before you an ever-lengthening, ever-ascending, ever-improving path. You know you will never get to the end of the journey. But this, so far from discouraging, only adds to the joy and glory of the climb.”

Appendix A

Entrance jamming in electric field

Electrophoretically driven particles occasionally jammed at the entrances of channels (method described in Section 5.1.2). For example, a typical electrophoresis experiment is shown in Figure A.1a. Here, the electric field direction is kept fixed, which slowly increases the particle density on the left reservoir. As a result, more particles translocate through the channels and occasionally they jam, thus blocking the channel. In Figure A.1b, channels 1, 3, 4, and 5 have recently jammed. The formation of clusters on the left side indicates that the electric current flows through the structure. In fact, these structures keep growing and create large structures, as shown in Figure A.1c. The image is focused on the glass cover slip, but the structure extends into \hat{z} direction as well. The inset shows a Fourier transform of the image, which suggests a hexagonal packing. The distance between particles is 521 ± 15 nm, which agreed well with theoretical expectation of $2a + 2\lambda_D \approx 520$ nm.

Empirically, we observe that the time to jamming is inversely proportional to initial particle density and also the applied potential. However, the exact relationship was not determined.

Two types of jamming events were observed. First, particles jammed by forming an arch around the channel's mouth, as shown in Figure A.2a. The arch forms a structure that seems to lock the particles outside the channel. In second type of events, two particles interlock inside the channel, as shown in Figure A.2b. This type was observed more frequently than the first type events. Notice that the fourth row shows a jamming that occurred further inside the channel. Such events were relatively rare and might be caused by a small tapering of that channel. In both cases, the mechanism of the particle jamming might be similar to the bulk jamming for soft particles [135], but further research is required.

Similar jamming transitions have been observed for pressure driven systems, but at much higher particle densities [136]. They report jamming at volume fractions of $\phi \approx 0.5$, which corresponds to about 800 particles/pL. This is an order of magnitude higher than our bulk concentrations. However, it is possible that around the channel inlet the particle density reaches

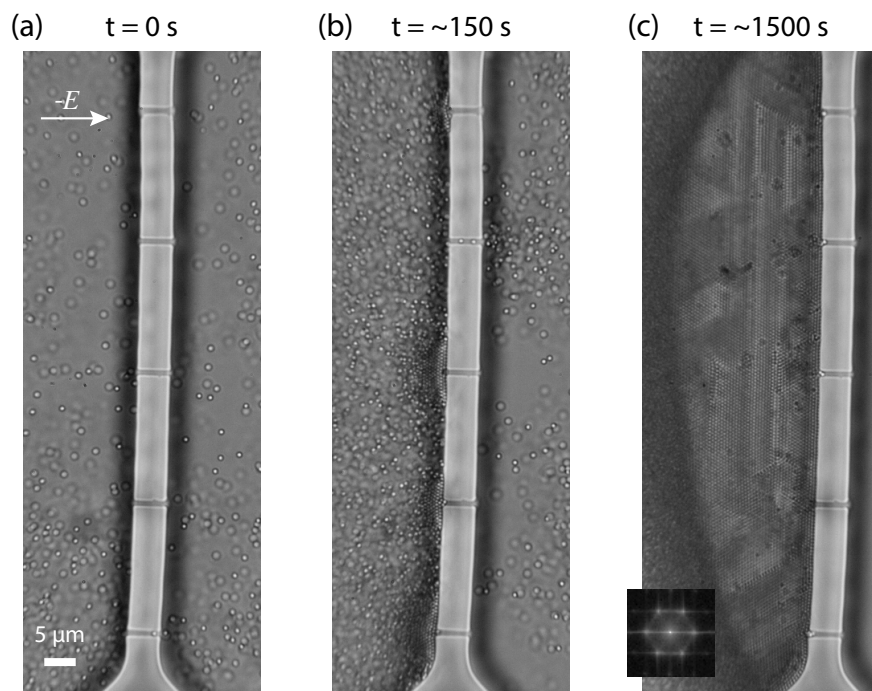


Figure A.1: Entrance jamming induced by electric fields. (a) Shows a snapshot of normal electrophoretic transport driven by a 500 mV potential. (b) Shows a transition to entrance jamming at four channels. The time when jamming starts varied between experiments. However, increasing particle density reduces the time necessary for the first jamming. (c) Once the channels are blocked, the crystal-like structure grows. The inset shows a discrete Fourier transform of the image, which reveals that the structure follows a dense hexagonal packing.

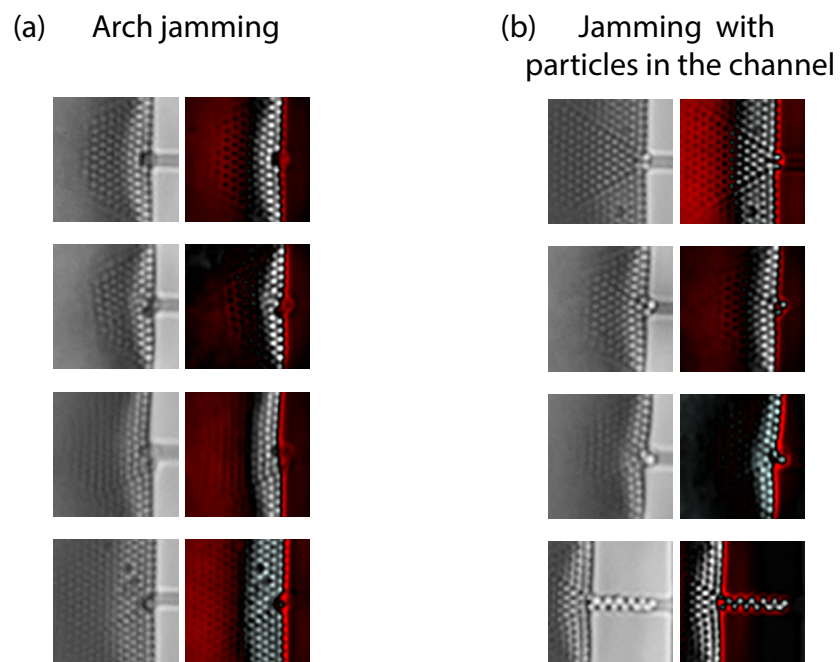


Figure A.2: Sample images for entrance jamming. The images on the left are median averages that eliminate moving particles. Meanwhile, in the corresponding images on the right, the background image has been subtracted to enhance contrast. (a) Row shows cases where colloids form an arch. There are no colloids in the channel. (b) row shows cases where jamming occurred with colloids inside the channel.

this density before the jamming occurs. As mentioned earlier, electric fields focus particles into the inlet and it increases the particle density over time.

Once the large crystal-like structure had formed, we observed a reversal of the migration direction inside the channel. For example, free particles on the right side of the barrier in the Figure A.1c moved to the left through the channels and joined the structure. This effect is surprising and likely caused by electric field reversal due to accumulation of charged colloids. However, this effect is a consequence of the large structure and not the cause, because the reversal does not happen when the structure is small.

We hypothesize that electrophoretic jamming may be used for self-healing materials. Suppose that we have a pipe with a small crack, where we induce particle jamming thus blocking further leaks. For example, consider lubrication liquid in an offshore drilling pipe. Pressure can induce jamming, but it requires the high density of particles [136] that might also block the desired flow inside the pipe. On the other hand, the electrophoretically induced jamming increases the local particle density, which then allows for jamming to occur. Therefore, much lower densities of colloids may be used to produce jamming, which then might block small cracks in the pipe.

Appendix B

More on experimental methods

B.1 E-beam lithography and Si etching protocol

This protocol was used to produce sub-micron wide channels for a mould. It was developed and performed by Vahe Tshitoyan.

Preparation: Clean the chip with acetone and IPA. Sonication seems to break the edges of the sample into small pieces which then damage the surface. Therefore, we avoided the ultrasound. If it still does not look clean enough, ash with Oxygen plasma at around 150 W for about a minute.

Add resist: $\sim 1\ \mu\text{m}$ PMMA A6 (spin coating at 1500-2000 rpm). It is good to check the thickness at least once, because it has to be at least $1\ \mu\text{m}$ for the lift-off to work later. Then Bake on a hotplate for 7 min at $180\ ^\circ\text{C}$.

E-beam: expose resist to electron beam. Performed by a technician at Cavendish Laboratory.

Development: 45 sec MIBK/IPA (25%/75%) + 2% Di water, after which rinse in IPA for at least 30 sec. After the development, do Oxygen plasma ashing for 10 sec to get rid of the residual resist. Don not keep it for more than 10 sec, because this makes the edges round and the lift-off will not work. Then bake for about 5 min at $110\ ^\circ\text{C}$ to get rid of the water, if there is any left.

Evaporation: Thermal evaporation of Cr/Au (25 nm/375 nm). Anything else should work too, as long as it is around 400 nm thick and sticks well. E.g. Ti instead of Cr should be fine.

Lift-off: Standard acetone lift off works well. Check afterwards if the structures are there. If they are not, then there must have been a problem with the e-beam or with the development, which made the edges too rounded and the evaporated layer was continuous.

Ashing and baking: 1 min of ashing and 10 min of baking to get rid of the residuals before loading it into the etcher.

Reactive ion etching: After the metallic wires are there, the Si needs to be selectively etched down. The rate of etching is system specific, so one has to try. We used $\text{CF}_4 + \text{SiCl}_4$ combined with Argon at 300 W, for 7 min, which seemed to give around 850 nm height and sharp edges. We believe the Cr/Au was being etched down around 2 times slower than Si, so after 7 min the whole metal was gone, and there were 850 nm high Si wires left.

B.2 PDMS/glass bonding quality

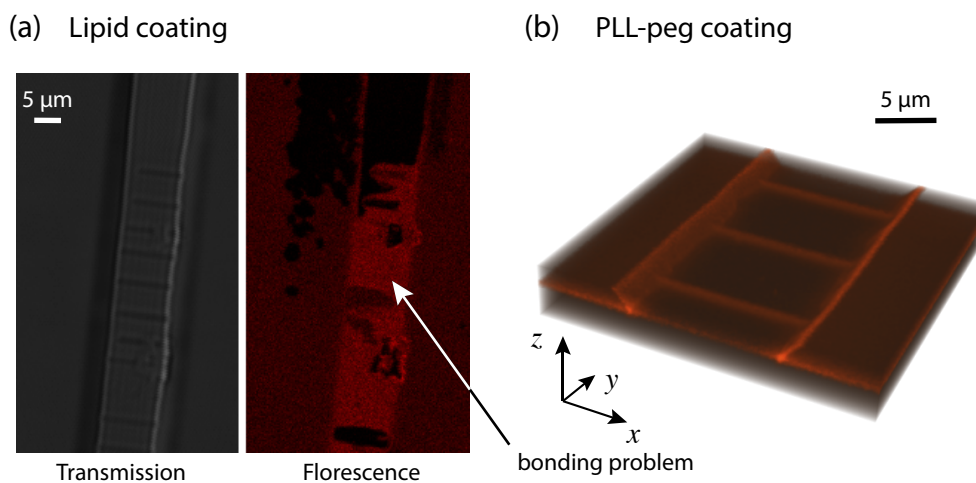


Figure B.1: Confocal microscopy images of fluorescent surface coatings. (a) Fluorescent lipid coating onto of microfluidic channels. Bright-filed images are very standard, but inspecting the florescence image reveals that lipids could get in between the PDMS and glass. Elsewhere in the chip there was no florescence in the bonded regions. This suggests that bonding failed in that part of the chip (S3-10um). (b) A 3D image of PLL-peg coating. The three bright lines in the middle are channels (chip B4-13um). The florescence intensity in between the channels is low, suggesting that the PDMS bonded well.

In some electrophoresis experiments, particles are driven towards the barrier. We suspected that this might be due to poor bonding between PDMS and glass, thereby leaving a thin gap between them. In such case, the gap would conduct the electricity and thus the charged particles would be attracted towards the gap. To test this idea, we coated interior of the chip with florescent lipids (protocol below), allowing us to identify all surfaces that water could reach. The coated chip was measured using a confocal microscope (Leica TCS SP5 II).

Figure B.1a shows a bright-field image alongside a florescence image. Red color indicates lipid location that are stuck to the surface. Notice that reservoirs have monotonous red color, which correspond to lipids on the glass surface. Meanwhile, the barrier has black regions and also bright red regions. The black regions have no florescence, suggesting that lipids could not

reach those locations and the PDMS has bonded to the glass. The bright red regions have twice the intensity of the reservoirs, suggesting that there are two surfaces there. This agrees with our idea of a thin gap between the PDMS and the glass. Such gap is only observed in S3-10um chip and is attributed to defects in the mould.

The protocol for coating the channels was developed together with Lorenzo Di Michele, who also supplied the florescent lipids. First, we bond the PDMS to the glass coverslip, as described in Section 3.1, and leave it in air for 30 minutes. Then the chip is placed back into plasma oven for 4 min to activate the surfaces. The chip is flushed with a solution containing lipid vesicles (diameter of ~ 200 nm), and afterwards it is flushed with a buffer (solution: 5 mM KCl, Tris buffer) to remove excess lipids. The same procedure works for PLL-peg coating, but it has a lower contrast, as shown in Figure B.1b.

B.3 Measuring D_x for migrating particles

Measuring the diffusion coefficient often relies on observing passive Brownian motion, but sometimes this is impractical or unachievable. For example, the resistive pulse sensing technique can size polymers moving through a channel [137–139], but cannot record passive motion. Here, we attempt to measure the diffusion coefficients from the trajectories of moving particles and compare them with our measurements for passive Brownian motion.

We modify the mean squared displacement function by subtracting the average velocity, which would otherwise dominate the function:

$$MSD^* \equiv \langle (\Delta x(\Delta t))^2 \rangle - \langle v \rangle^2 \Delta t^2 = \text{Var}[\Delta x(\Delta t)] \quad (\text{B.1})$$

where Var is the variance function. The last equality suggests that measuring the variance is equivalent to the mean squared displacement. We expect this function to have a linear term caused by the Brownian motion, $\propto 2D_x \Delta t$, and a quadratic term due to the intrinsic variability of the particles, $\propto W^2 \langle v \rangle^2 \Delta t^2$. Additional terms are also possible, but we restrict ourselves to these two and an offset term, thus giving us a polynomial equation:

$$\text{Var}[\Delta x] \approx A + 2D_x \Delta t + W^2 \langle v \rangle^2 \Delta t^2 \quad (\text{B.2})$$

Figure B.2a shows the variance function for driving potentials of 200 mV, 400 mV, and 0 mV. The latter experiment corresponds to passive diffusion, thereby providing the true diffusion coefficient in this channel, $D_x = 0.153 \mu\text{m}^2/\text{s}$. It allows to asses the quality of our estimates. The solid lines in the figure are fits to our phenomenological model given by Equation (B.2). The estimates for D_x are within 15% from the expected value. Figure B.2b

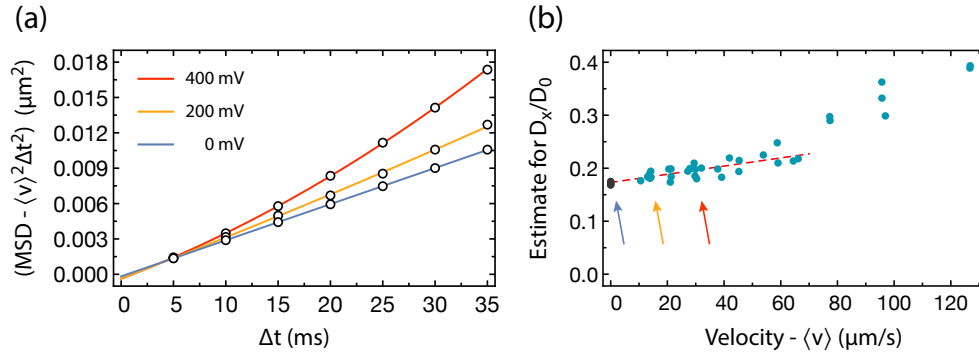


Figure B.2: Diffusion coefficient estimates from moving particle trajectories. (a) Mean squared displacement with subtracted average velocity as a function of time. Three driving potentials are shown, where 0 mV correspond to passive diffusion. The solid lines show fits to the function $f = A + 2D_x\Delta t + C'\Delta t^2$, where the parameters were: (0 mV) $A = -175 \text{ nm}^2$, $D_x = 0.153 \mu\text{m}^2/\text{s}$, $C = 0$; (200 mV) $A = -353 \mu\text{m}^2$, $D_x = 0.170 \mu\text{m}^2/\text{s}$, $C = 0.792 \mu\text{m}^2/\text{s}^2$; (400 mV) $A = -372 \text{ nm}^2$, $D_x = 0.169 \mu\text{m}^2/\text{s}$, $C = 4.8711 \mu\text{m}^2/\text{s}^2$. (b) Estimate for diffusion coefficient as a function of particle velocity. The D_x was estimated from the polynomial fit as shown in (a). The red line indicates a linear fit for data below $70 \mu\text{m/s}$, which allows to extrapolate the D_x at $\langle v \rangle = 0$. This gives accurate value for the diffusion coefficient.

shows D_x estimates from 33 other experiments, which suggest that the estimated D_x values increase with the particle velocity. This might be due to fitting errors or a second order effect that we did not account for (e.g. particle rotation). We obtain a better estimate of the diffusion coefficient by fitting a linear function and extrapolating the value at $\langle v \rangle = 0$. It gives $D_x = 0.152 \mu\text{m}^2/\text{s}$, which agrees with the passive Brownian motion measurement.

For the quadratic term, we performed a similar fit to our experimental data and obtained a value $W = 0.046 \pm 0.010$. As expected, this value is close to the previously measured variability of average velocities, shown in Figure 5.6. This agrees with our hypothesis that the quadratic term comes from variability in particle velocities.

All in all, our analysis suggests that fitting the simple quadratic polynomial equation to the $\text{Var}[\Delta x(\Delta t)]$ gives a reliable upper estimate for the diffusion coefficient. An accurate value can be obtained by measuring at multiple driving potentials and then extrapolating the value to zero potential.

B.3.1 Comparison to DNA polymer transport

We compare our particle transport through channels with polymer transport through conical nanopores. These experiments were developed and performed by Nicholas Bell [138, 139, 141]. Briefly, two reservoirs are connected with a conical nano-capillary with a tip diameter of 15 nm. The solution contains DNA molecules that were modified to have six evenly spaced

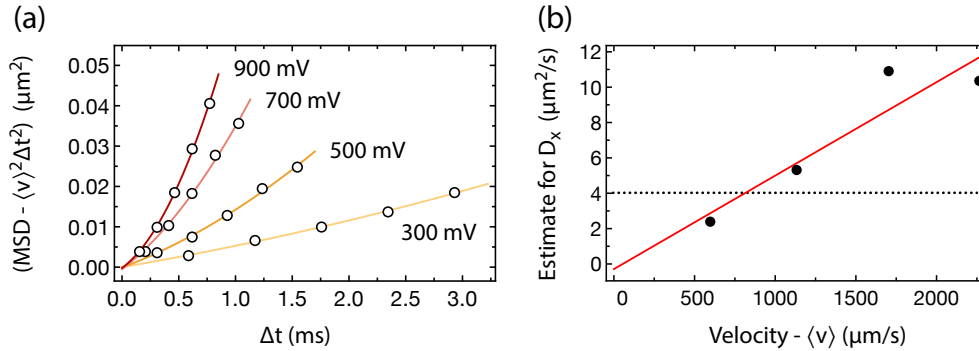


Figure B.3: DNA polymer transport through a nanopore. Experiments were performed by Nicholas Bell using a resistive pulse sensing method. The DNA molecule had evenly spaced markers along its length, allowing us to measure times when different segments pass the nanopore (DNA length is $\approx 2460\text{nm}$ and spacing between markers is $\approx 350\text{nm}$). (a) Mean squared displacement with subtracted average velocity as a function of time. We translated the data from time domain to space domain using the mean velocity. The solid lines are fits to Equation (B.2). (b) D_x coefficients from the polynomial fit in (a). Red line indicates a linear fit through the data: $-0.290 + 0.0053\langle v \rangle$. The D_x coefficients grow linearly with the polymer velocity, suggesting that D_x does not correspond to the diffusion coefficient of the polymer. For comparison, the dashed line shows literature value for the diffusion coefficient of a stretched DNA molecule [140].

markers. When an electric potential is applied the DNA moves through the nano-capillary and thus reduces current. This technique is known as the resistive pulse sensing. Crucially, the markers on the DNA block slightly larger current, thus allowing us to time their passage through the nano-capillary. These times are not sufficient to obtain the trajectory, but they do provide information about the velocity of the DNA at different segments.

From these times, we computed the MSD with subtracted mean velocities, as described in the previous section. Figure B.3a shows the result, where the solid lines are fits to our polynomial model given by Equation (B.2). These fits capture the data well, but a closer examination of the D_x coefficients reveals a linear dependence on the average velocity – see Figure B.3b. We saw such dependence with particle electrophoresis, where we found a correct diffusion coefficient by extrapolating the value at $\langle v \rangle = 0$. However, for polymers the extrapolation yields zero, suggesting that the process is dominated by a different process altogether. Therefore, our analysis suggests that the MSD of moving polymers cannot be used to estimate the diffusion coefficients.

B.4 Velocity auto-correlation function and motion blur

Cameras collect light over a finite interval called exposure time, δt_e . During this time, particles move around, and thus, the recorded image contains an averaged particle position. This effect is called motion blur and its impact is visible in the velocity auto-correlation function, defined by Equation (2.3). This function measures similarity between consecutive displacements of the particle, or in other words, how the velocity changes over time. We estimate velocity from trajectories using $v \equiv \Delta x / \Delta t = (x(t + \Delta t) - x(t)) / \Delta t$, where $x(t)$ is the position of the particle at time frame t .

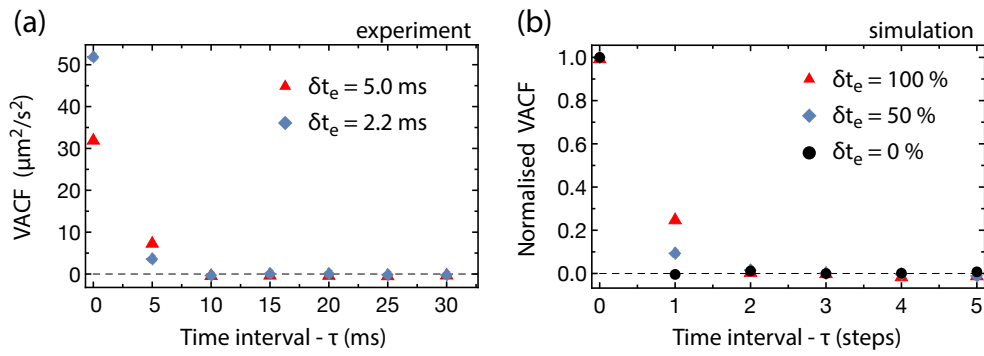


Figure B.4: Velocity auto-correlation function as a function of time interval between velocities. (a) Measurement in channels for a single particles. The two sets correspond to two different camera exposure times, while the interval between frames was kept at $\Delta t = 5$ ms. The auto-correlation of the second data point decreases with the exposure time. (b) Simulation of 1D random walk with motion blurring. There different simulated exposure times are shown: 100% - maximum exposure time; 50% - half exposure time; 0% - instantaneous snapshot. Simulation suggests that introducing motion blur increases anomalous auto-correlation, which does not exist in the underlying data.

For passive Brownian motion, VACF should be zero when $\Delta t \gg \tau_f \sim 10\mu\text{s}$ [30, 142]. However, Figure B.4a shows that in our measurements the first two points of VACF are non-zero. The first data point corresponds to $\tau = 0$: $\langle v(0)^2 \rangle = \langle \Delta x^2 \rangle / \Delta t^2 \approx D / \Delta t$, suggesting that the first point is intrinsic to Brownian motion. The second data points is above zero because of the motion blur artefact, which can be seen when varying the exposure time. Two exposure times are shown in the Figure B.4a: $\delta t_e = 5.0$ ms and $\delta t_e = 2.2$ ms, while the time between frames was the same, $\Delta t = 5.0$ ms. From the figure one can see that the second point decreases with δt_e , suggesting that for $\delta t_e \rightarrow 0$ it will also disappear. This limit would correspond to an instantaneous snapshots in time.

This effect is not intuitive, and therefore we ran a simulation to test our hypothesis of the motion blur. In the simulation, one particle performs a random walk in 1D. This is a well behaved and simple Brownian system [29]. We generated trajectories with one million steps

to get sufficient statistics. Then we performed motion blurring by taking an average of 10 steps and creating a new trajectory with 100'000 steps. The resulting velocity auto-correlation function is shown in the Figure B.4b as red triangles. The simulation reproduces the same pattern as seen in the experiments. Further, we reduced the exposure time by averaging over 5 steps and discarding the other 5, which is shown in the blue diamonds. This partial blurring reduces the observed auto-correlation, as with the experiment. Finally, we took only every 10th step without averaging and saw no auto-correlation, as expected. This simple model proves that motion blur induces apparent velocity auto-correlation for the second time step. The code used in the simulation is available at [143].

B.4.1 VACF for moving particles

Figure B.5 shows velocity auto-correlation function computed using Equation (2.3). Clearly, the the coefficient is dominated by the average velocity that is shown as the red line. The first two data points are visibly higher. This increase corresponds to the VACF measured for passively diffusing particles, as shown in the Figure B.4a. Therefore, the first data point is self correlation due to Brownian motion, and the second one is artefact due to the motion blur.

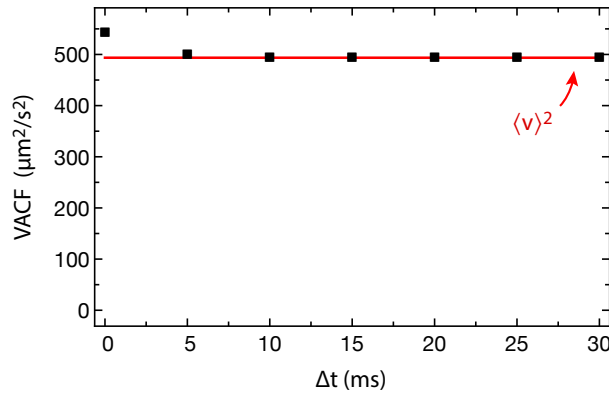


Figure B.5: Velocity auto-correlation function for particles migrating in an electric field. The particles were driven with 100 mV potential through a channel of length $L = 13 \mu\text{m}$. The red line indicates the average velocity squared. The first and second data points are above the red line by $49.5 \mu\text{m}^2/\text{s}^2$ and $4.9 \mu\text{m}^2/\text{s}^2$, respectively. The other points have a small positive bias that is nearly indiscernible in this plot.

The other data points at $\Delta t \geq 10 \text{ms}$ are also a bit higher than the line at $\langle v \rangle^2$. To see this difference we subtract the average velocity from each measurement:

$$\langle [v(0) - \langle v \rangle][v(\Delta t) - \langle v \rangle] \rangle \approx \langle v(0)v(\Delta t) \rangle - \langle v \rangle^2, \quad (\text{B.3})$$

where the approximation is exact if the velocities are constant throughout the channel. Figure B.6a shows the resulting auto-correlation. Again, the first two data points are higher than the tail average that is indicated by the blue dashed line. We investigate the offset in the tail. It is almost constant for all time separations, which can be explained with individual particles moving at slightly different average velocities. In such case, the offset (β^2) should scale linearly with the average velocity squared ($\langle v \rangle^2$), because it propagates through Equation (B.3). Figure B.6b shows the relation between the two quantities, where each data point represents an experiment in B4-10um-5 chip. The slope of the linear fit is 0.047, which is very close to W in the position variance measurement, and also close to the velocity variation measurement as reported in the Figure 5.6b. Therefore, the variation of particle average velocities explains the constant offset and agrees with other measurements. See Sections 5.1.3 and B.3 for the other measurements.

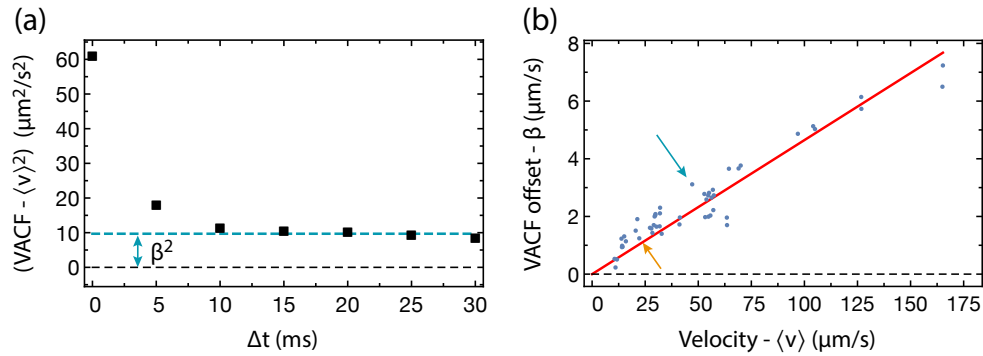


Figure B.6: Difference between VACF and average velocity for driven transport. (a) Velocity auto-correlation function with the average velocity squared subtracted. The particle was drive with 200 mV. The blue dashed line indicates an average for $\Delta t \geq 10$ ms, where we call is VACF offset, β^2 . (b) Square root of VACF offset parameter versus the average particle velocity. Each data point represents a different experiment in “B4-10um-5” chip. The red lines shows a linear fit with a slope 0.047. The blue arrow indicates the experiment shown in (a), while the orange arrow indicates the experiment shown in the Figure B.5.

Appendix C

Full analytical model for particle interaction

The following derivation was done by Eric Lauga and John R. Lister, while the comparison with simulation models was done by Karolis Misiunas.

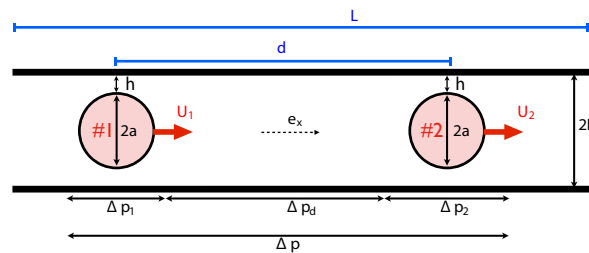


Figure C.1: Notation for the two-sphere resistance calculation.

We consider the setup shown in Figure C.1. We have two spheres of identical radius, a , along the centerline of a pipe of radius R , separated by a distance d (which we assume is a few sphere diameters, so that the only hydrodynamic coupling is through the net flow induced in the pipe). We denote by x the coordinate along the pipe and $L = \ell + d$ the total pipe length. Sphere i is assumed to move in the $+x$ direction with velocity U_i and we use Δp_i to denote the pressure increase in the x direction across the sphere. The total pressure increase across the two-sphere system is denoted Δp .

Flow rate vs. pressure difference across each sphere

The main goal of this problem is to compute the flow rate setup in the pipe as a result of the motion of the spheres. In order to determine the flow rate we have to consider overall mass

conservation. The flow rate Q can be computed in the pipe in between the two spheres, which has a length d and for which we denote the pressure increase Δp_d . Assuming Poiseuille flow we have

$$\frac{\Delta p_d}{\eta} = -\frac{8dQ}{\pi R^4}, \quad (\text{C.1})$$

(the minus sign is there because Δp_d is an increase in pressure, not a pressure drop). The total pressure increase across the two-sphere system is thus given by

$$\Delta p = \Delta p_d + \Delta p_1 + \Delta p_2, \quad (\text{C.2})$$

and must satisfy the Poiseuille relationship on the other side of the pipe (through the outer chamber)

$$\frac{\Delta p}{\eta} = \frac{8\ell Q}{\pi R^4}. \quad (\text{C.3})$$

We therefore have

$$-\frac{8dQ}{\pi R^4} + \frac{\Delta p_1}{\eta} + \frac{\Delta p_2}{\eta} = \frac{8\ell Q}{\pi R^4}, \quad (\text{C.4})$$

and thus

$$\frac{\Delta p_1}{\eta} + \frac{\Delta p_2}{\eta} = \frac{8LQ}{\pi R^4}, \quad (\text{C.5})$$

Flow around sphere 1

We now consider the flow around sphere 1, and the other one can be deduced by symmetry. Since the sphere is moving in the lab frame, it is easier to jump into the frame moving at speed U_1 , where the geometry of the problem is steady. Mass conservation in the moving frame around the sphere is written as

$$Q - \pi R^2 U_1 = 2\pi R q_1, \quad (\text{C.6})$$

where q_1 is the one-dimensional x -lubrication flow rate in the thin gap between the sphere and the pipe, which is constant in this frame. That flow is a simple (lubrication) combination of shear and Poiseuille flow. Writing the pressure gradient in the thin gap p_1/x we have

$$q_1 = -\frac{1}{2}U_1 h(x) - \frac{1}{12\eta} \frac{p_1}{x} h^3(x), \quad (\text{C.7})$$

which means that the pressure gradient satisfies

$$\frac{1}{\eta} \frac{p_1}{x} = -\frac{6U_1}{h^2(x)} - \frac{12q_1}{h^3(x)}. \quad (\text{C.8})$$

In this equation, $h(x) \approx h_0 + x^2/2a$, where h_0 is the smallest clearance between the sphere and the pipe. Integrating Eq. (C.8) across the particle gives access to the pressure drop as

$$\frac{\Delta p_1}{\eta} = -6U_1 I_2 - 12q_1 I_3, \quad (\text{C.9})$$

where we have denoted

$$I_n = \int_{-\infty}^{+\infty} \frac{x}{h^n(x)} = \frac{\sqrt{2ah_0}}{h_0^n} \int_{-\infty}^{+\infty} \frac{x}{(1+u^2)^n}, \quad (\text{C.10})$$

and therefore

$$I_1 = \pi \frac{\sqrt{2ah_0}}{h_0}; \quad I_2 = \frac{\pi}{2} \frac{\sqrt{2ah_0}}{h_0^2}; \quad I_3 = \frac{3\pi}{8} \frac{\sqrt{2ah_0}}{h_0^3}. \quad (\text{C.11})$$

Flow rate vs. velocity relationship

Putting together Eq. (C.12) and Eq. (C.9), and using the similar version to Eq. (C.12) for sphere #2, we get

$$\frac{\Delta p_1}{\eta} + \frac{\Delta p_2}{\eta} = \frac{8LQ}{\pi R^4}, \quad (\text{C.12})$$

$$-6(U_1 + U_2)I_2 - 12(q_1 + q_2)I_3 = \frac{8LQ}{\pi R^4}. \quad (\text{C.13})$$

Using Eq. (C.6) to replace explicitly the q_i 's with

$$q_i = \frac{Q}{2\pi R} - \frac{RU_i}{2}, \quad (\text{C.14})$$

we obtain the final (symmetric) relationship between the flow rate in the pipe, Q , and the velocity of each sphere as

$$(RI_3 - I_2)(U_1 + U_2) = \left(\frac{4L}{3\pi R^4} + \frac{2I_3}{\pi R} \right) Q. \quad (\text{C.15})$$

Force on sphere 1

We now compute the force on sphere 1 in order to obtain the coupled resistance matrix (and invert it to obtain the mobility matrix needed for diffusion). The force on sphere 1 arises from two sources: the pressure increase across the sphere and the thin lubrication flow between the sphere and the pipe. The simplest way to compute F_1 is to do a force balance on a control volume of fluid which includes the particle. The total force on the fluid must sum up to zero.

Since the force from the particle on the fluid is $-F_1$ we have by force balance on the fluid in the x direction

$$-F_1 - \pi R^2 \Delta p_1 + 2\pi R \int \tau_1(x) dx = 0, \quad (\text{C.16})$$

where $\tau_1(x)$ is the distribution of wall shear stresses in the thin gap, which is easily computed in the lubrication limit

$$\tau_1(x) = -\frac{\eta U_1}{h(x)} + \frac{1}{2} \frac{p_1}{x} h(x). \quad (\text{C.17})$$

Using Eq. (C.8) we thus have

$$\tau_1(x) = -\frac{4\eta U_1}{h(x)} - \frac{6\eta q_1}{h^2(x)}, \quad (\text{C.18})$$

and therefore the net force is given by

$$F_1 = -\pi R^2 \Delta p_1 - 2\pi \eta R (4U_1 I_1 + 6q_1 I_2). \quad (\text{C.19})$$

We now plug in the value for Δp_1 , Eq. (C.9), and get

$$F_1 = 2\pi \eta R (3RI_2 - 4I_1) U_1 + 12\pi \eta R (RI_3 - I_2) q_1 \quad (\text{C.20})$$

We then use

$$q_1 = \frac{Q}{2\pi R} - \frac{RU_1}{2}, \quad (\text{C.21})$$

to obtain

$$F_1 = 6\eta (RI_3 - I_2) Q + 2\pi \eta R (6RI_2 - 4I_1 - 3R^2 I_3) U_1. \quad (\text{C.22})$$

The flow rate, Q , is given in Eq. (C.15) by

$$Q = \frac{3\pi R^4 (RI_3 - I_2)}{4L + 6R^3 I_3} (U_1 + U_2), \quad (\text{C.23})$$

which, when plugged into Eq. (C.22), leads to the final equation for the force

$$F_1 = \zeta_{1,1} U_1 + \zeta_{12} U_2, \quad (\text{C.24})$$

with

$$\zeta_{12} = \frac{18\eta \pi R^4 (RI_3 - I_2)^2}{4L + 6R^3 I_3}, \quad (\text{C.25})$$

and

$$\zeta_{11} = \zeta_{12} + 2\pi \eta R (6RI_2 - 4I_1 - 3R^2 I_3). \quad (\text{C.26})$$

The formula for F_2 is identical with a $1 \leftrightarrow 2$ permutation in the velocities.

Comparison with simulations

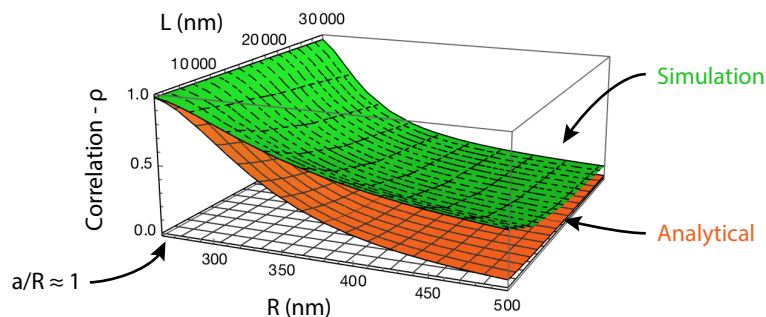


Figure C.2: Analytical model comparison with simulation for the predicted correlation coefficients. The correlation coefficient was computed using $\rho \approx -\zeta_{1,2}/\sqrt{\zeta_{1,1}\zeta_{2,2}}$. The particles were $2a = 500$ nm wide. The analytical model agrees very well for $a/R \approx 1$, but deviates away for smaller a/R ratios.

Figure C.2 shows a comparison of these equations to the numerical simulations for the same problem. The analytical model agrees very well for tightly confined particles ($a/R \approx 1$), but deviates away for more realistic scenarios of $a/R \approx 0.5$. This deviation is due to lubrication approximations that were necessary for deriving the model.

List of publications

1. Laohakunakorn, N., Ghosal, S., Otto, O., Misiunas, K. & Keyser, U. F. DNA Interactions in Crowded Nanopores. *Nano Lett.* 13, (2013).
2. Hernandez-Ainsa, S. et al. DNA origami nanopores for controlling DNA translocation. *ACS Nano* 7, 60246030 (2013).
3. Dettmer, S. L., Pagliara, S., Misiunas, K. & Keyser, U. F. Anisotropic diffusion of spherical particles in closely confining microchannels. *Phys. Rev. E* 89, 062305 (2014).
4. Hernández-Ainsa, S., Misiunas, K., Thacker, V. V, Hemmig, E. a & Keyser, U. F. Voltage-Dependent Properties of DNA Origami Nanopores. *Nano Lett.* (2014).
5. Pagliara, S. et al. Diffusion coefficients and particle transport in synthetic membrane channels. *Eur. Phys. J. Spec. Top.* 223, 31453163 (2014).
6. Misiunas, K., Pagliara, S., Lauga, E., Lister, J. R. & Keyser, U. F. Nondecaying Hydrodynamic Interactions along Narrow Channels. *Phys. Rev. Lett.* 115, 038301 (2015).

List of figures

1.1	Examples of channels in nature and technology	2
1.2	Examples of particle transport through nano-channels	3
1.3	Motivation for microfluidic channels	5
2.1	Geometry of channel with a particle	7
2.2	Double layer illustration	14
2.3	Electroosmosis illustration	16
2.4	Electrophoresis illustration	17
3.1	Setup diagram	22
3.2	PDMS replica moulding technique	23
3.3	SEM images of channel molds	24
3.4	Designs of microfluidic access layer	25
3.5	Photograph of microfluidic chip	26
3.6	Illustration of particle tracking	27
3.7	Bright-field images of particle blobs	29
3.8	Sub-pixel position fitting algorithm response to noise	31
3.9	Sub-pixel position fitting test with piezo stage	32
3.10	Sample trajectory for Brownian motion inside a channel	33
3.11	MSD for single particle	34
3.12	Localised diffusion coefficients	36
3.13	Measuring channel width from trajectories	37
3.14	COMSOL simulation mesh	38
3.15	Geometry for single particle simulations	39
3.16	$D_x \propto a/R$ for infinite channels	40
3.17	Friction coefficient as a function of particles position	42
3.18	Hydrodynamic friction as a function of a/R and b/R	43
3.19	Diffusion coefficient for different positions	44

3.20	Effects of particle rotation	45
3.21	Simulation of position dependence for finite channel	46
3.22	Simulation of D_x in short channels	48
3.23	Flow field for infinite and finite channels	48
3.24	Effects of access resistance to D_x	49
3.25	Periodic B.C. with access resistance	50
3.26	D_x v a/R comparison with measurements	51
4.1	Multiple particle correlated trajectories	54
4.2	Closed vs open channel	55
4.3	Correlation as function of channel length	57
4.4	Friction coefficients for multiple particles	59
4.5	Many particle correlations	61
4.6	D_x vs number of particles	62
4.7	A generalised simulation method for many particles	63
4.8	Simulation of hydrodynamic interactions for different a/R and L	64
4.9	Correlation vs L	64
4.10	Brownian dynamics simulation for particle interactions	68
4.11	Interactions between particle of different sizes	69
4.12	Correlation at the channel's entrance	69
4.13	Correlation in two channels	70
5.1	Pressure application with micrometer drive	75
5.2	Pressure drop across microfluidic chip	76
5.3	Electric fields in microfluidic chip	77
5.4	Velocity stability in time	79
5.5	Electrophoresis in a channel	79
5.6	Electrophoretic velocity distributions	80
5.7	Electrophoretic velocity vs electric potential	81
5.8	Electrophoretic velocity vs c_0 and pH	82
5.9	Particle speed-up in channels	84
5.10	Tilt-able microscope	85
5.11	Driven particle interaction example	87
5.12	Driven particle interactions	88
5.13	Enhancement coefficient vs salt concentration and pH	89
5.14	Simulation geometry for many driven particles	91
5.15	Simulation of particles driven by pressure gradient	92

5.16	Simulation of particle interactions under the gravity fall	93
5.17	Flow profiles for electrophoresis in channels	94
5.18	Simulation of particle interactions when driven by electrophoresis	95
5.19	Simulation of electrophoretic enhancement coefficient vs c_0 and σ_p	96
5.20	Simulation of electrophoretic enhancement coefficient with electroosmosis . . .	98
5.21	Competition between electrophoresis and pressure	101
A.1	Entrance jamming	106
A.2	Entrance jamming examples	107
B.1	Surface coatings	110
B.2	MSD for moving particles	112
B.3	MSD for polymer transport	113
B.4	Velocity auto-correlation function for single particle	114
B.5	VACF for particles migrating in an electric field	115
B.6	VACF offset	116
C.1	Notation for the two-sphere resistance calculation.	117
C.2	Correlation coef. comparison between analytic solution and simulations	121

List of tables

3.1	SEM or AFM dimensions of different channels	25
3.2	Sub-pixel localisation algorithm comparison	30
3.3	Tracking errors	31
3.4	Diffusion coefficients	34
3.5	Effective radius for different channels	37

List of revisions

2016-09-02 University library copy

2016-09-15 Removed the declaration page and added a list of revisions

References

- [1] B. Alberts, A. Johnson, J. Lewis, D. Morgan, M. Raff, K. Roberts, and P. Walter, *Molecular Biology of the Cell*, 6th ed. (Garland Science, 2014).
- [2] Kelvinsong, *Diagram of a capillary*, URL: en.wikipedia.org/wiki/File:Capillary.svg, 2013.
- [3] D. T. Nicholson, *SEM micrograph of transgranular cracking induced by experimental freeze-thaw in a highly porous magnesian limestone*, URL: www.dawntnicholson.org.uk/detpagemain.html, 2010.
- [4] J. H. Pikul, H. Gang Zhang, J. Cho, P. V. Braun, and W. P. King, “High-power lithium ion microbatteries from interdigitated three-dimensional bicontinuous nanoporous electrodes”, *Nature Communications* **4**, 1732 (2013).
- [5] O. Nanopores, *Technology illustration*, URL: www.nanoporetech.com.
- [6] Z. Membranes, *SEM image of a membrane*, URL: www.zena-membranes.cz.
- [7] W. Yang, J. Gelles, and S. M. Musser, “Imaging of single-molecule translocation through nuclear pore complexes”, *Proceedings of the National Academy of Sciences* **101**, 12887 (2004).
- [8] V. V. Thacker, S. Ghosal, S. Hernández-Ainsa, N. A. W. Bell, and U. F. Keyser, “Studying DNA translocation in nanocapillaries using single molecule fluorescence”, *Applied Physics Letters* **101**, 223704 (2012).
- [9] “Blausen gallery 2014”, *Wikiversity Journal of Medicine* (2014) [10.15347/wjm/2014.010](https://doi.org/10.15347/wjm/2014.010).
- [10] N. Laohakunakorn, S. Ghosal, O. Otto, K. Misiunas, and U. F. Keyser, “DNA Interactions in Crowded Nanopores”, *Nano Letters* **13**, 2798 (2013).
- [11] S. Gravelle, L. Joly, F. Detcheverry, C. Ybert, C. Cottin-Bizonne, and L. Bocquet, “Optimizing water permeability through the hourglass shape of aquaporins”, *Proceedings of the National Academy of Sciences* **110**, 16367 (2013).
- [12] M. Suntharalingam, and S. R. Wentz, “Peering through the pore”, *Developmental Cell* **4**, 775 (2003).
- [13] C. A. Hubner, “Ion channel diseases”, *Human Molecular Genetics* **11**, 2435 (2002).
- [14] B. Cui, B. Lin, S. Sharma, and S. a. Rice, “Equilibrium structure and effective pair interaction in a quasi-one-dimensional colloid liquid”, *The Journal of Chemical Physics* **116**, 3119 (2002).
- [15] S. Pagliara, C. Schwall, and U. F. Keyser, “Optimizing diffusive transport through a synthetic membrane channel”, *Advanced Materials* **25**, 844 (2013).

- [16] S. Pagliara, S. L. Dettmer, and U. F. Keyser, “Channel-facilitated diffusion boosted by particle binding at the channel entrance”, *Physical Review Letters* **113**, 048102 (2014).
- [17] Q. Wei, “Single-file diffusion of colloids in one-dimensional channels”, *Science* **287**, 625 (2000).
- [18] C. Lutz, M. Kollmann, and C. Bechinger, “Single-file diffusion of colloids in one-dimensional channels”, *Physical Review Letters* **93**, 026001 (2004).
- [19] J. B. Delfau, C. Coste, C. Even, and M. Saint Jean, “Single-file diffusion of interacting particles in a finite-sized channel”, *Physical Review E* **82**, 031201 (2010).
- [20] M. Iwaoka, and T. Ishii, “Experimental wall correction factors of single solid spheres in circular cylinders”, *Journal of Chemical Engineering of Japan* **12**, 239 (1979).
- [21] C. Hilty, and M. Winterhalter, “Facilitated substrate transport through membrane proteins”, *Physical Review Letters* **86**, 5624 (2001).
- [22] B. Cui, H. Diamant, and B. Lin, “Screened hydrodynamic interaction in a narrow channel”, *Physical Review Letters* **89**, 188302 (2002).
- [23] B. Lin, B. Cui, J.-H. Lee, and J. Yu, “Hydrodynamic coupling in diffusion of quasio-dimensional Brownian particles”, *Europhysics Letters (EPL)* **57**, 724 (2002).
- [24] D. T. Valley, S. a. Rice, B. Cui, H. M. Ho, H. Diamant, and B. Lin, “Pair diffusion in quasi-one- and quasi-two-dimensional binary colloid suspensions”, *The Journal of Chemical Physics* **126**, 134908 (2007).
- [25] E. Kosheleva, B. Leahy, H. Diamant, B. Lin, and S. a. Rice, “Long-range hydrodynamic correlations in quasi-one-dimensional circular and straight geometries”, *Physical Review E* **86**, 041402 (2012).
- [26] J.-L. Viovy, “Electrophoresis of DNA and other polyelectrolytes: Physical mechanisms”, *Reviews of Modern Physics* **72**, 813 (2000).
- [27] D. Mehlhorn, D. Kondrashova, C. Küster, D. Enke, T. Emmerich, A. Bunde, R. Valiullin, and J. Kärger, “Diffusion in complementary pore spaces”, *Adsorption* (2016) 10.1007/s10450-016-9792-y.
- [28] J. Cama, H. Bajaj, S. Pagliara, T. Maier, Y. Braun, M. Winterhalter, and U. F. Keyser, “Quantification of fluoroquinolone uptake through the outer membrane channel OmpF of *Escherichia coli*”, *Journal of the American Chemical Society* **137**, 13836 (2015).
- [29] R. M. Mazo, *Brownian Motion: Fluctuations, Dynamics, and Applications* (Oxford University Press, 2002).
- [30] R. Huang, B. Lukic, S. Jeney, and E.-L. Florin, “Direct observation of ballistic Brownian motion on a single particle”, *Nature Physics* **7**, 576 (2010).
- [31] T. Franosch, M. Grimm, M. Belushkin, F. M. Mor, G. Foffi, L. Forró, and S. Jeney, “Resonances arising from hydrodynamic memory in Brownian motion.”, *Nature* **478**, 85 (2011).
- [32] B. J. Alder, and T. E. Wainwright, “Decay of the velocity autocorrelation function”, *Physical Review A* **1**, 18 (1970).
- [33] L. Bocquet, and J.-l. Barrat, “Hydrodynamic properties of confined fluids”, *J. Phys. Condens. Matter* **8**, 9297 (1996).

- [34] M. H. J. Hagen, I. Pagonabarraga, C. P. Lowe, and D. Frenkel, “Algebraic decay of velocity fluctuations in a confined fluid”, [Physical Review Letters](#) **78**, 3785 (1997).
- [35] W. Sutherland, “Dynamical theory of diffusion for non-electrolytes and the molecular mass of albumin”, *Philosophical Magazine* **9**, 781 (1905).
- [36] A. Einstein, “Über die von der molekularkinetischen Theorie der Wärme geforderte Bewegung von in ruhenden Flüssigkeiten suspendierten Teilchen”, [Annalen der Physik](#) **322**, 549 (1905).
- [37] M. von Smoluchowski, “Zur kinetischen Theorie der Brownschen Molekularbewegung und der Suspensionen”, [Annalen der Physik](#) **326**, 756 (1906).
- [38] G. K. Batchelor, *An Introduction to Fluid Dynamics* (Cambridge University Press, 2000).
- [39] J. Happel, and H. Brenner, *Low Reynolds number hydrodynamics*, Vol. 1, Mechanics of fluids and transport processes (Springer, 1981).
- [40] W. Deen, “Hindered transport of large molecules in liquidfilled pores”, [AIChE Journal](#) **33**, 1409 (1987).
- [41] H. Diamant, “Hydrodynamic interaction in confined geometries”, [Journal of the Physical Society of Japan](#) **78**, 1 (2009).
- [42] J. C. Crocker, “Measurement of the hydrodynamic corrections to the Brownian motion of two colloidal spheres”, [The Journal of Chemical Physics](#) **106**, 2837 (1997).
- [43] B. Cui, H. Diamant, B. Lin, and S. Rice, “Anomalous hydrodynamic interaction in a quasi-two-dimensional suspension”, [Physical Review Letters](#) **92**, 258301 (2004).
- [44] N. Liron, and R. Shahar, “Stokes flow due to a Stokeslet in a pipe”, [Journal of Fluid Mechanics](#) **86**, 727 (1978).
- [45] H.-j. Butt, K. Graf, and M. Kappl, *Physics and Chemistry of Interfaces* (Wiley, 2003).
- [46] O. Stern, “Zur theorie der elektrolytischen doppelschicht”, [Zeitschrift fur Elektrochemie](#) **30**, 508 (1924).
- [47] Tosaka, *Double layer diagram*, URL: [en.wikipedia.org/wiki/File:Electric_double-layer_\(BMD_model\)_NT.PNG](http://en.wikipedia.org/wiki/File:Electric_double-layer_(BMD_model)_NT.PNG).
- [48] O. Teschke, G. Ceotto, and E. de Souza, “Interfacial water dielectric-permittivity-profile measurements using atomic force microscopy”, [Physical Review E](#) **64**, 011605 (2001).
- [49] U. F. Keyser, S. van Dorp, and S. G. Lemay, “Tether forces in DNA electrophoresis”, [Chemical Society Reviews](#) **39**, 939 (2010).
- [50] U. F. Keyser, B. N. Koeleman, S. van Dorp, D. Krapf, R. M. M. Smeets, S. G. Lemay, N. H. Dekker, and C. Dekker, “Direct force measurements on DNA in a solid-state nanopore”, [Nature Physics](#) **2**, 473 (2006).
- [51] J. H. Masliyah, and S. Bhattacharjee, *Electrokinetic and Colloid Transport Phenomena* (Wiley, 2006).
- [52] G. Karniadakis, A. Beskok, and N. Aluru, *Microflows and Nanoflows: Fundamentals and Simulation* (Springer, 2005).
- [53] H. J. Keh, and J. L. Anderson, “Boundary effects on electrophoretic motion of colloidal spheres”, [Journal of Fluid Mechanics](#) **153**, 417 (1985).

- [54] J. Chakraborty, and S. Chakraborty, *Mechanics Over Micro and Nano Scales*, edited by S. Chakraborty, (Springer New York, New York, NY, 2011), pp. 1–60.
- [55] N. V. Priezjev, and S. M. Troian, “Influence of periodic wall roughness on the slip behaviour at liquid/solid interfaces: molecular-scale simulations versus continuum predictions”, *Journal of Fluid Mechanics* **554**, 25 (2006).
- [56] C. Kumar, *Microfluidic Devices in Nanotechnology: Fundamental Concepts* (Wiley, 2010).
- [57] L. Saint-Raymond, *Hydrodynamic limits of the boltzmann equation* (Springer, 2009).
- [58] S. Pagliara, C. Chimere, R. Langford, D. G. a. L. Aarts, and U. F. Keyser, “Parallel sub-micrometre channels with different dimensions for laser scattering detection”, *Lab on a Chip* **11**, 3365 (2011).
- [59] S. Bhattacharya, A. Datta, J. M. Berg, and S. Gangopadhyay, “Studies on surface wettability of poly(dimethyl) siloxane (PDMS) and glass under oxygen-plasma treatment and correlation with bond strength”, *Journal of Microelectromechanical Systems* **14**, 590 (2005).
- [60] S. L. Dettmer, U. F. Keyser, and S. Pagliara, “Local characterization of hindered Brownian motion by using digital video microscopy and 3D particle tracking”, *Review of Scientific Instruments* **85**, 023708 (2014).
- [61] R. C. Gonzalez, and R. E. Woods, *Digital Image Processing* (Prentice Hall, 2010).
- [62] M. K. Cheezum, W. F. Walker, and W. H. Guilford, “Quantitative comparison of algorithms for tracking single fluorescent particles”, *Biophysical journal* **81**, 2378 (2001).
- [63] N. Chenouard, I. Smal, F. de Chaumont, M. Maka, I. F. Sbalzarini, Y. Gong, J. Cardinale, C. Carthel, S. Coraluppi, M. Winter, A. R. Cohen, W. J. Godinez, K. Rohr, Y. Kalaidzidis, L. Liang, J. Duncan, H. Shen, Y. Xu, K. E. G. Magnusson, J. Jaldén, H. M. Blau, P. Paul-Gilloteaux, P. Roudot, C. Kervrann, F. Waharte, J.-Y. Tinevez, S. L. Shorte, J. Willemse, K. Celler, G. P. van Wezel, H.-W. Dan, Y.-S. Tsai, C. O. de Solórzano, J.-C. Olivo-Marin, and E. Meijering, “Objective comparison of particle tracking methods”, *Nature Methods* **11**, 281 (2014).
- [64] R. Parthasarathy, “Rapid, accurate particle tracking by calculation of radial symmetry centers”, *Nature Methods* **9**, 724 (2012).
- [65] K. Misiunas, *Source code for subpixel fitting algorithm*, URL: gist.github.com/kmisiunas/53e3b53e704a35343266, 2016.
- [66] T. Savin, and P. S. Doyle, “Static and Dynamic Errors in Particle Tracking Microrheology”, *Biophysical Journal* **88**, 623 (2005).
- [67] M. Gyger, F. Ruckerl, J. Käs, and J. Ruiz-García, “Errors in two particle tracking at close distances”, *Journal of Colloid and Interface Science* **326**, 382 (2008).
- [68] M. Polin, D. G. Grier, and Y. Han, “Colloidal electrostatic interactions near a conducting surface”, *Physical Review E* **76**, 041406 (2007).
- [69] M. Husain, T. Boudier, P. Paul-Gilloteaux, I. Casuso, and S. Scheuring, “Software for drift compensation, particle tracking and particle analysis of high-speed atomic force microscopy image series”, *Journal of Molecular Recognition* **25**, 292 (2012).

- [70] H. W. Kuhn, "The Hungarian method for the assignment problem", *Naval Research Logistics Quarterly* **2**, 83 (1955).
- [71] X. Michalet, "Mean square displacement analysis of single-particle trajectories with localization error: Brownian motion in an isotropic medium", *Physical Review E* **82**, 041914 (2010).
- [72] W. M. Haynes, *CRC Handbook of Chemistry and Physics, 95th Edition* (CRC Press, 2014).
- [73] S. L. Dettmer, S. Pagliara, K. Misiunas, and U. F. Keyser, "Anisotropic diffusion of spherical particles in closely confining microchannels", *Physical Review E* **89**, 062305 (2014).
- [74] S. Pagliara, S. L. Dettmer, K. Misiunas, L. Lea, Y. Tan, and U. F. Keyser, "Diffusion coefficients and particle transport in synthetic membrane channels", *The European Physical Journal Special Topics* **223**, 3145 (2014).
- [75] M. Bahrami, M. M. Yovanovich, and J. R. Culham, "Pressure Drop of Fully-Developed, Laminar Flow in Microchannels of Arbitrary Cross-Section", *Journal of Fluids Engineering* **128**, 1036 (2006).
- [76] M. W. Al-mufti, U. Hashim, and T. Adam, "Current trend in simulation: Review Nanostructures using Comsol Multiphysics", *Journal of Applied Sciences Research* **8**, 5579 (2012).
- [77] S. van Dorp, U. F. Keyser, N. H. Dekker, C. Dekker, and S. G. Lemay, "Origin of the electrophoretic force on DNA in solid-state nanopores", *Nature Physics* **5**, 347 (2009).
- [78] J. Fish, and T. Belytschko, *A First Course in Finite Elements* (Wiley, 2007).
- [79] I. Pagonabarraga, M. H. J. Hagen, C. P. Lowe, and D. Frenkel, "Short-time dynamics of colloidal suspensions in confined geometries", *Physical Review E* **59**, 4458 (1999).
- [80] P. Sharma, S. Ghosh, and S. Bhattacharya, "A high-precision study of hindered diffusion near a wall", *Applied Physics Letters* **97**, 104101 (2010).
- [81] N. Al Quddus, W. a. Moussa, and S. Bhattacharjee, "Motion of a spherical particle in a cylindrical channel using arbitrary Lagrangian-Eulerian method", *Journal of Colloid and Interface Science* **317**, 620 (2008).
- [82] M. Schiel, and Z. S. Siwy, "Diffusion and trapping of single particles in pores with combined pressure and dynamic voltage", *The Journal of Physical Chemistry C* **118**, 19214 (2014).
- [83] A. M. Berezhkovskii, and S. M. Bezrukov, "Optimizing transport of metabolites through large channels: molecular sieves with and without binding", *Biophysical Journal* **88**, L17 (2005).
- [84] E. R. Dufresne, T. M. Squires, M. P. Brenner, and D. G. Grier, "Hydrodynamic coupling of two Brownian spheres to a planar surface", *Physical Review Letters* **85**, 3317 (2000).
- [85] Y. Sokolov, D. Frydel, D. G. Grier, H. Diamant, and Y. Roichman, "Hydrodynamic pair attractions between driven colloidal particles", *Physical Review Letters* **107**, 158302 (2011).
- [86] K. Misiunas, S. Pagliara, E. Lauga, J. R. Lister, and U. F. Keyser, "Nondecaying hydrodynamic interactions along narrow channels", *Physical Review Letters* **115**, 038301 (2015).

- [87] D. Reguera, G. Schmid, P. Burada, J. Rubí, P. Reimann, and P. Hänggi, “Entropic transport: kinetics, scaling, and control mechanisms”, *Physical Review Letters* **96**, 130603 (2006).
- [88] D. G. Grier, “A revolution in optical manipulation.”, *Nature* **424**, 810 (2003).
- [89] M. Padgett, and R. Di Leonardo, “Holographic optical tweezers and their relevance to lab on chip devices”, *Lab on a Chip* **11**, 1196 (2011).
- [90] K. Misiunas, *Video demonstration for Nondecaying hydrodynamic interactions experiment*, URL: www.youtube.com/watch?v=rbbxQ8xZQaA.
- [91] K. F. Riley, P. Hobson, and S. J. Bence, *Mathematical Methods for Physics and Engineering: A Comprehensive Guide* (Cambridge University Press, 2006).
- [92] W. R. Smythe, “Flow around a sphere in a circular tube”, *Physics of Fluids* **4**, 756 (1961).
- [93] X. Xu, S. Rice, B. Lin, and H. Diamant, “Influence of hydrodynamic coupling on pair diffusion in a quasi-one-dimensional colloid system”, *Physical Review Letters* **95**, 158301 (2005).
- [94] J. Sane, J. T. Padding, and A. A. Louis, “The crossover from single file to Fickian diffusion”, *The Royal Society of Chemistry* **144**, 7 (2010).
- [95] R. Seghir, and S. Arscott, “Extended PDMS stiffness range for flexible systems”, *Sensors and Actuators A: Physical* **230**, 33 (2015).
- [96] D. L. Ermak, and J. a. McCammon, “Brownian dynamics with hydrodynamic interactions”, *The Journal of Chemical Physics* **69**, 1352 (1978).
- [97] K. Misiunas, *Source code for Brownian dynamics simulation of 2 particles in 1D*, URL: gist.github.com/kmisiunas/9cb04f18e0ab22644e69265566982913, 2014.
- [98] P. M. Bungay, and H. Brenner, “The motion of a closely-fitting sphere in a fluid-filled tube”, *International Journal of Multiphase Flow* **1**, 25 (1973).
- [99] J. Happel, and B. J. Bryne, “Motion of a sphere in a cylindrical tube”, *Industrial & Engineering Chemistry* **46**, 1181 (1954).
- [100] S. Navardi, and S. Bhattacharya, “Axial pressure-difference between far-fields across a sphere in viscous flow bounded by a cylinder”, *Physics of Fluids* **22**, 103305 (2010).
- [101] M. Frank, D. Anderson, E. R. Weeks, and J. F. Morris, “Particle migration in pressure-driven flow of a Brownian suspension”, *Journal of Fluid Mechanics* **493** (2003) 10.1017/S0022112003006001.
- [102] M. K. Lyon, and L. G. Leal, “An experimental study of the motion of concentrated suspensions in two-dimensional channel flow. Part 1. Monodisperse systems”, *Journal of Fluid Mechanics* **363**, 25 (1998).
- [103] L. D. Reed, and F. A. Morrison, “Hydrodynamic interactions in electrophoresis”, *Journal of Colloid And Interface Science* **54**, 117 (1976).
- [104] H. J. Keh, and F. R. Yang, “Particle interactions in electrophoresis”, *Journal of Colloid and Interface Science* **139**, 105 (1990).
- [105] A. A. Shugai, S. L. Carnie, D. Y. Chan, and J. L. Anderson, “Electrophoretic motion of two spherical particles with thick double layers”, *Journal of Colloid and Interface Science* **191**, 357 (1997).

- [106] H. J. Keh, and S. B. Chen, "Particle interactions in electrophoresis", *Journal of Colloid and Interface Science* **130**, 542 (1989).
- [107] H. J. Keh, and S. B. Chen, "Particle interactions in electrophoresis", *Journal of Colloid and Interface Science* **130**, 542 (1989).
- [108] H. J. Keh, and J. Y. Chiou, "Electrophoresis of a colloidal sphere in a circular cylindrical pore", *AIChE Journal* **42**, 1397 (1996).
- [109] E. Yariv, and H. Brenner, "The electrophoretic mobility of an eccentrically positioned spherical particle in a cylindrical pore", *Physics of Fluids* **14**, 3354 (2002).
- [110] C. Ye, X. Xuan, and D. Li, "Eccentric electrophoretic motion of a sphere in circular cylindrical microchannels", *Microfluidics and Nanofluidics* **1**, 234 (2005).
- [111] J. P. Ebel, J. L. Anderson, and D. C. Prieve, "Diffusiophoresis of latex particles in electrolyte gradients", *Langmuir* **4**, 396 (1988).
- [112] J. Zhu, and X. Xuan, "Particle electrophoresis and dielectrophoresis in curved microchannels", *Journal of Colloid and Interface Science* **340**, 285 (2009).
- [113] Y. Kang, and D. Li, "Electrokinetic motion of particles and cells in microchannels", *Microfluidics and Nanofluidics* **6**, 431 (2009).
- [114] X. Xuan, B. Xu, and D. Li, "Accelerated particle electrophoretic motion and separation in converging-diverging microchannels", *Analytical Chemistry* **77**, 4323 (2005).
- [115] J.-p. Hsu, M.-h. Ku, and C.-y. Kao, "Electrophoresis of two identical cylindrical particles along the axis of a cylindrical pore", *Industrial & Engineering Chemistry Research* **44**, 1105 (2005).
- [116] J. P. Hsu, and L. H. Yeh, "Electrophoresis of two identical rigid spheres in a charged cylindrical pore", *Journal of Physical Chemistry B* **111**, 2579 (2007).
- [117] A. V. Singh, L. Sharma, and P. Gupta-Bhaya, "Studies on falling ball viscometry", *Physics.Flu-Dyn*, 1 (2012).
- [118] U. F. Keyser, J. van der Does, C. Dekker, and N. H. Dekker, "Optical tweezers for force measurements on DNA in nanopores", *Review of Scientific Instruments* **77**, 105105 (2006).
- [119] P. Lemeyonouin, A. Guillaume, K. K. Honoré, and T. Albert, "Influence of chlorides on the electrochemical oxidation of formic acid on thermally prepared platinum electrodes", *International Journal of Pure and Applied Sciences and Technology* **14**, 33 (2013).
- [120] D. Angell, and T. Dickinson, "The kinetics of the ferrous/ferric and ferro/ferricyanide reactions at platinum and gold electrodes", *Journal of Electroanalytical Chemistry and Interfacial Electrochemistry* **35**, 55 (1972).
- [121] P. H. Daum, and C. G. Enke, "Electrochemical kinetics of the ferri-ferrocyanide couple on platinum", *Analytical Chemistry* **41**, 653 (1969).
- [122] B. J. Kirby, and E. F. Hasselbrink, "Zeta potential of microfluidic substrates: 2. Data for polymers.", *Electrophoresis* **25**, 203 (2004).
- [123] S. Deshpande, Y. Caspi, A. Meijering, and C. Dekker, "Octanol-assisted liposome assembly on chip", *Nature communications* **accepted**, 1 (2015).

- [124] K. Ohsawa, M. Murata, and H. Ohshima, “Zeta potential and surface charge density of polystyrene-latex; comparison with synaptic vesicle and brush border membrane vesicle”, *Colloid & Polymer Science* **264**, 1005 (1986).
- [125] D. Mampallil, D. Van Den Ende, and F. Mugele, “A simple method to determine the surface charge in microfluidic channels”, *Electrophoresis* **31**, 563 (2010).
- [126] H. Strathmann, *Ion-Exchange Membrane Separation Processes* (Elsevier, 2004).
- [127] S. Sablani, M. Goosen, R. Al-Belushi, and M. Wilf, “Concentration polarization in ultrafiltration and reverse osmosis: A critical review”, *Desalination* **141**, 269 (2001).
- [128] N. Laohakunakorn, “Electrokinetic phenomena in nanopore transport”, PhD thesis (University of Cambridge, 2015).
- [129] N. Laohakunakorn, and U. F. Keyser, “Electroosmotic flow rectification in conical nanopores”, *Nanotechnology* **26**, 275202 (2015).
- [130] V. Tandon, and B. J. Kirby, “Zeta potential and electroosmotic mobility in microfluidic devices fabricated from hydrophobic polymers: 2. Slip and interfacial water structure”, *Electrophoresis* **29**, 1102 (2008).
- [131] V. Tandon, S. K. Bhagavatula, W. C. Nelson, and B. J. Kirby, “Zeta potential and electroosmotic mobility in microfluidic devices fabricated from hydrophobic polymers: 1. The origins of charge”, *Electrophoresis* **29**, 1092 (2008).
- [132] S. H. Behrens, and D. G. Grier, “The charge of glass and silica surfaces”, *The Journal of Chemical Physics* **115**, 6716 (2001).
- [133] B. J. Kirby, and E. F. Hasselbrink, “Zeta potential of microfluidic substrates: 1. Theory, experimental techniques, and effects on separations.”, *Electrophoresis* **25**, 187 (2004).
- [134] T. Shirai, M. Takai, and K. Ishihara, “Simple and functional modification of PDMS surface for microchannel electrophoresis”, in 14th international conference on miniaturized systems for chemistry and life sciences, October (2010), pp. 1946–1948.
- [135] M. E. Cates, J. Wittmer, J.-P. P. Bouchaud, and P. Claudin, “Jamming, force chains, and fragile matter”, *Physical Review Letters* **81**, 1841 (1998).
- [136] A. I. Campbell, and M. D. Haw, “Jamming and unjamming of concentrated colloidal dispersions in channel flow”, *Soft Matter* **6**, 4688 (2010).
- [137] W. Sung, and P. J. Park, “Polymer translocation through a pore in a membrane”, *Physical Review Letters* **77**, 783 (1996).
- [138] N. A. W. Bell, M. Muthukumar, and U. F. Keyser, “Translocation frequency of double-stranded DNA through a solid-state nanopore”, *Physical Review E* **93**, 022401 (2016).
- [139] N. A. W. Bell, and U. F. Keyser, “Specific protein detection using designed DNA carriers and nanopores”, *Journal of the American Chemical Society* **137**, 2035 (2015).
- [140] R. M. Robertson, S. Laib, and D. E. Smith, “Diffusion of isolated DNA molecules: Dependence on length and topology”, *Proceedings of the National Academy of Sciences* **103**, 7310 (2006).
- [141] N. A. W. Bell, and U. F. Keyser, “Digitally encoded DNA nanostructures for multiplexed, single-molecule protein sensing with nanopores”, *Nature Nanotechnology* (2016) **10**. 1038/nnano.2016.50.

-
- [142] T. Li, and M. G. Raizen, “Brownian motion at short time scales”, [Annalen der Physik](#) **525**, 281 (2013).
- [143] K. Misiunas, *Simulation code for particle motion blur*, URL: gist.github.com/kmisiunas/ca41f5cc8ae5f51a695bde4c07f14070, 2016.

